PERFORMANCE ANALYSIS AND CONTROL OF HVDC LINKS IN MULTI-MACHINE SYSTEMS WITH WIND FARMS

Thesis
Submitted in partial fulfillment of the requirements for the degree of

DOCTOR OF PHILOSOPHY

by

RASHMI

DEPARTMENT OF ELECTRICAL AND ELECTRONICS ENGINEERING
NATIONAL INSTITUTE OF TECHNOLOGY KARNATAKA
SURATHKAL, MANGALORE - 575025

February, 2024

DECLARATION

by the Ph.D. Research Scholar

I hereby ***declare*** that the Research Thesis entitled **PERFORMANCE ANALYSIS AND CONTROL OF HVDC LINKS IN MULTI-MACHINE SYSTEMS WITH WIND FARMS** which is being submitted to the ***National Institute of Technology Karnataka, Surathkal*** in partial fulfillment of the requirement for the award of the Degree of ***Doctor of Philosophy*** in **Department of Electrical and Electronics Engineering** is a ***bonafide report of the research work carried out by me***. The material contained in this Research Thesis has not been submitted to any University or Institution for the award of any degree.

Rashmi

Rashmi,
Reg. No. 187044EE006,
Department of Electrical and Electronics Engineering

Place: NITK, Surathkal
Date: 26-02-2024

CERTIFICATE

This is to certify that the Research Thesis entitled **PERFORMANCE ANALYSIS AND CONTROL OF HVDC LINKS IN MULTI-MACHINE SYSTEMS WITH WIND FARMS** submitted by Rashmi, (Register Number: 187044EE006) as the record of the research work carried out by her, is *accepted as the Research Thesis submission* in partial fulfillment of the requirements for the award of degree of **Doctor of Philosophy**.

Dr. Dattatraya N. Gaonkar
Research Guide

28/02/2024.
Dr. Dattatraya N. Gaonkar
Chairman-DRPC

PROFESSOR AND HEAD
DEPARTMENT OF ELECTRICAL AND ELECTRONICS ENGINEERING
NATIONAL INSTITUTE OF TECHNOLOGY KARNATAKA
SRINIVASNAGAR, SURATHKAL, MANGALORE - 575 025, INDIA

Acknowledgements

First and foremost, I would like to express my heartfelt gratitude to Lord Shiva, my divine mentor, for bestowing His endless grace and kindness.

I would like to thank my parents, Mr. Madhukara Nayak and Mrs. Sridevi, my sisters, Mrs. Sushma and Ms. Madhushree, my brother-in-law, Dr. Harishkumar Kamat, and my husband, Dr. A. Manoj, for standing by me like a rock through this entire phase. They have always guided me towards the right path regardless of the adversities faced, and instilled in me the value of standing for the truth. I wouldn't have traversed this journey without their unwavering support, love, and affection. I will be eternally grateful to them.

My heartfelt thanks goes to my mentor, Prof. Seetharam Nayak, from the Department of Civil Engineering at NITK. He has been instrumental in helping me navigate one of the toughest battles of my life, providing constant support and words of encouragement. Words alone cannot convey my gratitude for what he has done for me.

I would like to express my heartfelt and immense gratitude to my research guide, Prof. D. N. Gaonkar, for his unwavering support, kindness, and continuous encouragement. He has not only been a source of inspiration but has also shown what it means to be a true leader and a compassionate human being. I have reached this point solely due to his constant encouragement and his immense faith in me. I will remain forever indebted to him.

I would like to express my sincere gratitude to Prof. Vidya Shetty, Academic Dean, NITK Surathkal for her exceptional help and support. I will always value the kindness she extended to me. I am extremely thankful to Prof. G. S. Punekar for the invaluable support he provided me.

I am immensely grateful to the efforts put in by the learned members of my Research Progress Assessment Committee, Prof. B. Venkatesapermul and Prof. Annappa for consistently monitoring my progress and giving important suggestions.

The Electrical Engineering Department at NITK has offered me an ideal environment and excellent facilities for conducting my research work. For this, I would like to thank all the HOD's during the tenure of my work and all the teaching and non-teaching staff for their full co-operation and assistance. I also extend my thanks to the staff members from library, administration and academic sections of NITK.

I want to express my loving thanks to my childhood friends, Mrs. Ramya Vytla, Mr. Naren Tadepalli, Mr. Madhusoodhan Acharya, Mrs. Swarna Prabhu, and Ms. Kavya Prabhu, for their constant support, for being there for me at any hour, and for consistently lifting me up in times of need. Their friendship is a precious gift, and I deeply cherish it.

I wish to express my heartfelt thanks to Dr. Teena Johnson, Dr. Mir Khadim Aalam, Dr Pavana Prabhu, Dr. Krishna Rao, Mr. Anvit Khare, Mr. Asif Abdullah, Mr Vikas Singh, Mrs. Nisha K. S., Mr. Subhradip Mondal, Mr. Amal Lazar and my other colleagues for their help, discussions, useful suggestions and keeping me motivated throughout my research work.

I am deeply grateful to my cousins, Dr. Shriram Marate and Dr. Sunaina Patil for their support, assistance, and encouragement throughout my Ph.D. journey.

I am sincerely thankful to my uncle, Mr. Shridhar Nayak, and aunt, Mrs. Bharathi, for being an incredible support system.

My nieces Shreya, Eesha, Achintya, Hima and my nephew Aaryan have been wonderful companions and sources of stress relief. My parents in law, Mr. Achutha Prabhu and Mrs. M. B. Yashodha, my brothers in law, Mr. Ashok Prabhu and Dr. Chethan B. A., and my sisters in law, Mrs Geetha Borker and Mrs Priya, have been a great source of support and encouragement. I wholeheartedly thank each one of them.

I thank all those who helped me directly or indirectly for the successful completion of this thesis.

Once again, I humbly bow to Lord Shiva, deeply grateful for His boundless grace.

NITK-Surathkal Rashmi

Abstract

A global trend in the growth of power systems is to build interconnections with the aim of achieving technical, economical and environmental benefits. The interconnections facilitate exchange of power between different regions or countries improving the utilization, flexibility, power quality, efficiency of transmission and emergency support. High Voltage Direct Current (HVDC) systems emerge as a compelling and efficient solution for long-distance power transmission, asynchronous system interconnection, and renewable energy integration. As offshore wind generation is exploited at increasing distances from shore, HVDC stands out as the preferred transmission method. Offshore wind farms equipped with Direct Drive Permanent Magnet Synchronous Generators (DD-PMSG) are drawing increased attention due to their advantage over other variable speed technologies. Voltage Source Converter based High Voltage Direct Current (VSC-HVDC) links are considered the most suitable option for transferring power to the onshore system. The rapid development of VSC-HVDC based offshore wind farms have highlighted the need for these stations to synchronise with the grid independently and provide inertial support, especially as grid strength declines, rendering phase-locked loops (PLLs) ineffective. In this context, the research work deals with the systematic analysis of Line Commutated Converter based High Voltage Direct Current (LCC-HVDC) links, Voltage Source Converter based High Voltage Direct Current (VSC-HVDC) links and integration of VSC-HVDC based offshore wind farms into multi-machine systems.

Specifically, the study presents a performance analysis of synchronous and asynchronous multi-machine systems using tie-lines as LCC-HVDC links. Detailed inferences are drawn for the systems subjected to various dynamic events in comparison to systems with Thyristor Controlled Series Capacitor (TCSC) lines. The effect of variation of synchronous tie-line power levels on the modal behaviour is investigated. The asynchronous system modes are analysed with reference to the modes of its synchronous counterparts. The impact of VSC-HVDC active and reactive power controls on frequency controllers is assessed. The effect of feedforward and feedback active power loops are examined through bandwidth analysis. The influence of reactive power controllers on the performance of frequency controllers is also studied. Additionally, a simplified model of VSC-HVDC link is proposed that can be efficiently used for analysis of links embedded in large AC systems. This model offers lesser modelling complexity and computation time, enhancing efficiency in analysis.

Following the above analysis, the integration of VSC-HVDC connected DD-PMSG based offshore wind farms into multi-machine systems is explored. A novel approach for power flow and initial condition calculations is proposed to facilitate dynamic analysis of the system. For three cases of the most commonly specified quantities of the wind farm, efficient methods have been described. This approach enables the user to build the model in any basic graphical dynamic modeller and numerical computational software without requiring power system toolboxes or electromagnetic transient packages. Case studies and simulations are conducted to verify the proposed technique. The work further presents a novel approach for grid synchronisation and inertial support from VSC-HVDC based offshore wind farms. The DC capacitor dynamics are utilised to imitate the rotor dynamics of a synchronous generator for synchronisation, while inertia support is derived from the DC capacitor energy and the hidden inertia of the offshore wind farm. A time constant based approach employing two distinct DC voltage tolerance bands for the control is proposed. This leads to improved inertial response and a very easy selection of controller parameters. The effectiveness of the strategy has been proved in high impedance and low inertia systems. MATLAB/SIMULINK has been used for the study.

Keywords: HVDC; frequency control; multi-machine systems; PMSG; grid synchronisation; inertial control; asynchronous systems

Contents

List of Figures

List of Tables

Abbreviations

AC : Alternating Current
CSC : Current Source Converter
CC : Current Control
COI : Centre of Inertia
DC : Direct Current
DD-PMSG : Direct Drive Permanent Magnet Synchronous Generator
DFIG : Doubly Fed Induction Generator
EMTP : Electro-magnetic Transient Program
GSC : Generator Side Converter
GSVSC : Grid Side Voltage Source Converter
HVDC : High Voltage Direct Current
IGBT : Insulated Gate Bipolar Transistor
LCC : Line Commutated Converter
MPP : Maximum Power Point
MPPT : Maximum Power Point Tracking
MSC : Machine Side Converter
MTDC : Multi Terminal Direct Current
OWF : Offshore Wind Farm
PMSG : Permanent Magnet Synchronous Generator
PLL : Phase Locked Loop
PSCAD : Power Systems Computer Aided Design
PCC : Point of Common Coupling
PMU : Phasor Measurement Unit
pu : Per Unit
SCIG : Squirrel cage Induction Generator
TCSC : Thyristor Controlled Series Capacitor
UHVDC : Ultra High Voltage Direct Current
VDCOL : Voltage Dependent Current Order Limit
VSC : Voltage Source Converter
VSG : Virtual Synchronous Generator
VSWT : Variable Speed Wind Turbine
WPP : Wind Power Plant
WECS : Wind Energy Conversion System
WF : Wind Farm
WFVSC : Wind Farm Voltage Source Converter
WRIG : Wound Rotor Induction Generator
WRSG : Wound Rotor Synchronous Generator
WT : Wind Turbine

Nomenclature

δF	:	Frequency deviation in pu
λ	:	Tip speed ratio of wind turbine
β	:	Blade pitch angle of wind turbine
ρ	:	Air density in kg/m^3
ψ_F	:	Stator flux linkage in pu
ω_r	:	Wind turbine rotor speed in pu
ω_{rB}	:	Base rotor speed in electrical rad/s
ω_{rm}	:	Wind turbine rotor speed in rad/s (mechanical)
ω_{re}	:	Wind turbine rotor speed in electrical rad/s
ω_{gB}	:	Frequency base of grid/multi-machine system in rad/s
A_{WT}	:	Surface area of wind turbine blades in m^2
C_p	:	Performance coefficient of wind turbine
c_1 - c_6	:	Wind turbine coefficients
C_{dc}	:	DC link capacitance
e_{abc}	:	PCC bus voltage in *abc* frame in pu
e_q, e_d	:	d and q axis PCC bus voltage in pu
e_Q, e_D	:	D and Q axis PCC bus voltage in pu
H_i	:	Inertia of i^{th} synchronous generator in s
H_t	:	Inertia of wind turbine in s
H_{mb}	:	Inertia of individual PMSG in s
H_s	:	Inertia of agrregated PMSG in s
I_{Href}	:	LCC-HVDC reference current in pu
I_{Tref}	:	TCSC reference current in pu
I_{TCSC}	:	Current in the TCSC line in pu
i_{abc}	:	VSC current in *abc* frame in pu
i_q, i_d	:	d and q axis VSC current in pu
i_Q, i_D	:	D and Q axis VSC current in pu
i_{cc}	:	DC link current of VSC-HVDC in pu
J	:	Moment of inertia of PMSG
$K_{p_{vdc}}$, $K_{i_{vdc}}$	:	PI constants of DC voltage controller of VSC-HVDC link
K_{p_P}, K_{iP}	:	PI constant of active power controller of VSC-HVDC link

Nomenclature (Continued)

K_{pQ}, K_{iQ} : PI constant of reactive power controller of VSC-HVDC link

K_{pvac}, K_{ivac} : PI constants of AC voltage controller of VSC-HVDC link

$(K_p)_{i_q}$, $(K_i)_{i_q}$: q-axis PI constants of inner current controller of VSC-HVDC link

$(K_p)_{i_d}$, $(K_i)_{i_d}$: d-axis PI constants of inner current controller of VSC-HVDC link

K_{pf}, K_{if} : PI constants of frequency controller

K_{psq}, K_{isq} : q-axis PI constant of inner current controller of MSC

K_{psd}, K_{isd} : d-axis PI constants of inner current controller of MSC

$(K_p)_{eQ}$, $(K_i)_{eQ}$: Q-axis PI constants of voltage controller

$(K_p)_{eD}$, $(K_i)_{eD}$: D-axis PI constants of voltage controller

L_{dc} : VSC-HVDC link inductance in pu

n_b : Total number of buses in the multi-machine system

N_{WT} : Total number of wind turbines in the wind farm

P_{PCC} : Real power at the PCC bus in pu

P_f^* : Modulated power reference in pu

P_c : Real power at VSC bus in pu

P_m : Mechanical power output in pu

P_{WF} : Real power at the wind farm bus in pu

Q_{PCC} : Reactive power at the PCC bus in pu

Q_c : Reactive power at VSC bus in pu

Q_{WF} : Reactive power at WF bus in pu

R : VSC line reactor resistance in pu

R_s : PMSG resistance in pu

R_{dc} : VSC-HVDC link resistance in pu

R_f : Droop controller constant in pu

R_{GSC} : GSC converter line reactor resistance in pu

R_{WT} : Wind turbine radius in m

$sysCOI$: average system frequency / common mode frequency / COI frequency

S_{sys} : Multi-machine system power base MVA

T_m : Mechanical torque in pu

T_{eg} : Electromagnetic torque in pu

Nomenclature (Continued)

T_{TCSC} : Delay constant of TCSC controller in s

T_L : Time constant in s

V_{dr} : LCC-HVDC link rectifier voltage in pu

v_{abc} : VSC converter bus voltage in *abc* frame in pu

v_q, v_d : d and q axis VSC converter bus voltage in pu

v_Q, v_D : D and Q axis VSC converter bus voltage in pu

v_{dc} : VSC-HVDC DC link voltage in pu

v_{sd}, v_{sq} : d and q axis PMSG stator voltages in pu

V_W : wind speed in m/s

X_{max}, X_{min} : maximum and minimum limit of reactances of TCSC controller

X : VSC line reactor reactance in pu

x_{sd}, x_{sq} : d and q axis PMSG stator reactances in pu

Chapter 1

INTRODUCTION

In recent years, the global energy demand has experienced a remarkable surge, while conventional fossil fuel reserves continue to deplete rapidly. This escalating challenge has necessitated a paradigm shift towards cleaner, sustainable, and cost-effective power generation and transmission. In this pursuit, two promising options that have emerged are High Voltage Direct Current (HVDC) technology and Wind Power Plants (WPP). The research work will delve into the significance of HVDC and WPP technology in shaping a more resilient energy landscape.

Industrialization in the major cities of India led to an urgent need of fetching power from generating stations situated at distant remote places. The HVDC transmission systems facilitated this. Five bipole HVDC systems were installed in India till June 2012, namely, Chandrapur - Padghe (1500 MW, ± 500 kV DC), Rihand - Dadri (1500 MW, ± 500 kV DC), Talcher - Kolar(2500MW, ± 500 kV DC), Balia - Bhiwadi(2500 MW, ± 500 kV DC) and Mundra - Mohindergarh(2500 MW, ± 500 kV DC). All the initial five Bipole HVDC transmission systems had voltage level of ± 500 kV DC. The first Back-to-Back HVDC project in India was commissioned in 1989 at Vindhyachal in central India, which has a rating of 500 MW. There are another three Back-to-Back HVDC stations installed in India, namely Chandrapur, Gazuwaka (Vizag) and Sasaram. Recent trend is for Ultra High Voltage DC (UHVDC) transmission by using line-commutated converters for long distance power transmission. There are four bipole UHVDC systems in India namely Champa - Kurukshetra (6000 MW, ± 800 kV DC, 1,365 km, 2 parallel lines 3000 MW each), Raigarh - Pugalur (6000 MW, ± 800 kV, 1,830 km), Biswanath Chariali - Alipurduar - Agra (6000 MW, ± 800 kV, 1,728 km). All the above links are based on line commutated converter (LCC) technology. The LCC-HVDC projects of India are presented in Figure 1.1. The

HVDC connection of about 200km between Pugalur (Tamil Nadu) to Trichur (Kerala) is India's first HVDC link featuring voltage-sourced converter (VSC) technology. The transmission voltage level is ± 320 kV DC and the total capacity is 2000 MW. Moreover, India has also commissioned cross border projects (India - Bangladesh) and many others are in the planning stage.

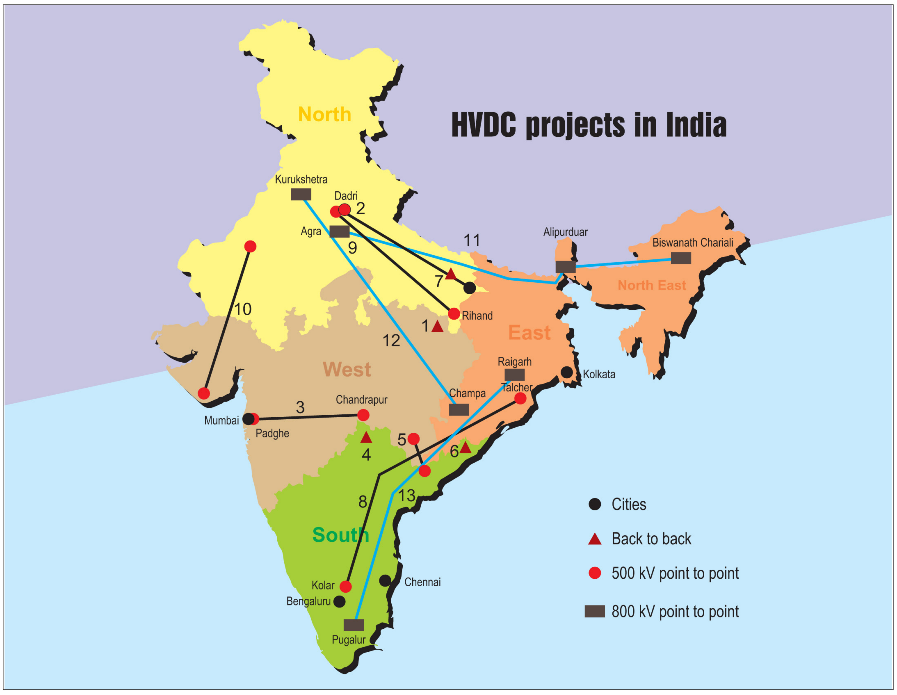

Figure 1.1: LCC-HVDC links in India (Source : https://powerline.net.in)

The world's first 1100 kV DC UHVDC transmission link is between Changji and Guquan in China. This is the biggest HVDC project in the world with a power transfer capacity of 12,000 MW and the length of the link is 3,284 km (Abhijit, 2018).

By the end of 2022, the global cumulative wind energy was nearly 940 GW with 78 GW of new installations in the year 2022. Out of the 78 GW, 68.8 GW are onshore installations and 8.8 GW are offshore installations. India ranks among the top five wind markets in the world with a total installed capacity of around 42 GW. India aims to achieve a substantial increase in its wind energy capacity. By the end of 2030, the country is targeting the addition of over 60 GW of onshore wind capacity and nearly 40 GW of offshore wind capacity. The onshore and offshore global wind capacity is given in Figure 1.2 (GWEC, 2023).

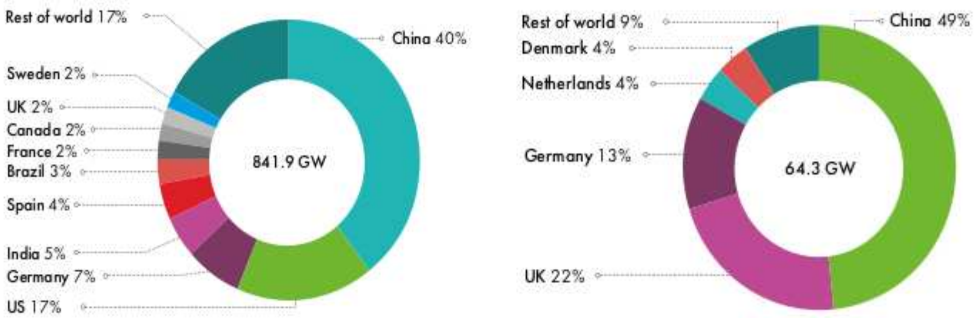

(a) (b)

Figure 1.2: Global wind installations (a) Global onshore capacity (b) Global offshore capacity (Source : GWEC 2023)

By the first half of 2023, India had accumulated wind power installations totaling 43.8 GW. This accounted for approximately 10% of the nation's overall installed power capacity and roughly 30% of its total renewable power capacity. In June 2023, Gujarat took the lead as the foremost wind power installer, contributing to nearly 24.9% of the total cumulative wind installations in India. Tamil Nadu secured the second position with a share of 23.2% of the country's total wind installations. Following closely were Karnataka and Rajasthan, ranking third and fourth, respectively, with 12.1% and 11.9% of the cumulative installations. Maharashtra completed the top five states, accounting for 11% of the total wind power installations. India is also a market with high offshore wind potential. Studies are being undertaken for 1 GW offshore plant in Gujarat with Tamil Nadu being the next focus (MERCOM, 2023).

Due to the bottlenecks in the High voltage alternating systems, HVDC is an attractive solution for the integration of large offshore wind farms to the onshore AC system. VSC-HVDC technology holds great promise for efficiently integrating large-scale offshore wind farms (OWF) into the main power grid. With the increasing number of inverters set to connect to the power system in the coming years, it is becoming increasingly evident that this will have a substantial impact on the stability of the AC system. Loss of system controllability and decrease of system inertia will cause fluctuation in grid voltage and frequency. Thus, the need arises to operate inverters in the same way as conventional generators. It would be expected that WF's and VSC HVDC links provide additional inertia, frequency regulation and damping features to the main AC system. Most of the grid codes around the world put a mandatory requirement on inertial support, frequency regulation, damping contribution from WF's and VSC-HVDC. In countries like Germany where the penetration of wind power is really high very stringent regulations have been put into place.

1.1 HVDC links

Despite alternating current (AC) being the prevailing method for transmitting electrical energy throughout the 20th century, the superiority of HVDC technology has been demonstrated in various specific application areas. Since the early 21st century, the number of HVDC installations per year has steadily risen. Despite the considerable costs associated with converter stations, HVDC is generally favoured for the following applications (Kundur, 1994, Dragan and Khaled, 2015):

- Long-distance, high-capacity power transmission.
- Subsea and extensive cable-based power delivery over extended distances.
- Linking asynchronous AC systems or systems with differing frequencies.
- Enabling controlled power transfer between different nodes within a power network.
- Providing AC grid stability support, ancillary services, and resilience during blackouts.
- Connecting isolated systems such as offshore wind farms or offshore oil platforms.

The primary components of an HVDC transmission system are the converter stations located at either end of the transmission line. The rectifier station converts AC power from the grid into DC power, which is then transmitted via the DC line. At the receiving end, the inverter station converts the DC power back into AC power, which is then fed into the AC grid connected to its terminal.

1.1.1 Types of HVDC link

The origins of contemporary HVDC transmission can be traced back to the Sweden-Gotland installation in 1954. Prior to the mid-1970s, all HVDC systems, including this one, utilized converters based on mercury arc valves. A notable technological leap occurred when solid-state valve converters (thyristors), were introduced. Subsequently, another significant milestone was reached with the advancement of insulated-gate bipolar transistor (IGBT) converters. Presently, the HVDC technology is of two types : HVDC classic and HVDC light technology. The HVDC-classic is based on current source converter (CSC) concept where the basic modules in the AC/DC converters are thyristor-based as shown in Figure 1.3. These converters exclusively endorse the line-commutated converter (LCC) concept and are more widely recognized as LCC-HVDC. HVDC light is based on voltage source converter (VSC) concept where the basic modules in the AC/DC converters are IGBT-based as shown in Figure 1.4.

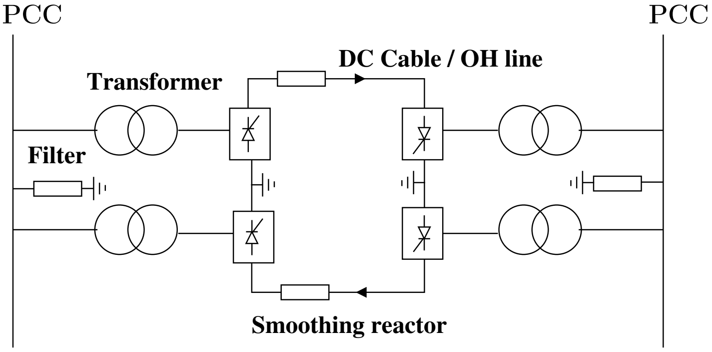

Figure 1.3: Schematic of a LCC-HVDC link

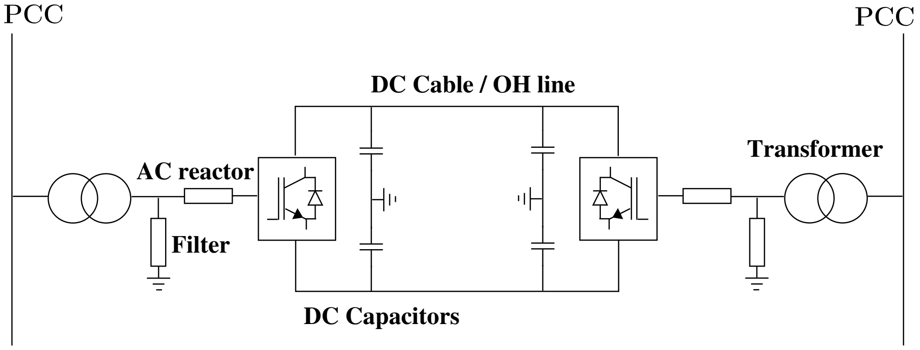

Figure 1.4: Schematic of a VSC-HVDC link

HVDC links are categorized based on the number of DC conductors and the valve arrangement into three types: Monopolar, Bipolar, and Homopolar.

- Monopolar Link: This type consists of a single conductor, with the ground serving as the return path. Ground is utilized as the return path.

- Bipolar Link: Bipolar links comprise two conductors or poles. One operates with a positive polarity, while the other operates with a negative polarity. Typically, the currents in the two poles are balanced, eliminating the need for ground return. Ground return is only utilized in the event of a fault in one of the poles, effectively transforming it into a monopolar link.

- Homopolar Link: Homopolar links consist of two or more conductors with the same polarity, usually preferring the negative polarity to minimize corona losses. Ground always serves as the return path. In the event of a fault in one of the poles, it functions as a monopolar link.

Among these, bipolar links are the most commonly employed HVDC transmission links. The schematic of these link types is illustrated in Figure 1.5.

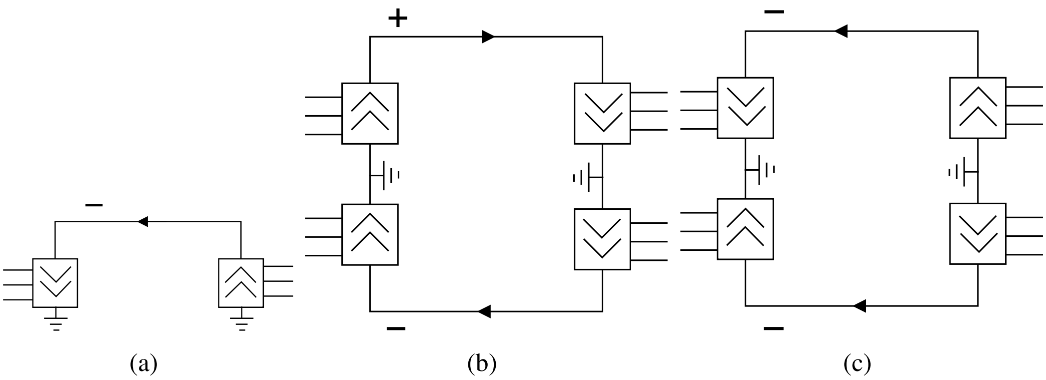

(a) (b) (c)

Figure 1.5: HVDC links based on number of conductors/poles : (a) Monopolar Link, (b) Bipolar Link, (c) Homopolar Link

Based on the arrangement of converters, HVDC links are categorized as Back-to-Back, Point-to-Point, and Multi-terminal, as depicted in Figure 1.6 and explained below :

- Back-to-Back: This type of HVDC link connects two neighboring power systems that have different and incompatible electrical parameters, such as frequency, voltage level, or short-circuit power level. It serves as a bridge between these systems, enabling power exchange.

- Point-to-Point: When there's an economic need to transmit electric power over long distances or between two distinct geographical locations using DC transmission or cables, a two-terminal or point-to-point HVDC transmission system is employed. This allows efficient power transfer over extended distances.

- Multi-terminal: In situations where three or more HVDC substations are situated in separate geographic locations and interconnected through transmission lines or cables, the HVDC transmission system takes on a multi-terminal configuration. This setup facilitates power distribution and exchange across multiple locations.

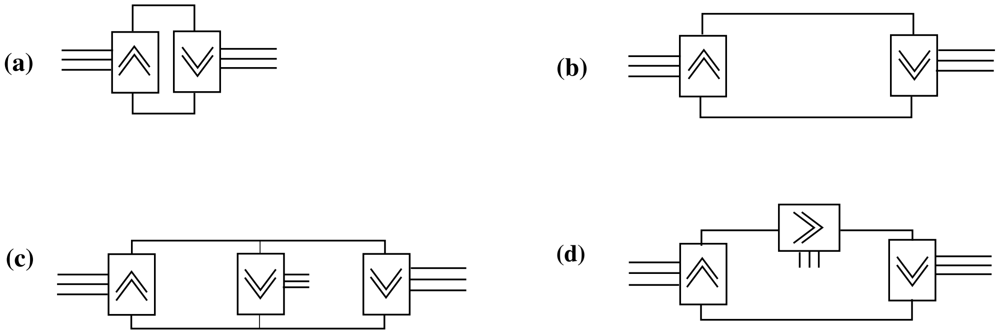

Figure 1.6: HVDC converter bridge arrangements : (a) Back-to-back system, (b) Two terminal system, (c) Multi-terminal parallel system, (d) Multi-terminal series system

1.1.2 Comparison of LCC-HVDC and VSC-HVDC link

The schematics of LCC-HVDC link and VSC-HVDC link is already given in Figure 1.3 and Figure 1.4. Table 1.1 presents a comparison of the two links.

1.2 Wind energy conversion systems

A Wind Energy Conversion System (WECS) is designed to convert the kinetic energy from the wind into electrical power. This process involves the wind turbine rotor rotating in response to the wind's speed, effectively harnessing mechanical energy. This mechanical power is then used to drive a rotating electrical generator, which in turn generates electrical energy. The block diagram of WECS is given in Figure 1.7.

1.2.1 Wind turbine components

A wind turbine (WT) comprises various components essential for energy conversion. Presently, horizontal axis wind turbines dominate the field of WT applications. This type of WT consists of a tower supporting a nacelle, which is positioned atop the tower. The nacelle

Table 1.1: Comparison of LCC-HVDC and VSC-HVDC based links

	LCC - HVDC	VSC-HVDC
Switching device	Thyristor	IGBT
Turn ON and OFF	Turn ON by control action and turn OFF by external circuit	Both Turn ON and OFF by control action
Station size	Large	Small (around 50% of LCC)
Reactive power demand	Yes	No
Reactive power control	Limited (with additional cost)	Continuous and inherent (without additional cost)
Switching losses	Negligible	High
Independent control of active and reactive power	No	Yes
Harmonics	Generates significant low order harmonics	Doesn't generate low order harmonics
AC filter	Large	Small
DC filter	Might be required	Rarely used
Commutation failure	Present for AC disturbances	No
Power Reversal	Voltage polarity needs to be reversed	Current direction needs to be changed
Black Start capability	Requires additional equipment	Inherent

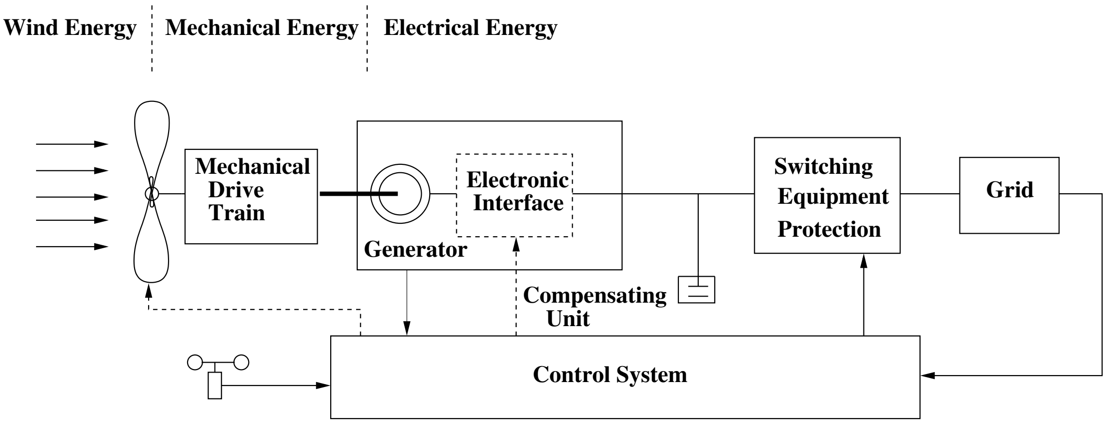

Figure 1.7: Block diagram of a WECS

essentially functions as the WT's machine room and is designed to rotate on its tower with the assistance of a yaw drive mechanism, allowing it to align with or deviate from the wind direction, particularly in the face of high wind speeds. Within the nacelle, critical components include the rotor, gearbox (if present), generator, and the control system.

Horizontal axis wind turbines designed for electricity generation typically feature two or three blades affixed to a rotor hub, which, in turn, is installed on the primary low-speed shaft. The transfer of mechanical energy to the generator occurs through the drive train, encompassing the shaft, bearings, and gearbox (if utilized). In contemporary WT technology, modern variable speed wind turbines (VSWT) are often gearless, utilizing direct drive systems. This design eliminates the need for a high-speed shaft, resulting in a smaller sized nacelle.

Additionally, beyond the components directly engaged in power conversion, there exist other vital elements within a WT system that play a significant role in ensuring its effective and dependable performance. These encompass the pitch system (which includes stall and pitch mechanisms), wind speed measurement devices, mechanical braking systems, power distribution cables, heat dissipation mechanisms, protective measures, power converters, and control systems, among others (Bin Wu et al., 2011).

1.2.2 WECS configurations

WT's can either operate with fixed speed or variable speed. There are four standard WT types. Type 1 is of fixed speed type and Type 2, Type 3, Type 4 are variable speed wind turbines (WECC task force, 2010, Ackermann, 2005).

1. Type-1 - Fixed speed
   This configuration represents a fixed-speed WT featuring an asynchronous squirrel cage induction generator (SCIG) connected to the grid through a transformer, illustrated in Figure 1.8. Type 1 WT's, as depicted here, often incorporate capacitor banks to facilitate reactive power compensation.

   For a considerable duration, fixed-speed WECS, whether employing active or passive stall mechanisms, have been the prevailing technology in the wind power industry. These systems have demonstrated their reliability in practical operation and naturally offer inertial response. However, their primary limitation lies in the fact that the constant generator speed doesn't allow for significant control flexibility.

2. Type-2 : Limited variable speed.
   This configuration represents limited VSWT, featuring a variable generator rotor resistance, as illustrated in Figure 1.9. In this configuration, a wound rotor induction

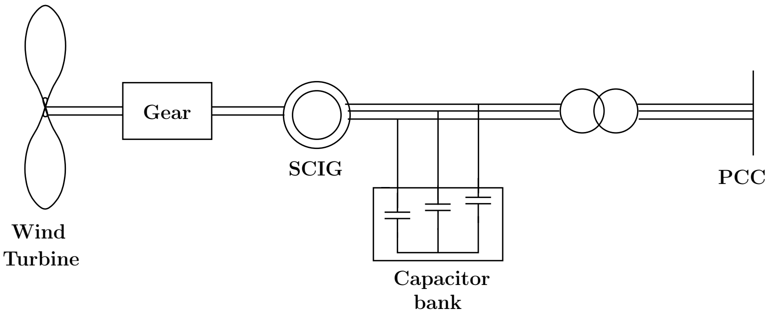

Figure 1.8: Type-1 WECS

generator (WRIG) is utilized. By utilizing power electronics, it becomes possible to modify the rotor resistance, thereby enabling control over the slip.

The extent of dynamic speed control achievable with this setup depends on the magnitude of the variable rotor resistance. However, as a general guideline, the speed adjustment range typically falls within the range of 0% to 10% above the synchronous speed.

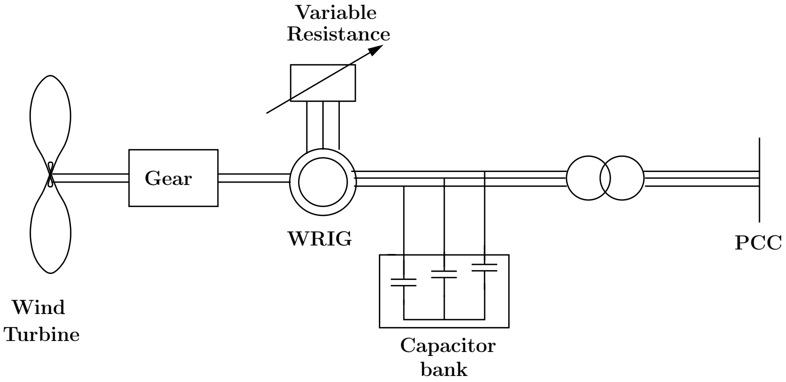

Figure 1.9: Type-2 WECS

3. Type-3 : Variable speed with partial scale frequency converter.
   This configuration, often referred to as the Doubly Fed Induction Generator (DFIG) concept, represents a specific limited VSWT design employing a wound rotor induction generator (WRIG) and incorporates a partial-scale frequency converter, rated at approximately 30% of the nominal generator power, within the rotor circuit, as depicted in Figure 1.10.

In this setup, the stator windings are directly connected to the three-phase grid with a constant frequency, while the rotor windings are linked to the grid through a pair of back-to-back VSCs. Typically, the achievable speed range spans from synchronous speed -40% to +30%. The utilization of a smaller frequency converter in this configuration enhances its economic appeal. However, it is worth noting that this concept comes with challenges related to the use of slip rings and the need for robust protection mechanisms in the event of grid faults.

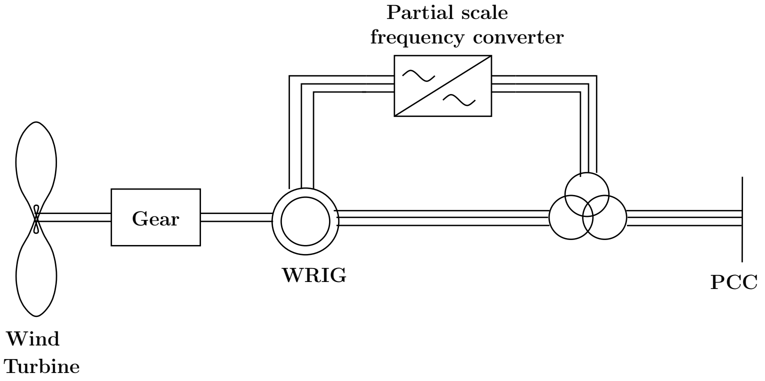

Figure 1.10: Type-3 WECS.

4. Type 4 : Variable speed with full scale frequency converter.
   This configuration corresponds to the full VSWT setup, where the generator is linked to the grid through a full-scale frequency converter, as depicted in Figure 1.11. In this setup, you have the flexibility to use either an induction generator or a synchronous generator.Further, the synchronous generator can take two forms: a wound-rotor synchronous generator (WRSG) or a permanent-magnet synchronous generator (PMSG). The PMSG configuration is particularly promising because it operates using permanent magnets, eliminating the need for an excitation energy source. Additionally, the salient pole design of a PMSG operates at low speeds, allowing for the elimination of the gearbox. This represents a significant advantage in PMSG-based WECS since gearboxes are known to be sensitive components in wind power systems. A similar advantage can be achieved by utilizing direct-drive PMSG (DD-PMSG).

VSWTs particularly Types-3 and 4, offer an exceptional degree of controllability, enabling the extraction of maximum power across a wide range of wind speeds. Notably,

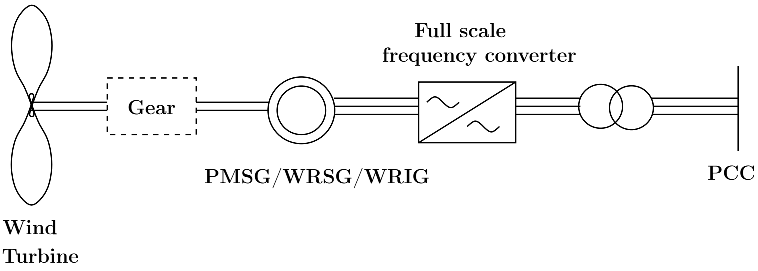

Figure 1.11: Type-4 WECS

these systems allow for the complete decoupling and independent control of active and reactive power, enhancing their flexibility. VSWTs have established a dominant presence in the market, particularly in the megawatt class. However, it's important to note that, especially in the case of Type-4 WT's, there exists electrical decoupling between the generator and the grid. This characteristic distinguishes them from conventional synchronous generators and they cannot contribute to the power system's inertia in the same manner.

1.3 Literature Survey

1.3.1 Modelling, control and performance analysis of HVDC links

Synchronous AC links combined with FACTS devices especially Thyristor controlled series capacitors (TCSC) have long proven to be a major success in increasing the power transfer capability and in providing a reliable controllability (Hingorani and Gyugyi, 2000, Padiyar, 2009). For large AC systems with transmission system spreading over thousands of kilometers, use of HVDC links along with meshed AC interconnections is found to be economically beneficial. In the asynchronous interconnections, HVDC links are the only practical solution to interconnect AC systems operating at different frequencies. In Indian power system, the southern grid was asynchronously connected to the rest of the grid before connecting it synchronously in December 2014 (Pritwish et al., 2015). With the increased penetration of solar PV power system and WECS into the grid and interconnection of such low inertia grids in-turn have led to the usage of asynchronous links prominently. Even in micro-grids, different types of renewables are interconnected through asynchronous ties. In these grids, frequency control and handling of large disturbances in the presence of renewables are the major concerns (Padiyar and Kulkarni, 2019, Chen et al., 2018). In this context, in (Miniyuan et al., 2015) and (Bandaru et al., 2018), an asynchronous system is simulated with VSC-HVDC links. In (Hu and Mao, 2005), LCC-HVDC are compared with VSC-HVDC links. The feasibility of integrating weak grids via LCC-HVDC link has been investigated in (Yong et al., 2012, Yogarathinam et al., 2017, Vennelaganti and Chaudari, 2018). The modelling of LCC-HVDC links is well established in (Teena and Shubhanga, 2017) and (Kundur, 1994). For general purpose power system stability studies response type model of LCC-HVDC is adopted. It provides a compromise between simulation accuracy and modelling efficiency. In most studies involving asynchronous HVDC systems, load flow analysis is typically performed using electromagnetic transient software packages. This approach is favoured over rigorous mathematical calculations. Additionally, there is potential for more robust and comprehensive analysis of the dynamic behavior and modal characteristics of LCC-HVDC systems in multi-machine environments.

A generalized dynamic model for a VSC-HVDC link is presented in (Stijin et al., 2010) which can be implemented for every conceivable topology of DC circuit. The time lag of converter's power electronics and DC voltage controller are addressed using time delays. The performance of a VSC-HVDC link crucially depends on its control system. Additional controllers of VSC-HVDC for system support have been widely discussed in the literature (Latorre et al., 2008, Preece et al., 2013, Xiao and Tang, 2015, Sigrist et al., 2015, Zhiyong et al., 2017). In (Latorre et al., 2008), control strategies of VSC-HVDC are examined for transient stability improvement and damping of low frequency oscillations of system using Lyapunov control functions. However, severely simplified model of VSC-HVDC is used for the study. Damping control strategies for stability improvement is discussed in (Xiao and Tang, 2015). The research is based on direct power-angle control of converters which may not be practical. Vector dq current control is the most widely used control due to its inherent advantages. The impact of frequency controllers on the transient stability of the system is analysed in (Sigrist et al., 2015). The primary frequency capability of VSC HVDC on three different asynchronous interconnections in North America is given in (Zhiyong et al., 2017). All the above investigations focus primarily on the dynamics of the AC system. In (Li S. et al., 2016), the effects of VSC-HVDC controllers on AC and DC side system responses is highlighted through modal analysis and transient simulations respectively. The impact of VSC control parameters on network stability is discussed in (Giddani et al., 2012) by presenting a detailed state space model of the system. However, the interactions between controllers and the possible effects as a result of this is not discussed. The impact of different types of reactive control schemes on power transfer capability is discussed in (Bernat and Preece, 2019). The stability and robustness of active power control system is examined with emphasis on the rectifying operation of the converter in (Wang W. et al., 2014). The effect of feedforward and feedback real power loops based on vector current control is demonstrated in a detailed manner. The impact of the power loops on voltage droop control is also investigated. There is potential for delving deeper into the analysis of the effect of active and reactive power control systems on frequency controllers, an aspect that has not yet been thoroughly investigated.

For small signal stability study and power system analysis of large scale systems, most literature model VSC-HVDC link merely as power injections at the AC buses to which it is connected (Abedin et al, 2021, Agnihotri et al, 2017, Asvapoositkul and Preece, 2020). However, such a model doesn't reflect the dynamic performance of the system. The feasibility of this model is checked in (Asvapoositkul and Preece, 2020) where the authors provide an index to detect regions where the simplified model can be utilised for small signal stability analysis. The work shows that the accuracy of the results can vary based on the location and type of VSC control used. Well-established VSC-HVDC models are presented in (Jef Beerten et al., 2014, Cole and Ronnie, 2011). In (Jef Beerten et al., 2014), a simplified model is also discussed by eliminating DC current dynamics while retaining DC voltage as state variable. In (Cole and Ronnie, 2011), smallest time constants of the full-order model are neglected to arrive at a simplified model with less number of differential equations. However, the time constant corresponding to DC capacitors is maintained as it is treated as a dominant element in the DC circuit. The above models reproduce an overall dynamic performance of the system. VSC-HVDC link represented by controlled voltage sources behind reactors is presented in (Shewarega and Erlich, 2014). In this work, the converter current is not explicitly modeled and voltage value of the source is directly obtained from the inner controllers. The DC link is represented by an equivalent capacitance. Similar work is carried out in (Jahan et al, 2017) to minimize simulation time in analysis of HVDC links connecting offshore wind farms to main grid. DC grid modeled as aggregated capacitance is implemented in (Meer et al, 2016) for a multi-terminal direct current (MTDC) system to investigate its feasibility in transient stability simulations. But the model performs inaccurately for very large disturbances. An optimal reduction algorithm is used for model reduction in (Wang T. et al, 2019). However, it is deduced in frequency domain over a required operating point. From the literature review, simplified VSC-HVDC models are either represented as power injections without any other dynamical representation or are modeled with partial simplification of both DC circuit and converter system. Not much effort has been put into presenting a simplified model that preserves the important aspects of the VSC-HVDC. Furthermore, there is a significant research gap in terms of a simplified model which can capture the effect of different types of VSC controllers on an AC system's behaviour.

1.3.2 Modelling and integration of VSC-HVDC based type-4 wind farms into multi-machine systems

In (Chia-Nan et al., 2014), a well-established dynamic model of a PMSG wind turbine is described and simulations for a single PMSG wind turbine feeding grid are performed. The operation and control strategies of VSC-HVDC connected PMSG wind farms connected to grid are discussed in (Muyeen et al., 2010). The modelling is carried out in PSCAD/EMTDC. In (Xudan et al., 2018), control strategies to provide synthetic inertia through VSC-HVDC connected offshore wind farm is discussed where the onshore power system is treated as a single synchronous generator. A complete transfer function model of an ensemble of OWF-MTDC-AC system is developed in (Hua et al., 2019). Aggregated models of type-4 wind farm is described in (Mercado et al., 2015). It elaborates equivalent wind, approximate mechanical torque and equivalent wind turbine rotor methods for aggregation of PMSG based wind farm. The author concludes that below nominal conditions of wind speed the response of the models are identical to the detailed model. In (Roland and Lukasz, 2020), the advantages of HVDC over HVAC technology in relation to transmission distance are given where a new break-even distance for offshore installation is proposed. A comparison of HVDC offshore technologies and various configurations of DC-DC offshore wind farms is discussed. A review of applications of VSC-HVDC technology for offshore wind integration has been presented in (Asimenia et al., 2016). The grid code requirements and various converter controls are discussed in the paper.

Power flow methods with VSC-HVDC systems have been discussed in (Pizano et al., 2007, Wei et al., 2020, Ye et al., 2020, Kamel et al., 2019). The load flow techniques of systems with wind farms have been presented in (Rahim, 2011, Divya et al., 2006, Zhao et al., 2008, Khan and Bhowmick, 2019, Hennig et al., 2014, Kumar and Thukaram, 2017, Kouadri et al., 2016, Zhou et al., 2019, Yao et al., 2020). In (Rahim, 2011), the integration of fixed speed and DFIG based WECS to multi-machine system is analysed in very limited detail with no discussion on the initial working condition calculations of the system that can assist the dynamic analysis. Steady state behaviour of type-4 wind farms connected to distribution systems has been studied in (Divya et al., 2006) to assess their impact when used as DG sources. Based on the given wind speed, the maximum power obtained from the power characteristics of the turbine is considered as the final output. The authors do not go into the intricate details of the wind farm model, nor do they explore VSC-HVDC-based wind farms. Sophisticated power flow models are described in (Zhao et al., 2008, Khan and Bhowmick, 2019, Hennig et al., 2014, Kumar and Thukaram, 2017, Kouadri et al., 2016, Zhou et al., 2019, Yao et al., 2020). In (Zhao et al., 2008), the wind farm network is divided into several local networks and the loadflow is calculated from one local network to another. Iterative methods for converter losses and converter control are proposed and included in the loadflow analysis. Optimal power flow techniques are proposed in (Kouadri et al., 2016, Zhou et al., 2019, Yao et al., 2020). Rigorous mathematical formulations are used to develop the models. However, such extensive methodologies are not required when the study concentrates more on the dynamic applications and control aspects of these systems. In such cases, in order to avoid the calculations of power flow and initial conditions of such systems, most researchers move towards electromagnetic transient packages (Zeni et al., 2016, Yousef et al., 2017, Kabsha et al., 2020).

1.3.3 Inertial and grid synchronisation capabilities from VSC-HVDC based offshore wind farms

In a VSC-HVDC based offshore wind farm integration, the candidates for providing inertia support are the HVDC capacitor and the kinetic energy stored in the generators of offshore wind farm. Due to the decoupling nature of VSC-HVDC, the frequency information of the onshore power system is not directly transferred on to the offshore side. In order to provide for this, the literature suggests various methods for control that can be broadly classified as communication based control and communication-less control (Lu et al., 2021). The communication based control is ruled out due to the communication delays, reliability issues and large costs.

The communication less control can be further classified as phase locked loop (PLL) based control which follows the grid and control without PLL where VSC station forms the grid. In (Jiebei et al., 2013), the electro-static energy stored in the HVDC capacitor is used to provide inertia support. Though it provides a very quick support, the energy is limited as it depends on the maximum allowable DC voltage deviation which further depends on insulation and switching requirements. Also, a larger inertia would require a large capacitor which is not practical. Hence a combination of energy from both HVDC capacitor as well as the kinetic energy from offshore wind farm would prove beneficial. Coordinated control strategies are widely discussed in (Kabsha et al., 2020, Zeng et al., 2020, Xudan et al., 2018, Adeuyi et al, 2017, Liu and Chen, 2015, Ferr et al., 2015, Li et al., 2014, Silva et al., 2012). The coordinated strategies either adopt simultaneous or cascaded control to release the inertial energy. The DC voltage of the grid side VSC (GSVSC) of the VSC-HVDC is used to transfer the frequency information from onshore to offshore grid as any variation in the frequency of the onshore grid is immediately reflected in the GSVSC DC voltage. The commonality in all the above strategies being the PLL for grid synchronisation, it is well known that integration of VSC into grids with low short circuit ratios can degrade the dynamic performance of conventional PLL. This in turn degrades the performance of DC voltage control as well as the current vector control. To resolve this, virtual synchronous generator (VSG) based approach with grid forming capability has been applied to the VSC-HVDC based Offshore Wind Farm (OWF) for better stability.

On a general note, VSG refers to the use of synchronous generator rotor equation dynamics to achieve grid synchronization. This approach involves setting a fixed power reference that imitates the rotor dynamics, with any power deviations being compensated for by the sending end system (Miniyuan et al., 2015, Zhong and Weiss, 2011, Zhang et al., 2010, Ratnam et al., 2020). However, for offshore wind farms, the system is designed to operate on the principle of maximum power point tracking (MPPT), where a fixed reference at GSVSC would result in a deviation from the maximum power point and would negate the benefits of the offshore wind farm. Researchers have suggested utilizing the inherent behavior of the DC capacitor to facilitate grid synchronization and provide inertial support (Huang et al, 2017, 2018, He et al., 2018, Yuan et al., 2021, Yujun Li et al., 2014, Yang et al., 2018, Renxin et al., 2020) which is apt for VSC-HVDC based OWF. In (Huang et al, 2017), a DC capacitor synchronisation controller namely Visync is proposed which also provides inertial and damping abilities. This work has been further extended to multi-terminal DC links in (Huang et al, 2018) with an additional power droop controller. The above works have been implemented in systems where active power control is allowable and inertia and damping coefficients can be easily tuned and varied. In (He et al., 2018), a similar DC capacitor based virtual synchronous control for grid synchronisation co-ordinated with frequency droop controller to realize frequency regulation from WT is discussed for PMSG based WF directly connected to grid. The work does not discuss on the parameter selection of the inertia and damping constants of the synchronisation controller which is very crucial owing to the limit on allowable DC voltage deviation and the sending end inertial energy source being only kinetic energy of the PMSG WT. In (Yuan et al., 2021), a communication-less cascading frequency regulation scheme is proposed which uses DC voltage - frequency droop based grid synchronisation strategy and uses DC voltage for frequency reflection to a sending end AC system. The strategy is implemented for point to point VSC HVDC link connecting two AC systems. In Yujun Li et al. (2014), the above droop based synchronisation strategy along with additional damping is implemented for a PMSG WT connected to grid. Only the DC capacitor participates in the inertial support and no support is obtained from wind farm. In (Yang et al., 2018), inertial synchronising control with WF support through AC frequency mirroring technique using droop based approach is proposed for a point to point VSC-HVDC based offshore wind farm system. This method does not use the rotor mechanics of synchronous generator for grid synchronisation. An additional damping compensation unit to improve the response is added. The work is further extended to multi-terminal DC links in (Renxin et al., 2020).

1.4 Research gaps and motivation

Upon the onset of a power disturbance within a system, the frequency dynamics are predominantly influenced by the inertial response of the system. In systems with a substantial integration of static-based devices, particularly in the context of weak systems characterized by either high impedance or low inertia, it becomes imperative for these devices to actively contribute to the inertial response. Given the increasing emphasis on the integration of VSC-HVDC based offshore wind farms into multi-machine systems, it is crucial that these offshore wind farms and VSC converters actively participate in the inertial regulation process. However, achieving this goal first necessitates a comprehensive understanding of HVDC links and wind farms within the broader context of multi-machine systems.

A thorough review of the existing literature in the previous section highlighted several key research gaps. Though the modelling of LCC-HVDC links are well established, there is a notable absence of an in-depth dynamic and eigenvalue analysis of these links in multi-machine systems in comparison to its existing counterparts such as TCSC. Further, a major task in analysing asynchronous HVDC systems is in performing its load flow analysis. In order to avoid load-flow of such systems, many researchers move towards electromagnetic transient packages such as PSCAD and EMTP to arrive at the operating point. There is a lack of description of a simple method to perform loadflow analysis of asynchronous systems. As the research would delve deeper into the frequency stability of systems, the controller interactions of primary VSC-HVDC controls on the basic ancillary frequency controls is worth to be looked into. Further, the literature lacks the development of an efficient and simplified VSC-HVDC model suitable for large power systems, aiming to reduce complexity and simulation time. While the integration of offshore Type-4 wind farms into multi-machine AC systems has been extensively discussed in previous research, there is a dearth of simple power flow and initial condition approaches that can help the dynamic model to be readily implemented in commonly available modelling packages. Another significant challenge arises from the untapped potential of harnessing inertia in offshore wind farms due to the decoupling nature of VSC-HVDC links. By using proper control methodology this has to be tapped. However, there is always a time delay associated before the wind farms can react, which can be pitched in by the HVDC capacitor of the VSC-HVDC link initially. Given the restrictions on the maximum DC voltage deviation, it is well known that the HVDC capacitors can only provide limited amount of inertial power. Large voltage deviations are not advisable for longer periods of time with respect to reliable operation, safety of capacitors and efficient transfer of power. It would be worthwhile to develop a control to enhance the utilization of DC capacitor while keeping the restrictions in mind. The literature review reveals that there are limited existing control strategies that deal in particularly with synchronisation and inertial capabilities of VSC-HVDC based offshore wind farms leaving room to create a more robust controller.

To address these concerns, this study undertakes a comprehensive exploration of HVDC links, delving into their modal and dynamic analysis, as well as control interactions, encompassing both LCC and VSC-based systems. An attempt is made to introduce a simplified VSC-HVDC model, aiding in the analysis of large AC systems. Furthermore, a simplified approach is presented for the load flow analysis of asynchronous HVDC systems and VSC-HVDC-based offshore wind farms in the context of multi-machine systems. Lastly, a novel grid synchronization and inertial controller is proposed specifically tailored for VSC-HVDC-connected offshore wind farms.

1.5 Objectives

The extensive literature survey undergone has helped identify several research gaps based on which the objectives of the thesis are formulated as follows :

1. A study of synchronous and asynchronous LCC-HVDC systems investigating their

modal and dynamic behaviour.

2. An analysis on the impact of VSC-HVDC control strategies and modelling intricacy on the performance of multi-machine systems.
3. Development of loadflow and initial condition techniques for VSC-HVDC connected type-4 wind farms embedded in multi-machine systems.
4. A novel technique for grid synchronisation and inertial control of VSC-HVDC based offshore wind farms.

1.6 Author's Contributions

The major contributions based on the work carried out in this thesis are as follows :

1. An exhaustive analysis of synchronous and asynchronous LCC-HVDC links is presented. This includes both the dynamic and modal behaviour of the systems in comparison to system with TCSC line and system with only AC transmission lines. The impact of power level changes on the attributes of the dominant swing modes of the systems is neatly depicted. The effect of forming an asynchronous link is studied by analysing the modes with reference to the modes of its synchronous counterparts.
2. The effect of VSC-HVDC outer real and reactive controls on the behaviour of frequency controllers is analyzed. A simplified VSC-HVDC model that can be applied to links embedded in large power systems where the performance analysis of the AC systems is the main objective of the study is proposed. The model accurately describes the dynamic and modal behaviour of associated AC systems.
3. A unique approach for power flow and initial condition computations of VSC-HVDC connected DD-PMSG wind farms integrated into multi-machine systems, which can aid the dynamic model is proposed. The method allows the complete system dynamic model to be implemented in easily available basic dynamic modelling packages without the need for power system toolboxes or electromagnetic transient packages.
4. A novel approach to achieve grid synchronization and inertial capabilities in VSC-HVDC connected offshore wind farms that supply power to weak power systems is proposed. The controller demonstrates superior effectiveness in providing grid synchronization and inertial response when compared to existing droop-based methods.

1.7 Organization of the thesis

This thesis is divided into six chapters and are detailed below:

1. **Chapter 2**: analyzes performance of synchronous and asynchronous LCC-HVDC links in multi-machine systems. The study presents load flow technique for asynchronous HVDC system, investigates the influence of dynamic events on system performance, examines the impact of synchronous tie-line power levels on modal behaviour, and analyses the modal behaviour in asynchronous systems.

2. **Chapter 3**: discusses the modelling and control of VSC-HVDC systems integrated into multi-machine systems, analyzing the impact of active and reactive power control loops on frequency controllers. It also introduces a simplified VSC-HVDC model for use in analysis of large power systems.

3. **Chapter 4**: describes a simple approach for computing power flow and initial conditions for VSC-HVDC connected PMSG wind farms integrated into multi-machine systems enabling dynamic modelling of the system in basic software tools.

4. **Chapter 5**: introduces an innovative approach for achieving grid synchronization and harnessing inertial support from VSC-HVDC connected PMSG based offshore wind farms in weak systems. It utilizes DC capacitor dynamics to mimic the behavior of synchronous generators, enabling rapid grid synchronization and tapping into both DC capacitor and offshore wind farm inertia. The proposed controller is validated by comparing it with existing control strategies.

5. **Chapter 6**: summarizes the contribution of the work presented in this thesis. In this chapter the future research work which can be undertaken related to the thesis is also discussed.

Chapter 2

LCC-HVDC LINKS IN MULTI-MACHINE SYSTEMS

2.1 Introduction

Line Commutated Converter based High Voltage Direct Current technology, a cornerstone of modern power transmission, traces its origins to mid-20th century innovations in electrical engineering. In today's energy landscape, LCC-HVDC systems serve as vital conduits for cross-border power exchange, facilitating grid stability through asynchronous interconnections, and fostering energy resilience in the face of evolving demand patterns. With a proven track record and ongoing technological advancements, LCC-HVDC remains a fundamental pillar in providing sustainable and robust power networks.

In this chapter, in order to get better insight to the synchronous and asynchronous LCC-HVDC links, even with regard to their modal behaviour, LCC-HVDC based synchronous and asynchronous system are simulated and analysed. Additionally, a comparison is made by introducing systems with Thyristor Controlled Series Capacitor (TCSC) line as a tie-line. In such a context, LCC-HVDC link and a TCSC with current control are simulated with response type models. A multi-slack bus method is presented for load flow analysis of asynchronous systems where a slack bus is chosen in each area. This method can be used readily in MATLAB/ SIMULINK environment to perform further dynamic analysis. Synchronous systems with TCSC/ LCC-HVDC and asynchronous system with LCC-HVDC are simulated to bring out valuable insights on dynamic and modal behaviour. Eigenvalue analysis of interconnected power system involves intensive analytical calculations. However, in the present scenario, a large scale deployment of PMU's in the grid have lead to the ready availability of dynamic information of power systems. With the data available from the PMU's, signal measurement-based mode identification techniques can be applied to obtain the modal information of the systems. Hence, this chapter uses prony analysis, the most popular technique for ring-down signal measurement and presents the modal information of the systems.

2.2 System model

In this section, the load flow algorithm, prony method and power system models used in the study is described in detail.

2.2.1 Multi-slack bus AC-DC load flow algorithm

A power system containing asynchronous HVDC links divides the entire system into independent AC subsystems with different nominal frequencies. Therefore, while performing load flow, a slack bus is required in each subsystem. In this section, a load flow procedure with multiple slack buses to accommodate asynchronous systems is described.

- Let n_b be the total number of buses. The buses in the complete system are numbered from 1 to n_b.
- A slack bus is identified in each of the AC subsystem.
- The voltage magnitude and angle of each slack bus is initialised along with the normal initialisation process of other variables. The angle of the slack bus pertains to the reference angle of the respective subsystem.
- An admittance matrix of the complete system $[Y_{BUS}]_{n_b \times n_b}$ is formed. It is made up of elements of admittance matrices of individual AC subsystems. The Y_{BUS} terms, y_{jk} = y_{kj} = 0 where j,k are set of asynchronous rectifier-inverter bus pairs of the entire system, show decoupling of the AC subsystems. The interconnection is brought out by power injections at the rectifier and inverter buses. This allows for simultaneous solution of loadflow of all subsystems by handling only one matrix as in the conventional load flow. Consider an example of a 4 machine, 11 bus system as shown in Figure 2.1. The buses are numbered from 1 to 11 as shown. An asynchronous link

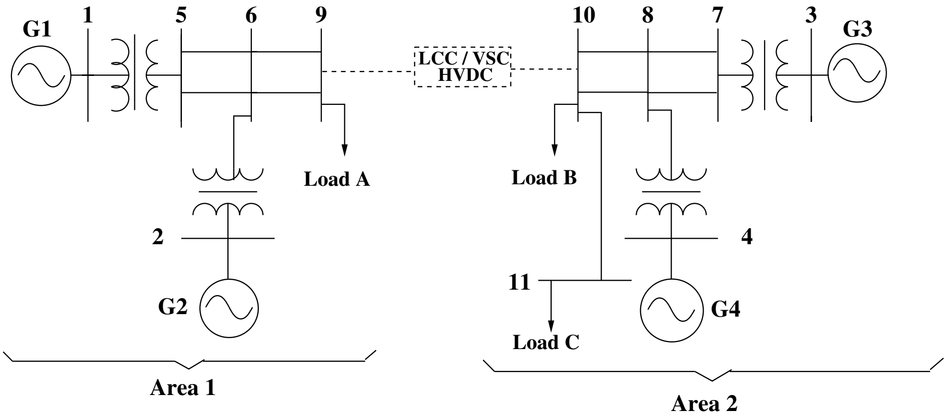

Figure 2.1: 4 machine, asynchronous System

between buses 9 and 10 separates the system into two AC subsystems, area-1 and area-2. The admittance matrix of the complete system is $\left[Y_{BUS}\right]_{11\times11}$. This matrix is made up of elements of individual admittance matrices of area-1 (Y_{A1}) and area-2 (Y_{A2}) i.e.

- $Y_{A1} = \left[Y_{BUS}(i,j)\right]_{5\times5}$ where $i, j = (1, 2, 5, 6, 9)$
- $Y_{A2} = \left[Y_{BUS}(i,j)\right]_{6\times6}$ where $i, j = (3, 4, 7, 8, 10, 11)$

However, they maynot be seen as proper submatrices in Y_{BUS} due to the bus numbering adopted in the system. The decoupling between the two areas in Y_{BUS} are indicated by the terms $Y_{BUS}(9,10) = Y_{BUS}(10,9) = 0$. The interconnection between the two areas are catered by providing power injections at buses 9 and 10.

- The rectifier and inverter bus's, real and reactive power injection vectors (P_{dc} and Q_{dc}) are given as :

$$\begin{aligned} P_{dc} &= \left[P_{dr}; -P_{di}\right] \\ Q_{dc} &= \left[Q_{dr}; Q_{di}\right] \end{aligned} \tag{2.1}$$

where subscripts r and i represent rectifier and inverter respectively and P_d and Q_d are real and reactive power respectively.

- Sequential approach of power flow analysis is used where AC and DC iterations are solved alternatively until the convergence is reached for the entire system. It in turn enables convergence of each AC subsystem.

Upon reaching convergence, the power at the slack buses and line flows are calculated in the usual way. Here, for a i^{th} slack bus, powers are calculated using the current injections obtained from the original Y_{BUS} itself as:

$$P_{si} + jQ_{si} = V_i \sum_{q=1}^{n_b} Y^*_{BUS}(i,q)V^*_q \tag{2.2}$$

Note: For the load flow procedure adopted in the study:

- The asynchronous link can be either of LCC-HVDC based or VSC-HVDC based.
- Any number of asynchronous links can be present in the system.
- The method discussed doesnot require decoupling of the complete system admittance matrix in terms of admittance submatrices of its subsystems. The numbering of the buses can be done in any order.

2.2.2 Response type model of HVDC

Response type model is employed for the HVDC link as detailed in (Kundur, 1994). A HVDC link representation is given in Figure 2.2 and a block diagram representing the response type model is presented in Figure 2.3.

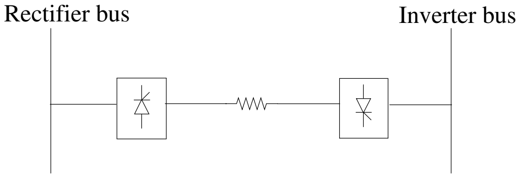

Figure 2.2: Schematic representation of a HVDC link

In this study, current controller is assumed on the rectifier and constant extinction angle control on the inverter. For a desired power (P_{HVDC}) through the link, the reference current (I_{Href}) of the controller is calculated as,

$$I_{Href} = \frac{P_{HVDC}}{V_{dr}} \tag{2.3}$$

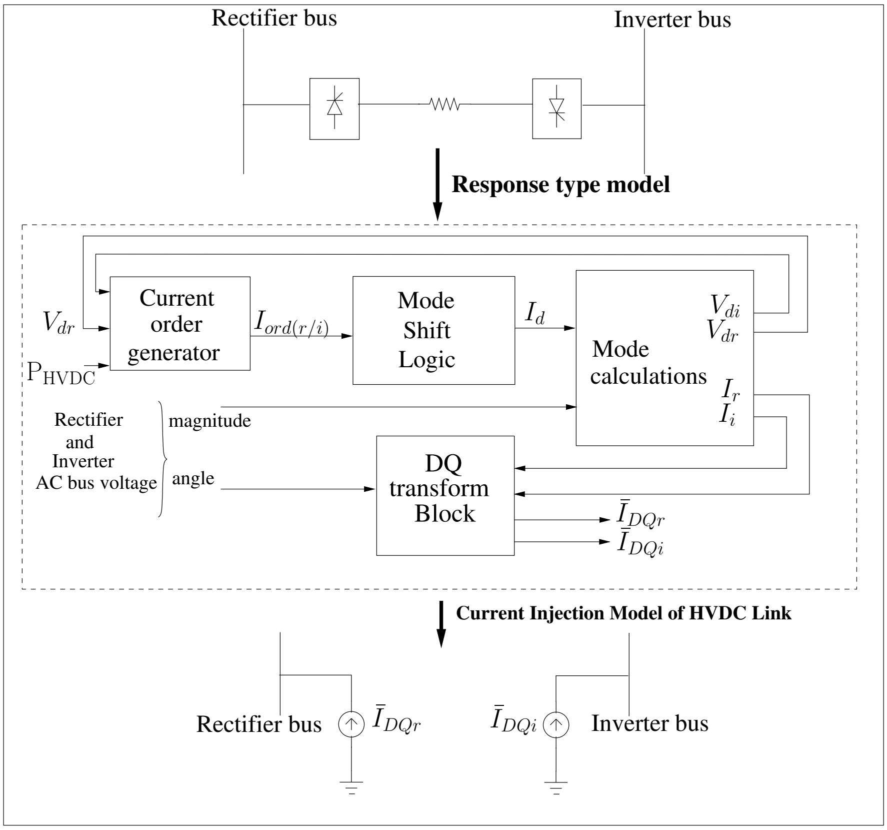

Figure 2.3: Schematic representation of the HVDC response type model

where V_{dr} is the rectifier bus DC voltage. Besides, Voltage Dependent Current Order Limit (VDCOL) is used to limit the maximum allowable current in the link under low voltage conditions. Thus, I_{Href} along with the limits imposed by the VDCOL characteristics decides the current order ($I_{ord(r/i)}$) for the rectifier and inverter. Further, this current order decides the mode of operation of the link using a mode shift logic which in turn will determine the link current (I_d) (Kundur, 1994). For a mode, calculations are then carried out to obtain rectifier/inverter bus DC voltages (V_{dr} and V_{di}) and AC current injections (I_r and I_i). DQ transform is applied to the currents (I_{DQr} and I_{DQi}) in order to interface HVDC to a network. The complex current injections can be represented as :

$$\underline{\bar{I}}_{hvdc} = \begin{cases} \bar{I}_{DQr} & : \text{At the rectifier AC bus.} \\ \bar{I}_{DQi} & : \text{At the inverter AC bus.} \\ 0 & : \text{At other buses.} \end{cases}$$

The bus voltages of the network are calculated as :

$$\underline{\bar{V}} = (\underline{\bar{I}}_{Gs} - \underline{\bar{I}}_{Ls} - \underline{\bar{I}}_{hvdc})/Y_{BUS} \tag{2.4}$$

where, $\underline{\bar{V}}$ is the bus voltage vector, $\underline{\bar{I}}_{Gs}$ is the vector of generator source currents, $\underline{\bar{I}}_{Ls}$ is the load current vector and Y_{BUS} is the admittance matrix of the system.

Detailed modelling of the HVDC link with equations is discussed in (Teena and Shubhanga, 2017) and the same is taken up in this study.

2.2.3 Modelling of the TCSC

A simplified variable reactance model is adopted for the TCSC where the firing angle delays and controller dynamics are approximated by a first order delay circuit (Padiyar, 2009). With this model, constant current (CC) control scheme is implemented for the TCSC.

A TCSC connected in a line between i^{th} and j^{th} bus is shown in Figure 2.4 and the modelling steps are presented in Figure 2.5. The current controller is given in Figure 2.6. Here, I_{Tref}, $\bar{I}_N$, R_l, X_l, X_{TCSC} and T_{TCSC} refer to the reference current, line current, line resistance, line reactance, TCSC reactance and delay constant respectively. X_{max} and X_{min} respectively represent the maximum and minimum limits of the reactance of the controller. Current injection approach is used to interface TCSC to a network (Uday and Shubhanga, 2015).

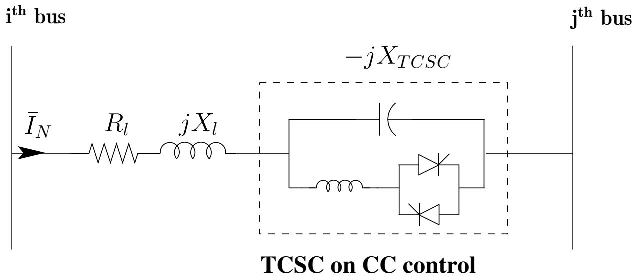

Figure 2.4: Schematic representation of a TCSC line

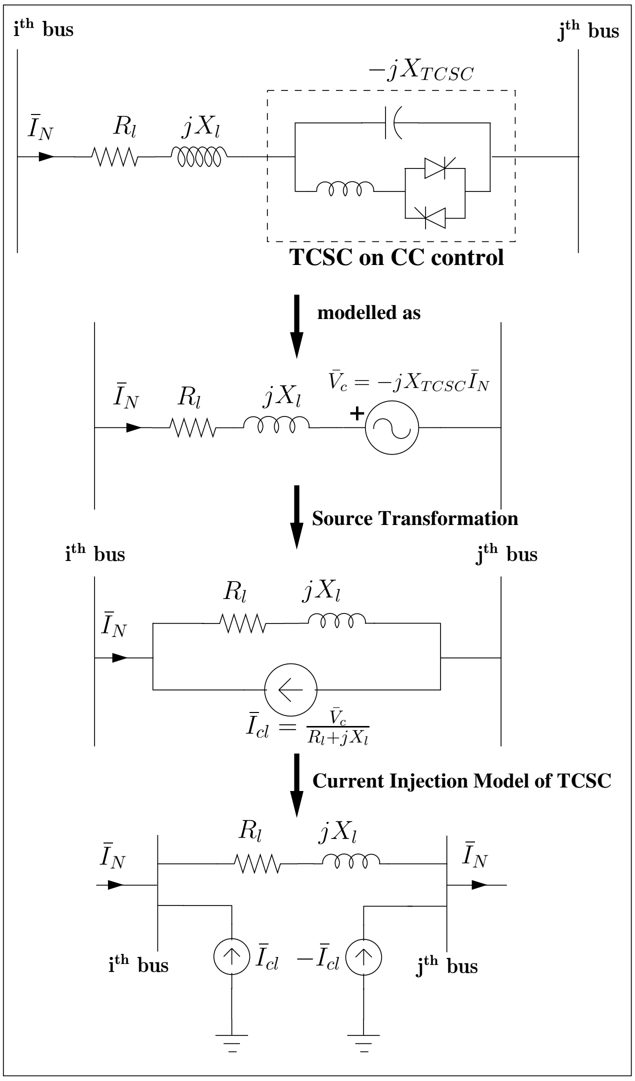

Figure 2.5: Schematic representation of the TCSC model

From Figure 2.5, the TCSC current injections can be given as :

$$\bar{I}_T = \begin{cases} \bar{I}_{cl} & : \text{At the } i^{th} \text{ bus.} \\ -\bar{I}_{cl} & : \text{At the } j^{th} \text{ bus.} \\ 0 & : \text{At other buses} \end{cases}$$

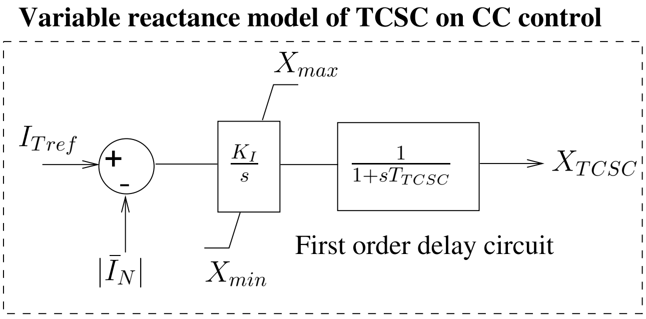

Figure 2.6: Current control scheme of the TCSC

Similar to HVDC modelling, the bus voltages of the network can be calculated as

$$\underline{\bar{V}} = (\underline{\bar{I}}_{Gs} - \underline{\bar{I}}_{Ls} - \underline{\bar{I}}_T)/Y_{BUS} \tag{2.5}$$

However, from Figure 2.5, it can be also noted that,

$$\bar{I}_{cl} = f(\bar{V}_i, \bar{V}_j, X_{TCSC}) \tag{2.6}$$

Therefore, from equations (2.5) and (2.6) it is understood that the model employed introduces non linear algebraic equations in addition to system differential algebraic equations i.e.

$$Y_{BUS}.\underline{\bar{V}} = h(\underline{\bar{V}}, X_{TCSC}) \tag{2.7}$$

An iterative solution within each time step is required to solve such a system of equations. In this study, this requirement is overcome by using a combination of fast acting differential equation and linear algebraic equation given by

$$\begin{aligned} \frac{d\bar{I}_{cl}}{dt} &= \frac{1}{T_L}(-\hat{\bar{I}}_{cl} + h(\underline{\bar{V}}, X_{TCSC})) \\ \bar{I}_{cl} &= \hat{\bar{I}}_{cl} \end{aligned} \tag{2.8}$$

A small value of time constant T_L is chosen.

The modelling of the other components of power system are done using (Padiyar K.R., 2002). Any requirement of iterative solution within a time step due to non linear algebraic equations is avoided in a similar way as that explained in modelling of TCSC.

2.2.4 Prony method

In this work, instead of performing a detailed analytical analysis, Prony method, a signal measurement-based mode identification method, is used to find the electromechanical oscillatory modes of the power system. Power system signals are generally classified as : a) Ring-down signals and b) Ambient signals. This study deals with only ring-down signals and hence prony method is adopted. A ring-down signal sampled at equal intervals of Δt to get N number of samples can be expressed in discrete form as :

$$y[k] = \sum_{i=1}^{n} B_i z_i^k \tag{2.9}$$

where, for the i^{th} component :

- z_i=$e^{(\lambda_i \Delta t)}$
- B_i = $\frac{A_i}{2} e^{j\phi_i}$ and λ_i= σ_i+$j\omega_i$
- A_i is the amplitude ϕ_i is the phase angle in *rad*
- σ_i is the decrement factor in $neper/s$ and ω_i is the radian frequency in rad/s

Sequence of steps to be followed for Prony analysis are (Gasca et al., 2012) :

- A linear prediction model $y(k)$ of order ‘n’ is constructed using the data set of the signal.

$$\begin{aligned} y(k) = a_1 y(k-1) + a_2 y(k-2) + a_3 y(k-3) + \ldots.. \\ \ldots\ldots + a_n y(k-n) \end{aligned} \tag{2.10}$$

  It is solved for its coefficients using Least square technique.

- Discrete system eigenvalues are determined using the characteristic polynomial $H(z)$ formed from the linear prediction coefficients.

$$H(z) = z^n - (a_1 z^{n-1} + a_2 z^{n-2} + \ldots.. + a_n z^0) = 0 \tag{2.11}$$

- Further, the continuous-time eigenvalues are found.

$$\lambda_i = \frac{ln(z_i)}{\Delta t} \tag{2.12}$$

- The original discrete form of the signal in equation (2.9) and the signal model can then be used to solve the amplitude and phase of the modes.
- From the complete set of modes, the most dominant modes are picked out on the basis of their energy (Krishna and Shubhanga, 2018).

2.2.5 System configuration

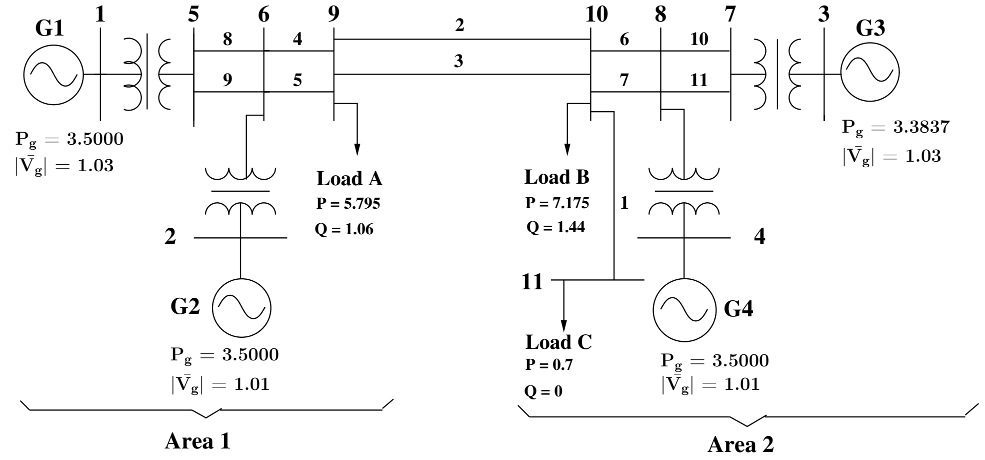

Figure 2.7: System description

A two-area, 4-machine, 10-bus power system as shown in Figure 2.7 is used for the study. One of the three lines interconnecting the two areas of the original system in (Padiyar K.R., 2002) is assumed to be on outage. An additional load, Load-C of $0.7 + j0$ pu is connected to bus-10 via a transmission line of $0.01j$. The system studies are carried out at 50% of the original load levels. The entire system is per-unitised on a 100 MVA base.

The generators are modelled as 2.2 models (Padiyar K.R., 2002). Generators 1 and 2 are provided with ST1A exciter and speed governor with hydro turbine. A slip input type power system stabilizer is also enabled in generator-2. Generators 3 and 4 are provided with constant static exciter. In addition, speed governor with reheat type steam turbine is enabled in generator-3. Composite load model is employed for real power loads with 30% fraction of constant power and constant current components along with 40% fraction of constant impedance component. The reactive power loads are modelled as constant impedance type. Loads are considered as frequency dependent. The network details are identical to those given in (Padiyar K.R., 2002).

In order to investigate the system performance, few case studies have been taken up. In the base case, both AC tie lines are noted to carry 0.5516 pu of power. The following systems are studied :

- Synchronous System :
    1. System with HVDC : The HVDC link shown in Figure 2.2 is used to replace line-2 of system shown in Figure 2.7. The LCC-HVDC link data is given in (Teena and Shubhanga, 2017).
    2. System with TCSC : Here, a TCSC with CC control as shown in Figure 2.4 is placed in line-2 of system shown in Figure 2.7. The TCSC current controller data is given in the Appendix A1.
    3. System with only TCSC line between the areas : Here, TCSC line is the only tie-line between the two areas. Line-3 is assumed to be on outage.
- Asynchronous System :
  In this system, HVDC link of Figure 2.2 is the only link between the two areas of the system in Figure 2.7.

2.3 Dynamic performance comparison of synchronous systems

In this section, simulations are carried out for the synchronous systems (system with HVDC and system with TCSC), and comparisons are drawn with the help of various case studies. In the base case, HVDC link / TCSC line is made to carry 0.5516 pu of power. The corresponding reference currents are shown in Table 2.1.

2.3.1 Variation in power level

The scheduled power transfer in the HVDC link / TCSC line is switched from the base case to a value of 0.8274 pu at 1s by changing the respective current reference values as tabulated in Table 2.1. The corresponding simulation results are shown in Figure 2.8 and Figure 2.9.

As observed in Figure 2.8, power transfer in the HVDC link / TCSC line tracks the reference level effectively. The power in the HVDC link settles to its new value without any oscillations unlike the power in the TCSC line. However, Line-3 power oscillates showing clearly the inter-area mode of frequency of 2.7656 rad/s.

The average system frequency (also known as common mode frequency or centre of inertia (COI) speed or **COI-frequency**) denoted by *sysCOI* for a system is given as:

$$sysCOI = \frac{\sum_{i=1}^{n} S_i H_i}{\sum_{i=1}^{n} H_i} \tag{2.13}$$

where n is total number of generators in the system, S_i is the slip deviation in pu and H_i is the inertia constant in MJ/MVA for the i^{th} generator.

COI-frequency is plotted for both the cases in Figure 2.9a. As speed governors and frequency dependency of loads are enabled, COI-frequency settles to a new steady-state value in both the cases. It is interesting to note that the COI-frequency of the system with HVDC shows an increasing trend whereas the system with TCSC shows a decreasing trend. In order to understand this, $\sum T_m - \sum T_{eg} = T_{COI}$ has been plotted in Figure 2.9b. Here, T_m refers to the mechanical torque and T_{eg} refers to the electromagnetic torque of the generators. It can be observed that the net T_{COI} is positive in the system with HVDC whereas it is negative in case of system with TCSC. This is noted to be due to decrease in the net real power losses in the system with HVDC and an increase in the losses in the system with TCSC with respect to base case.

Table 2.1: Current reference values in per-unit

Power Level	TCSC	HVDC	
	I_{Tref} (pu)	V_{dr} (pu)	I_{Href} (pu)
0.5516	0.5544	1.2016	0.4591
0.8274	0.8387	1.2023	0.6882

2.3.2 Load trip

The real power load, Load-C, is tripped at 1s during the base case operation of the system. The CC controller initiates action in order to retain the same level of power in HVDC link / TCSC line as seen in Figure 2.10. Hence, power in the other tie line gets altered to preserve the load balance as displayed in the plot. Since the load is thrown off, an increasing trend is observed in the COI - frequency plots of both the systems as shown in Figure 2.11.

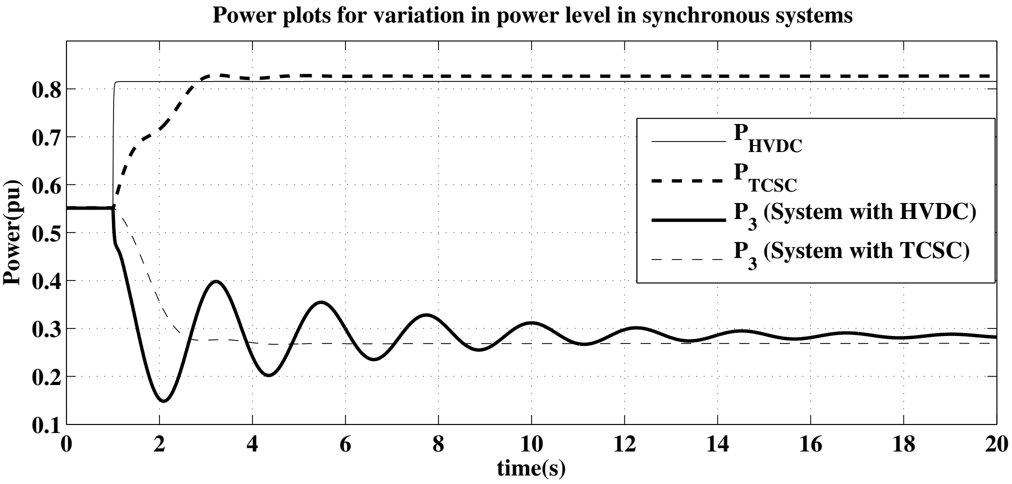

Figure 2.8: Power plots for variation in power level

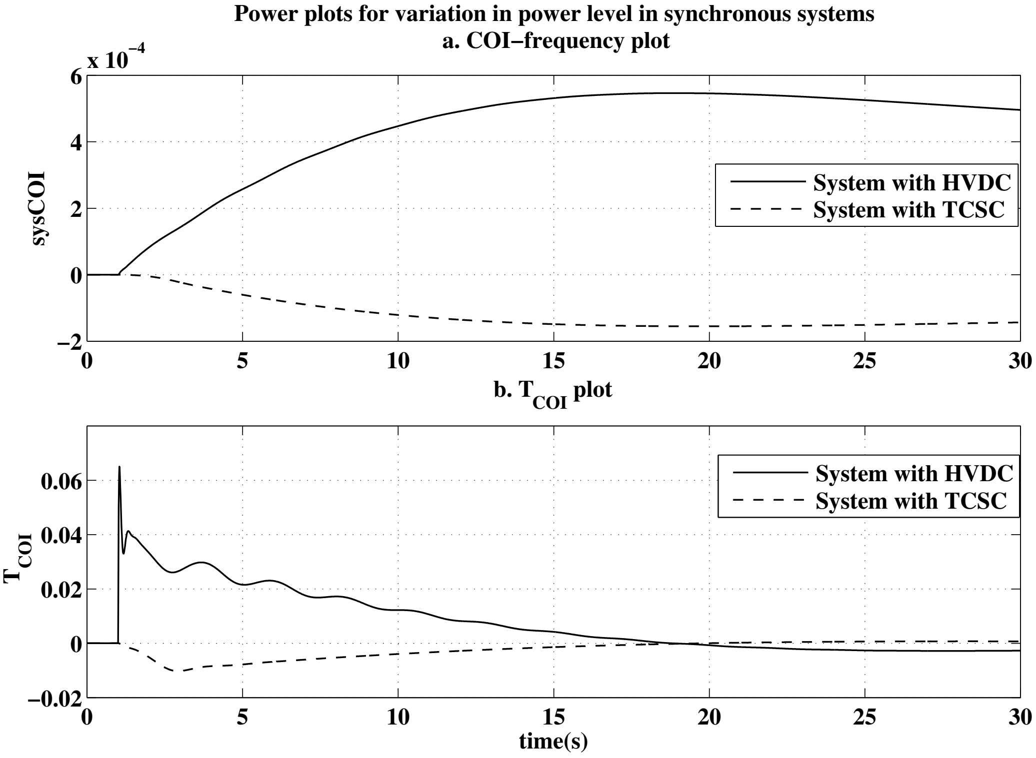

Figure 2.9: COI-frequency plots for variation in power level

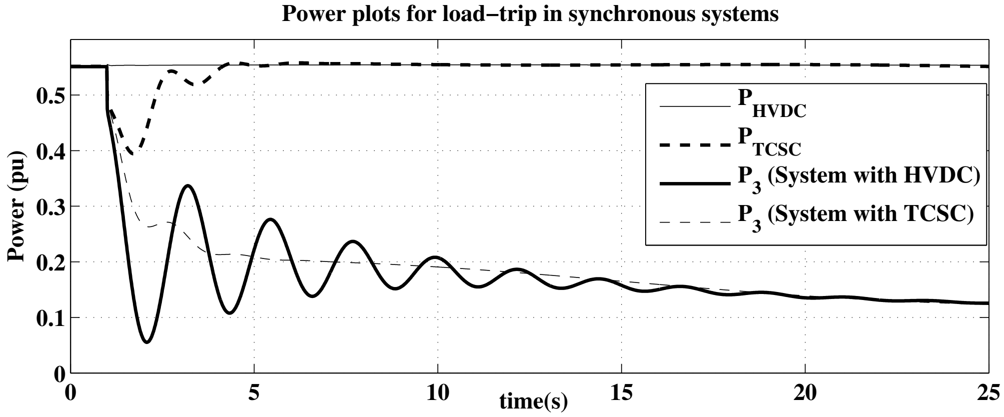

Figure 2.10: Power plots for load trip

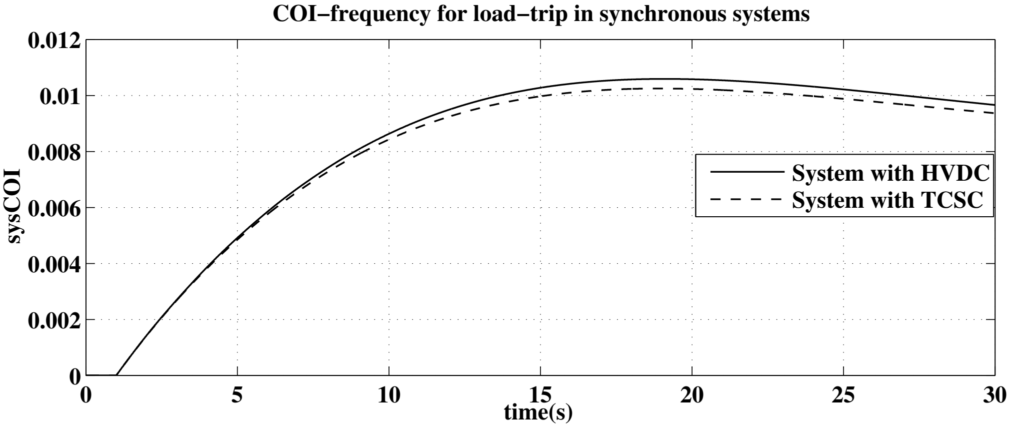

Figure 2.11: COI-frequency plots for load trip

2.3.3 AC tie line trip

In this section, AC tie line-3 (refer Figure 2.7) is tripped at 1s when the system is operating in the base case. In this condition, as displayed in Figure 2.12, irrespective of the load requirement in area-2, the HVDC link still transfers the same scheduled power. Further, as shown in Figure 2.13, the individual COI-frequency plots of area-1 and area-2 diverge, indicating loss of synchronism between the two areas.

However, in case of system with TCSC, the real power in the TCSC line increases to match the load-generation balance of the combined system (see Figure 2.12), thus maintaining the synchronism between the two areas. This is further verified by the COI-frequencies of area-1 and area-2 reaching the COI-frequency plot of the entire system in Figure 2.14. The plot of current in the TCSC line is presented in Figure 2.15. It can be observed that the current in the TCSC line is larger than the reference current of the controller throughout, after the disturbance. From the schematic of the controller in Figure 2.5, it can be understood that the controller would hit its lower limit. This indicates that the TCSC is unable to provide any regulation when the two areas get connected only by a single TCSC line.

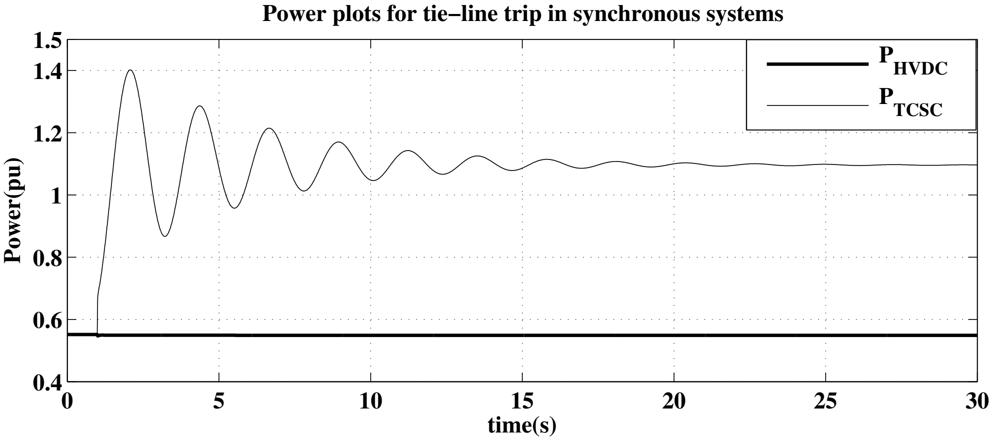

Figure 2.12: Power plots for AC tie line trip

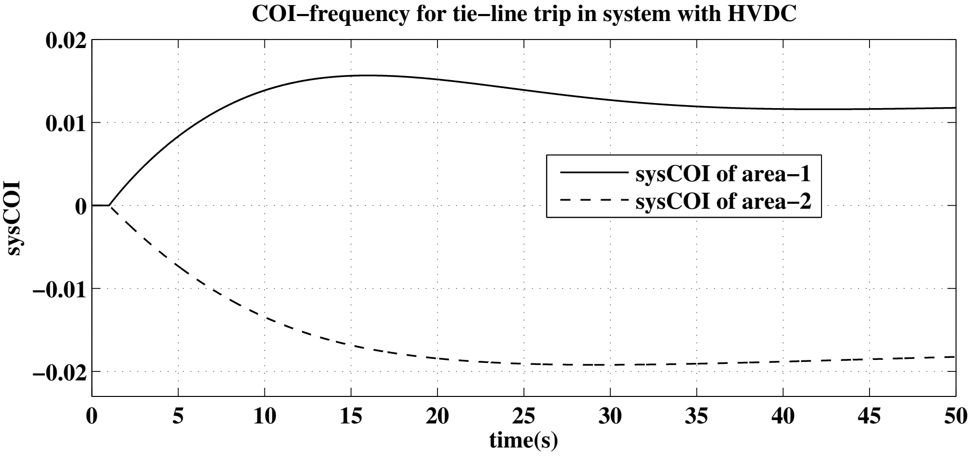

Figure 2.13: COI-frequency plots of HVDC system for AC tie line trip

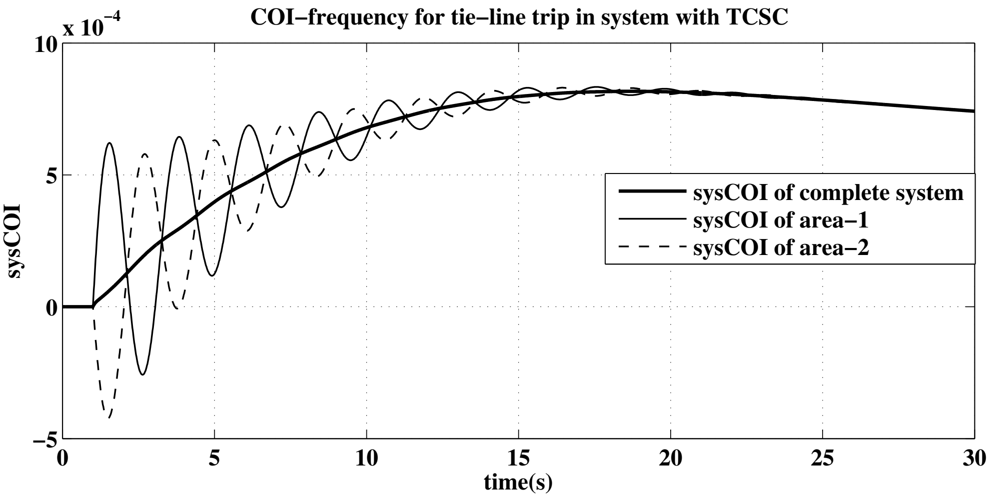

Figure 2.14: COI-frequency plots of TCSC system for AC tie line trip

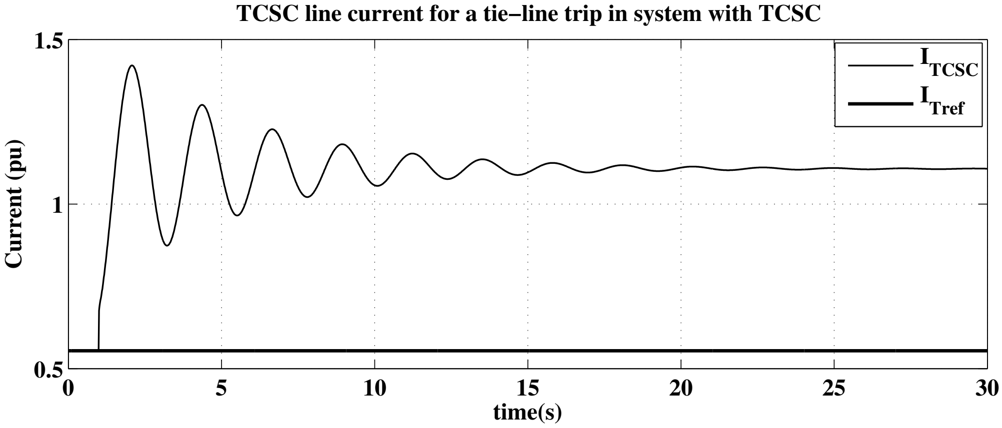

Figure 2.15: Current in the TCSC line for AC tie line trip

2.4 Modal behaviour of synchronous systems

In this section, modal behaviour of the synchronous systems are evaluated. In our analysis, the slip-COI signal of generators, given as slip-COI = $S_i - sysCOI$ for i^{th} generator, is obtained by applying a 3 phase fault for a short duration of 0.05 s without any line trip. This signal is subjected to prony analysis for identification of modes of the system.

In the synchronous system with HVDC / TCSC, the Prony analysis is repeated for different cases of pre-fault power levels in HVDC link / TCSC line ($\mathrm{P_{HVDC}}$ / $\mathrm{P_{TCSC}}$). The swing mode frequencies and their damping factors are tabulated in Table 2.2 for each of the cases. The analysis is also included for the system shown in Figure 2.7 for comparison (referred as System without HVDC/TCSC). It is to be noted that, case-3, i.e. a power transfer of 1.1010 pu could be established only in the system with HVDC. In this case, power in the AC tie line-3 (P_3) is zero. Such a condition is found to be infeasible in the system with TCSC.

Table 2.2: Comparison of results obtained from prony analysis of slip w.r.t COI signals for various power levels in synchronous systems

	Pre-fault Power Level		System without HVDC / TCSC**		System with TCSC**		System with HVDC**	
Case	P_2 / P_{TCSC} / P_{HVDC}	P_3	Swing Modes	Damping Factor	Swing Modes	Damping Factor	Swing Modes	Damping Factor
1	0.5516	0.5516	$\mathbf{-0.3863 \pm j\,3.3867}$ $\boxed{-1.5576 \pm j\,4.9857}$ $\mathit{-2.7765 \pm j\,6.2008}$	$\mathbf{0.1133}$ $\boxed{0.2982}$ $\mathit{0.4087}$	$\mathbf{-0.5611 \pm j\,3.3013}$ $\boxed{-1.6212 \pm j\,5.1956}$ $\mathit{-2.4817 \pm j\,6.4345}$	$\mathbf{0.1676}$ $\boxed{0.2979}$ $\mathit{0.3598}$	$\mathbf{-0.2077 \pm j\,2.7638}$ $\boxed{-1.6278 \pm j\,4.9459}$ $\mathit{-2.5731 \pm j\,6.0941}$	$\mathbf{0.0749}$ $\boxed{0.3126}$ $\mathit{0.3889}$
2	0.8274	0.2762	$\mathbf{-0.6304 \pm j\,3.8467}$ $\boxed{-2.0013 \pm j\,4.9885}$ $\mathit{-2.8400 \pm j\,6.2400}$	$\mathbf{0.1617}$ $\boxed{0.3724}$ $\mathit{0.4142}$	$\mathbf{-0.8307 \pm j\,3.7637}$ $\boxed{-1.8348 \pm j\,5.4656}$ $-2.7791 \pm j\,5.6353$	$\mathbf{0.2155}$ $\boxed{0.3182}$ $\mathit{0.4421}$	$\mathbf{-0.2063 \pm j\,2.7656}$ $\boxed{-1.6193 \pm j\,4.9546}$ $\mathit{-2.5058 \pm j\,6.0820}$	$\mathbf{0.0743}$ $\boxed{0.3107}$ $\mathit{0.3809}$
3	1.1010	0					$\mathbf{-0.2018 \pm j\,2.7637}$ $\boxed{-1.6034 + j\,4.9742}$ $\mathit{-2.4386 \pm j\,6.0741}$	$\mathbf{0.0728}$ $\boxed{0.3068}$ $\mathit{0.3725}$

****bolded mode** - Inter-area mode, $\boxed{\text{boxed mode}}$ - local mode of area-2, *italicized mode* - local mode of area-1

In order to verify the nature of swing modes, slip-COI plots for case-1 of system with HVDC are presented in Figure 2.16a for a 3-phase fault at bus-7. It can be observed that, generator G3 oscillates against G4 with a radian frequency almost same as the frequency of the boxed mode (4.9459 rad/s) tabulated in Table 2.2. Since the generators belonging to area-2 participate in this oscillation, this mode is considered as a local mode of area-2. Once the local-mode dies down, it can be seen that G1, G2 together oscillate against G3, G4 with a radian frequency equal to the frequency of the mode (2.7638 rad/s) which is in bold. This mode is referred to as an inter-area mode. The third mode in the list (italicized mode) is captured when a 3-phase fault is applied at bus-5 (plot not given), with generator G1 oscillating against G2. This mode is the local mode of area-1. Similarly, slip-COI plots for case-1 of system with TCSC have been plotted in Figure 2.16b for a 3-phase fault at bus-7. The corresponding modes can be verified through Table 2.2.

The following observations can be made from Table 2.2 :

- For a given case, the inter-area mode of the system with HVDC has the lowest damping factor and that of the system with TCSC has the highest. The frequency of the inter-area mode is the lowest in the system with HVDC, and the system without HVDC/TCSC has the highest inter-area mode frequency. To graphically verify these

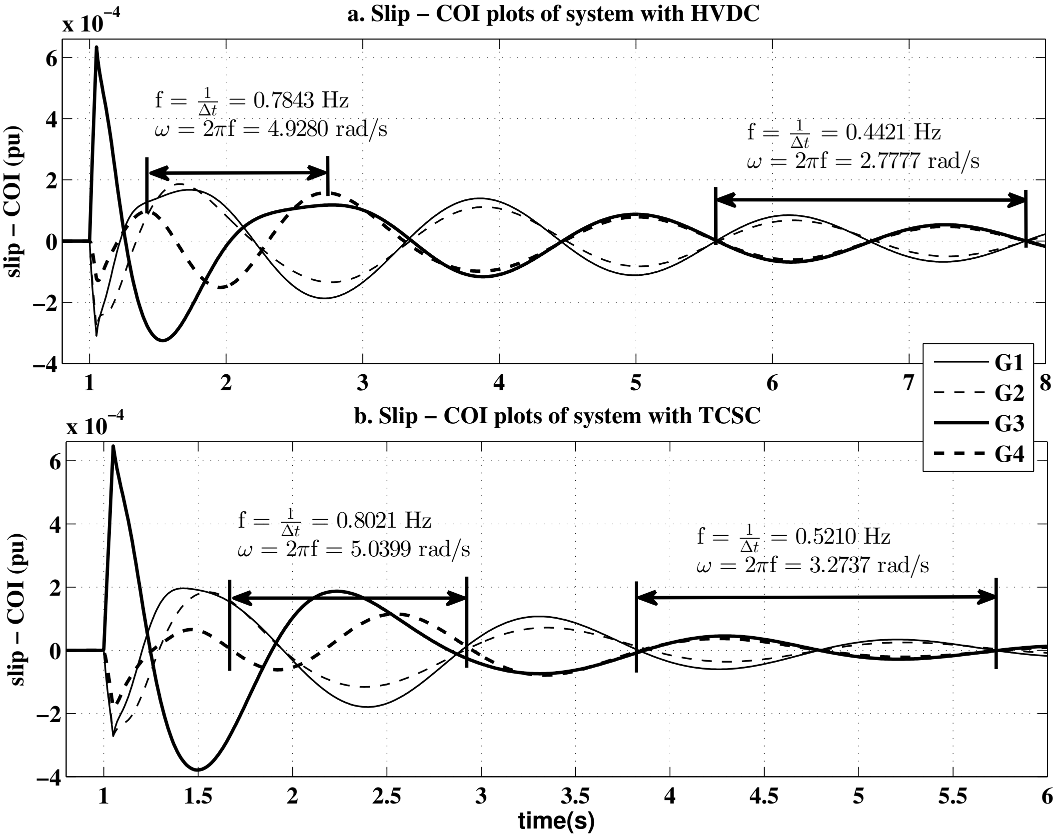

Figure 2.16: Slip w.r.t COI plots of system with HVDC and system with TCSC

facts, plots of the bus angle across the tie lines for all systems have been shown in Figure 2.17 for case-1. Only the inter-area oscillations are seen in such a plot. It can be observed that the oscillations decay faster in the system with TCSC. Also, the differences in frequency can be clearly seen through the plot.

- In the system without HVDC/TCSC, the damping factor and frequency of the swing modes increases as we increase the power flow in line-2.

- In system with TCSC, the damping factor of the swing modes increases as we increase the power flow in the TCSC line. Further, the frequency of the inter-area mode and local mode of area-2 increases, and that of the local mode of area-1 decreases.

- In the system with HVDC, the frequency of the inter-area mode remains almost the same with an increase in the specified power level in the link. Also, the damping factor of the inter-area mode doesnot show much variation. This can be verified by comparing the plots for case-1 and case-3 in Figure 2.17. However, the attributes of the local modes show variation along the cases. It is due to the fact that the scheduled power in the HVDC link is increased from case-1 to case-3. This leads to a decrease in the power flow in the AC tie line. Hence, it is expected that the local mode gets influenced to a greater extent than the the inter-area mode along the cases.

- In the system with HVDC, the damping factors of both the local modes show a decreasing trend. An increase in the local mode frequency of area-2 can be noticed, whereas the frequency of the local mode of area-1 exhibits a decreasing trend.

- It is to be noted that, in case-3, the HVDC link alone transfers power from area-1 to area-2 even though there is an AC line interconnection (P_3=0). This AC interconnection preserves the inter-area mode in the system.

2.5 Dynamic analysis of asynchronous system

In this section, the asynchronous system with HVDC is analysed. In this system, as the areas are connected only through a DC link, they would work as two independent AC systems. Thus, the system would have two different COI-frequencies, each pertaining to a area.

According to the load flow algorithm discussed in Section 2.2.1 buses 1 and 3 are chosen as slack buses. The voltages at these buses are initialised as $\bar{V}_1 = 1.03\angle 0$ and $\bar{V}_3 = 1.03\angle 0$. From the load flow, the power transfer in the HVDC link is found to be 1.1010 pu. The reference current of this system is found to be 0.9171 pu.

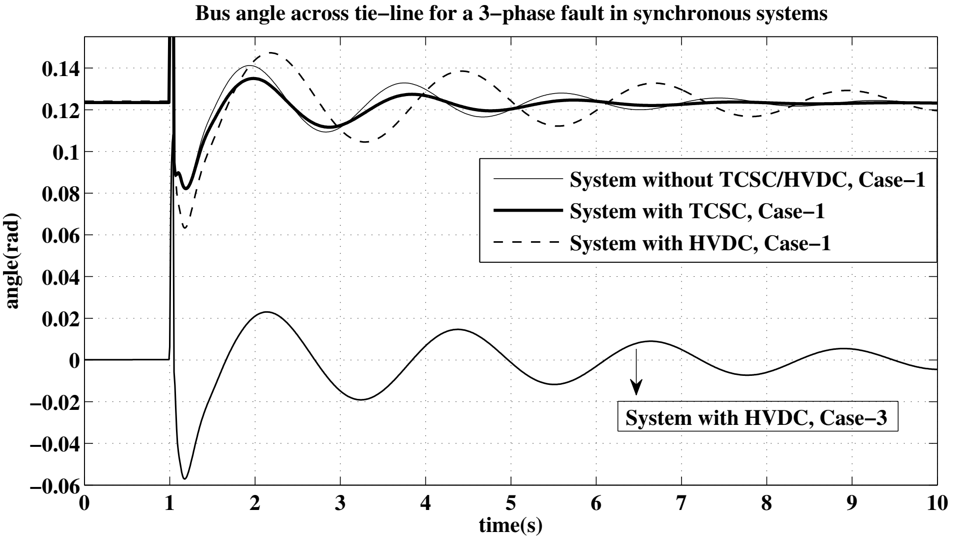

Figure 2.17: Bus angle across tie lines

2.5.1 Load trip

The real power load-C in area-2 is tripped at 1s. The power in the HVDC line remains almost the same as shown in Figure 2.18 due to the controller action. A slight increase in power is due to an increase in rectifier bus AC voltage.

The COI-frequency plots of area-1 and area-2 are given in Figure 2.19. It can be seen that, the COI-frequency of area-2 settles to a new higher value. However, the COI-frequency of area-1, shows a negligible change. Thus, the two areas now operate at different frequencies indicating asynchronous operation. Also, the rotor angles of all the generators expressed with respect to their COI's (δ w.r.t COI) are plotted in Figure 2.20. It can be clearly seen that, in the asynchronous HVDC system, with a load-trip in area-2, the quantities of area-1 do not get appreciably affected.

But, a contrasting result is obtained, when a 3-phase fault of small duration is applied in area-2 in this system. The results are presented in the following subsection.

2.5.2 3-phase fault

A 3-phase fault is applied at bus-7 of the asynchronous HVDC system at 1s and cleared after 0.05 s. The COI-frequencies of both the areas vary as shown in Figure 2.21. Though the fault belongs to area-2, unlike in the previous case of load trip, electromechanical oscil-

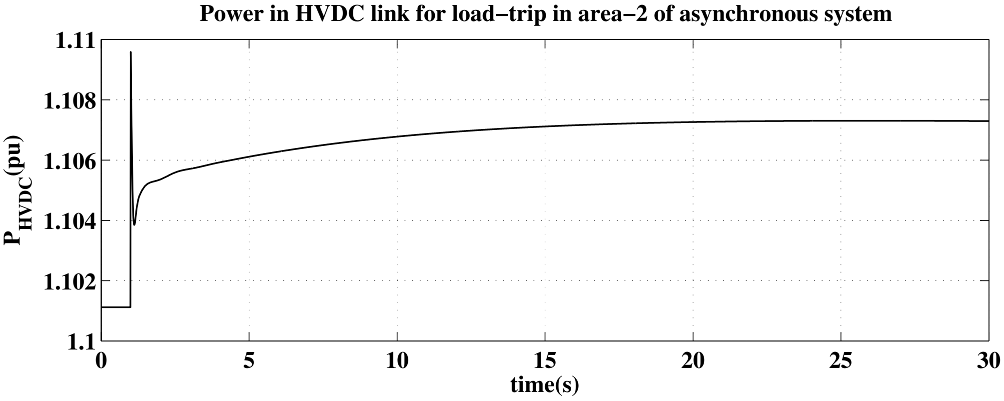

Figure 2.18: Power plot for load trip in the asynchronous HVDC system

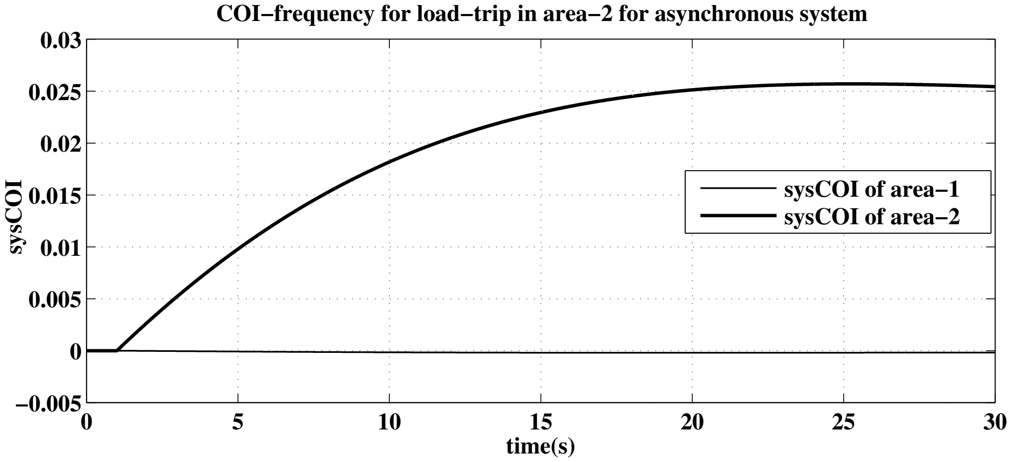

Figure 2.19: COI-frequency plots for load trip in the asynchronous HVDC system

lations appear in area-1 as well. The δ w.r.t COI plots of generators shown in Figure 2.22 further confirm this behaviour.

2.6 Modal analysis of asynchronous system

The prony analysis is now performed for the asynchronous HVDC system, where a real power transfer of 1.1010 pu is maintained from area-1 to area-2. The swing modes and their damping factors are presented in Table.2.3. The modes are verified by obtaining the slip-COI plots of generators in two areas by applying a 3-phase fault at bus-7 (see

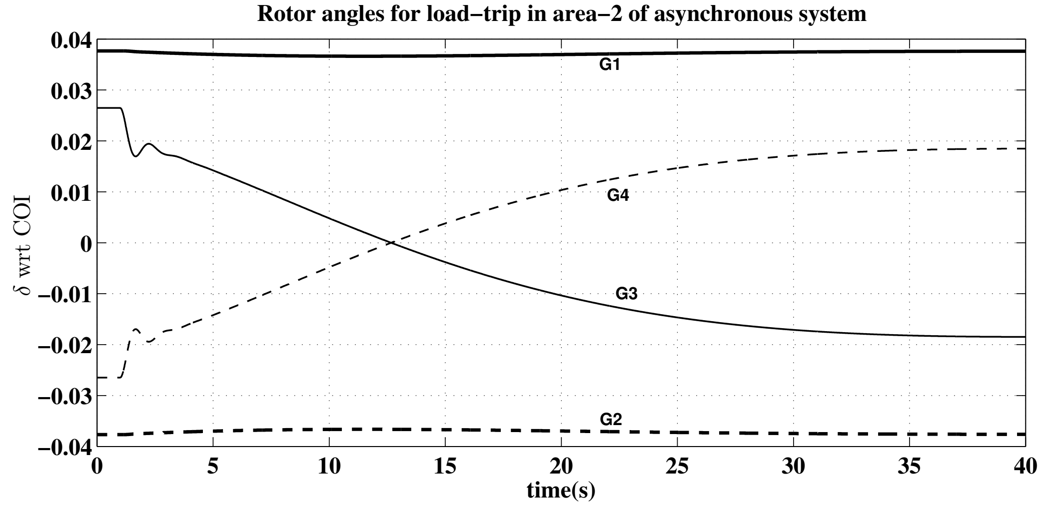

Figure 2.20: Rotor angle w.r.t COI plots for load trip in the asynchronous HVDC system

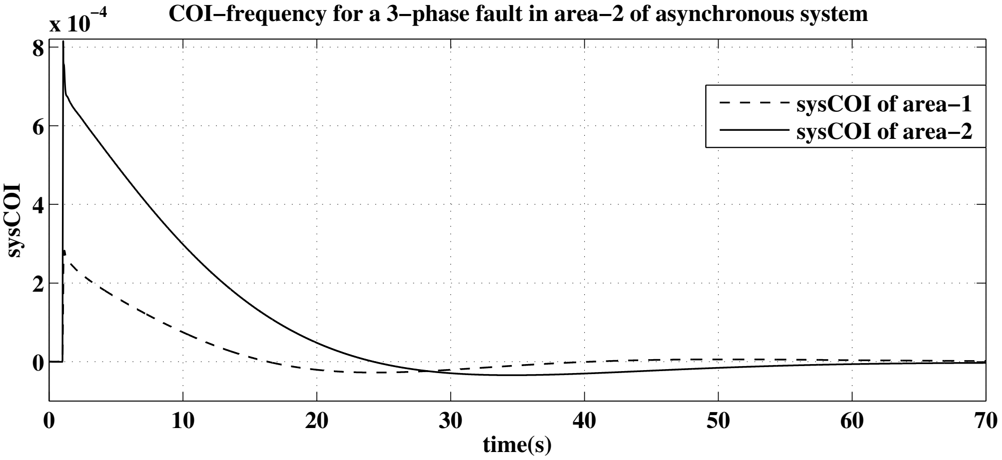

Figure 2.21: COI-frequency plots of area-1 and area-2 for a 3-phase fault at bus-7 in the asynchronous HVDC system

Figure 2.23). It can be observed that generators in area-1 swing against each other with a radian frequency equal to 6.0432 rad/s in Figure 2.23a. This is the local mode of area-1. Similarly, generators in area-2, oscillate against each other as shown in Figure 2.23b with a radian frequency of 5.0745 rad/s (see Table 2.3). This mode, therefore, corresponds to the local mode of area-2. As there is no AC link between the two areas, no inter-area modal behaviour exists in the asynchronous HVDC system.

For comparison, the swing modes of the system with only AC line-3 (without TCSC /

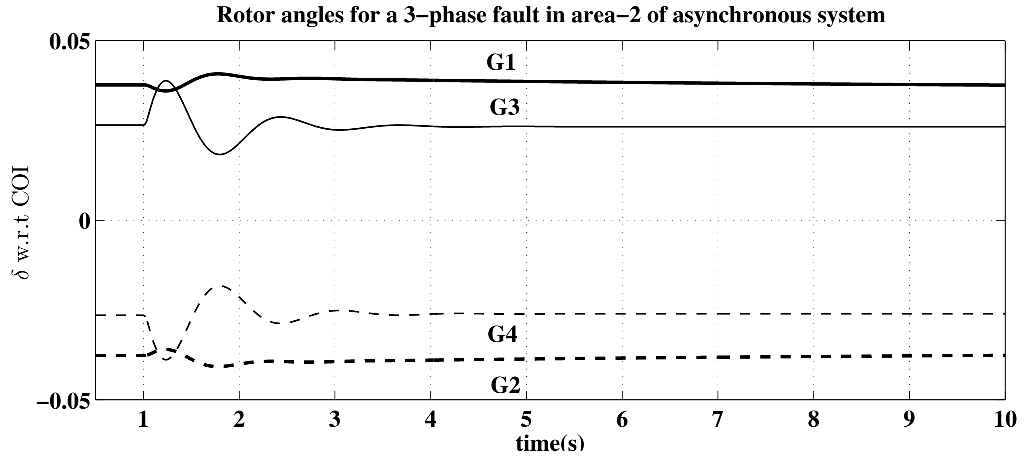

Figure 2.22: Rotor angle w.r.t COI for a 3-phase fault at bus-7 in the Asynchronous HVDC system

Table 2.3: Comparison of modes for a asynchronous HVDC system and system having one AC Tie line with and without TCSC

Asynchronous HVDC system**		System with only AC line-3** between the areas		System with only TCSC line** between the areas	
Swing Modes	Damping Factor	Swing Modes	Damping Factor	Swing Modes	Damping Factor
-2.2280 ±j 6.0432	*0.3459*	*-2.5697 ±j 6.1395*	*0.3861*	*-2.6467 ±j 6.3229*	*0.3861*
$\boxed{-1.6018 \pm j\,5.0745}$	$\boxed{0.3010}$	$\boxed{-1.5812 \pm j\,4.9846}$	$\boxed{0.3024}$	$\boxed{-1.5837 \pm j\,5.0749}$	$\boxed{0.2979}$
		-0.1970 ±j 2.7420	**0.0717**	**-1.1889 ±j 2.4666**	**0.4342**

***italicized mode* - local mode of area-1, $\boxed{\text{boxed mode}}$ - local mode of area-2, **bolded mode** - Inter-area mode

HVDC) between the areas, are also added in the table. It can be seen that the local mode of area-1 of the asynchronous HVDC system has a lower radian frequency and damping factor when compared to the system with only line-3 as the tie-line but the local mode of area-2 has a higher radian frequency and lower damping factor for the asynchronous HVDC system.

In Table. 2.3, the swing modes are also obtained for the system with only TCSC line between the areas. It is observed that the attributes of local mode of area-2 of asynchronous system is similar to that of this system. However, the frequency and damping factor of local mode of area-1 of asynchronous system is smaller. A large increase in the damping factor of the inter-area mode is observed in system with only TCSC tie-line when compared to the system with only AC line-3 between the areas. In the system of Fig. 2.7, when TCSC line is the only link between the two areas, a 3-phase fault is applied at bus-7 at 1s and cleared in 0.05s. The current in the TCSC line displayed in Fig. 2.24a indicates that the

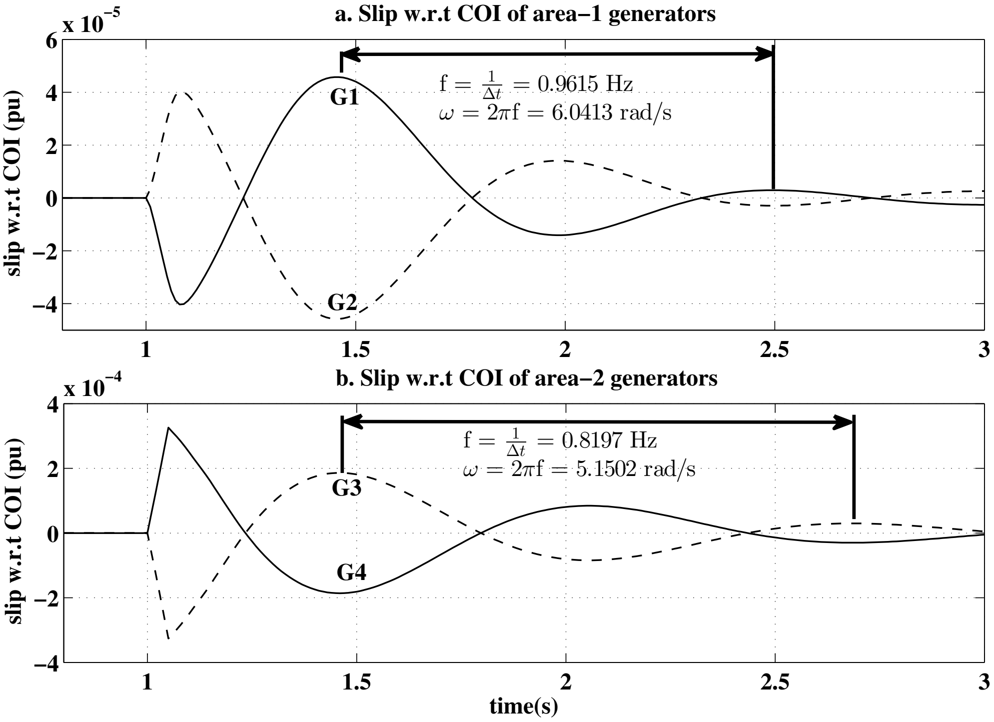

Figure 2.23: Slip w.r.t COI plots of generators in area-1 and area-2 for a 3-phase fault at bus-7 in the Asynchronous HVDC system

controller would hit its upper limit as shown in Fig. 2.24b. The slip w.r.t COI plots of all the generators under such condition are given in Figure 2.25. Though the oscillations damp out quickly, from Figure 2.24 it is seen that the operating point continuously changes and eventually reaches a new steady state. Under such a condition, a normal analytical based eigenvalue estimation fails. As Prony analysis is used, the modes could be readily identified even under a changing operating condition.

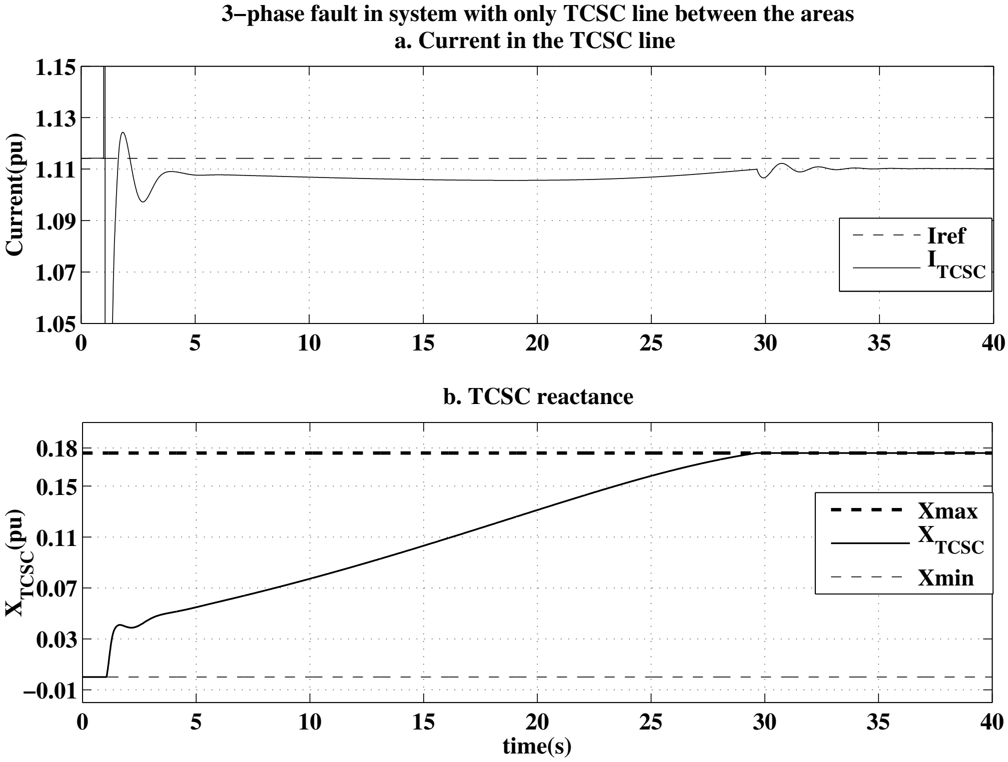

Figure 2.24: Current in TCSC line for a 3-phase fault at bus-7 when the two areas are connected only via TCSC line

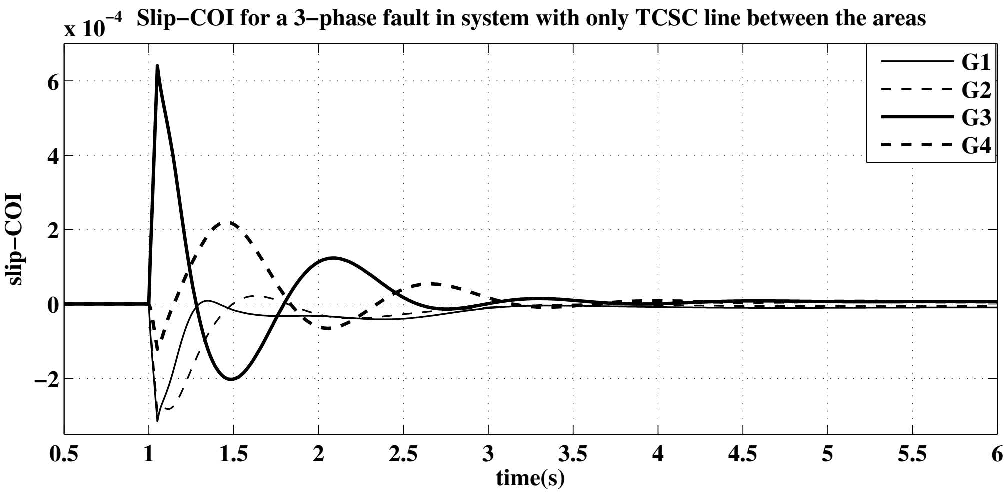

Figure 2.25: Slip w.r.t COI plot for a 3-phase fault at bus-7 when only TCSC line is connected between two area

2.7 Summary

This chapter analyses the dynamic and modal behaviour of synchronous systems with LCC-HVDC link / TCSC line and an asynchronous system with LCC-HVDC. A 4-machine, two-area system is used for the study. Studies carried out and observations made in this chapter are given below:

- The dynamic behavioural differences of the systems subjected to tie line trip and variation in power level are discussed using power plots and centre of inertia plots.
- From modal analysis of the synchronous systems, it is observed that for a given power level, the system with HVDC has the lowest inter-area mode frequency and damping factor when compared to systems with and without TCSC.
- The impact of power level changes on the attributes of the swing modes of the systems is neatly depicted. The attributes of inter-area mode of the system with HVDC remain unaffected by the variation of power levels. However, the impact is observed in the characteristics of all the dominant modes of the system with TCSC.
- The effect of forming an asynchronous link is studied by analysing the modes of the asynchronous system with LCC-HVDC in comparison to the modes of a system with

only one AC tie line between the areas, and a system with only a TCSC line between the areas.

- The eigenvalue analysis is conducted using prony method which doesnot require rigorous calculations as in conventional analytical methods.

The LCC-HVDC technology stands as a well-established and mature system that has continuously evolved over the years. This chapter provided insight into this technology from a power system standpoint delving into its modal and dynamic analysis within multi-machine systems. Another category of converter-based HVDC technology is VSC-HVDC systems. In contrast to LCC-HVDC systems, VSC-HVDC can autonomously control both active and reactive power without requiring extra compensating equipment. It possesses self-commutation capability, making it resilient to commutation failures, as well as black start capability and the ability to produce fewer harmonics. The next chapter explores VSC-HVDC systems, focusing on their modelling and control mechanisms.

Chapter 3

MODELLING AND CONTROL OF VSC-HVDC SYSTEMS

3.1 Introduction

Voltage Source Converter based High Voltage Direct Current systems emerged as a response to the need for more efficient and controllable power transmission. Advances in semiconductor technology and power electronics paved the way for VSC's, leading to the development of the VSC-HVDC system. The provision of independent control of active and reactive power, instantaneous power reversal without the need to reverse DC voltage, black start capability etc makes the VSC converter superior to its conventional counterpart. The major applications of the system include interconnection of asynchronous systems, integration of offshore wind farms to the main grid, provision of frequency support etc. Advanced research on VSC-HVDC systems and its control strategies is continuously progressing.

In this chapter, the modelling and control of VSC-HVDC system integrated to multi-machine systems is discussed in detail. The effect of outer active and reactive power control loops on the performance of supplementary frequency controllers is examined. The closed loop models of the feedforward and feedback active power loops are derived through analytical analysis and evaluated through simulation results. Bandwidth analysis is used to study the impact of feedback active power loops. In addition, the effects of feedforward reactive power control, feedback reactive power control and AC voltage control are also investigated. Further, a simplified VSC-HVDC model is described that can be applied to links embedded in large power systems where the performance analysis of the AC systems is the main objective of the study. It is validated in two multi-machine test systems where the modal and dynamic analysis of the system with simplified model is compared with that of a full model.

3.2 Description of VSC-HVDC link

The one line diagram of a point to point VSC-HVDC link connected between two AC buses is given in Figure 3.1. VSC-HVDC converters are connected to the AC system through a phase reactor and transformer. The subscripts "*r*" and "*i*" in the figure represent rectifier side and inverter side quantities and parameters respectively. $\mathrm{PCC_r}$ and $\mathrm{PCC_i}$ are the AC power system buses to which the link is connected and will be referred as PCC buses from here on. The converter side AC buses are represented as Bus-r and Bus-i and will be referred as converter buses from here on. The phase reactor and transformer are depicted by impedances, $Z_r = R_r + jX_r$ and $Z_i = R_i + jX_i$. C_{dc} is the capacitance of the DC capacitor, L_{dc} is the inductance of DC link, R_{dc} is the resistance of the DC link, v_{dcr} and v_{dci} are the DC voltages at rectifier and inverter respectively, i_{dc1}, i_{dc2}, and i_{cc} are DC currents. In this study, the complete interfacing of all the components in the power system to the AC network is conducted in the synchronously rotating reference frame or *DQ* frame. Any quantity in the *DQ* frame is defined as $\overline{F}_{DQ} = f_Q + jf_D$. The voltage at the PCC buses are represented by E or e and that of converter buses are V or v with appropriate subscripts. For *eg.*, the rectifier side PCC bus voltage (refer Figure 3.1) in DQ frame is represented as $\overline{E_{DQ}}_r = e_{Q_r} + je_{Dr}$. All the quantities are per unitised for the modelling.

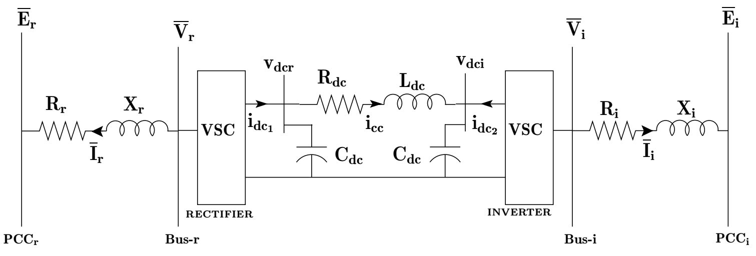

Figure 3.1: Equivalent circuit of VSC-HVDC link

The subscripts *r* and *i* can be used as required and will be omitted in redundant cases.

3.3 Dynamic model

In this section, the complete dynamic modelling of a 2-terminal VSC-HVDC link is presented. It involves the modelling of the converters, control system and the DC link. Current injection approach is used to interface the link to the AC network. A general schematic of a VSC station derived from Figure 3.1 is given in Figure 3.2.

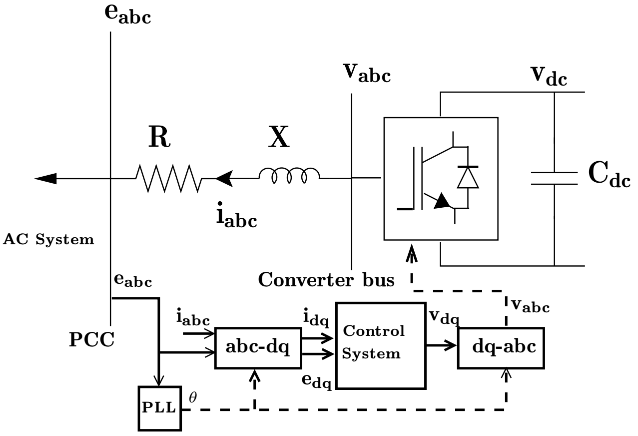

Figure 3.2: General schematic of a VSC station

A cascaded control structure consisting of inner and outer controllers is used to control each of the converters. Decoupled vector current control strategy is used. The fast inner current controller decouples the components of current using feedforward method which is elaborated later in this section. The reference currents required for the inner controller are provided by the outer controllers. The outer controller controls the real and reactive power at the PCC of each converter.

Given the voltage at PCC, say, $e_Q + je_D$ and injected current as $i_Q + ji_D$, it is well known that the injected real power at the PCC is given as $P_{PCC} = e_Q i_Q + e_D i_D$ and the injected reactive power as $Q_{PCC} = e_D i_Q - e_Q i_D$. It can be seen that each of the power quantities depend on both the components of current. An alteration in the frame of the vector co-ordinates can lead to decoupling of the components that would benefit the outer control process (Schauder and Mehta, 1993).

3.3.1 dq transformation

In regard to above, as a first step to modelling, a new frame called as dq frame is defined where the instantaneous voltage at the PCC is always aligned to the q axis and the d axis is quadrature to it. Any quantity in the dq frame is defined as $\overline{F}_{dq} = f_q + jf_d$. The transformation of any quantity from DQ frame to dq frame is given below :

$$\begin{aligned} f_q + jf_d &= (f_Q + jf_D)e^{-j\theta} \\ &= (f_Q + jf_D)(\cos\theta - j\sin\theta) \end{aligned} \tag{3.1}$$

where 'θ' is the PCC bus angle. The angle can be obtained from a PLL and this can be written in matrix form as :

$$\begin{bmatrix} f_q \\ f_d \end{bmatrix} = \begin{bmatrix} \cos\theta & \sin\theta \\ -\sin\theta & \cos\theta \end{bmatrix} \begin{bmatrix} f_Q \\ f_D \end{bmatrix} \tag{3.2}$$

Consider the voltages at $\mathrm{PCC_r}$ and $\mathrm{PCC_i}$,

$$\begin{aligned} \overline{E}_{DQ_r} &= e_{Q_r} + je_{D_r} = \left(\sqrt{e_{Q_r}^2 + e_{D_r}^2}\right)\angle\theta_r \\ \overline{E}_{DQ_i} &= e_{Q_i} + je_{D_i} = \left(\sqrt{e_{Q_i}^2 + e_{D_i}^2}\right)\angle\theta_i \end{aligned} \tag{3.3}$$

where 'θ_r' and 'θ_i' are the bus angles.
Transforming it to the dq frame using equation (3.1),

$$\begin{aligned} e_{q_r} &= \sqrt{e_{Q_r}^2 + e_{Dr}^2} \ , \quad e_{d_r} = 0 \\ e_{q_i} &= \sqrt{e_{Q_i}^2 + e_{Di}^2} \ , \quad e_{d_i} = 0 \end{aligned} \tag{3.4}$$

Therefore, the real power and reactive powers injected at the PCC (P_{PCC} and Q_{PCC}) by the converters can now be written as,

$$\begin{aligned} P_{PCCr} &= e_{q_r} i_{q_r} \ , \quad Q_{PCCr} = -e_{q_r} i_{d_r} \\ P_{PCCi} &= e_{q_i} i_{q_i} \ , \quad Q_{PCCi} = -e_{q_i} i_{d_i} \end{aligned} \tag{3.5}$$

It can be seen that, only 'q' component of current controls the active power and only 'd' component of current controls reactive power thus facilitating the control process. Hence, the modelling of the converters and its control system is done in the dq frame of reference.

3.3.2 Converter model

A generalised converter model is presented here with current directions taken to be into the PCC bus.
The basic equation of the converter AC side in *abc* reference frame is (refer Figure 3.2) :

$$\frac{X}{\omega_{gB}}\frac{di_{abc}}{dt} = v_{abc} - e_{abc} - Ri_{abc} \tag{3.6}$$

The converter model in dq frame is given as (Shubhanga, 2018):

$$\frac{di_q}{dt} = \frac{\omega_{gB}}{X}[v_q - Ri_q + \frac{\omega}{\omega_{gB}}Xi_d - e_q] \tag{3.7}$$

$$\frac{di_d}{dt} = \frac{\omega_{gB}}{X}[v_d - Ri_d - \frac{\omega}{\omega_{gB}}Xi_q - e_d] \tag{3.8}$$

Above, $\omega = \omega_{gB}$ and $e_d = 0$ as discussed in section 3.3.1. The initial conditions of the above equations are obtained from AC loadflow. The quantities v_q and v_d are obtained from output of control system block.

3.3.3 Control system modelling

The control of VSC converters comprises essentially of control of real and reactive power that the VSC-HVDC exchanges with the AC system. The control of real power may be implemented to regulate the power flow or to control the DC voltage of the VSC. Reactive power control may be done directly or by controlling the AC voltage magnitude at the PCC. Along with the power control, the controller should also provide converter protection, good response, system stability and grid support whenever required. Hence, a cascaded control structure is adopted with inner controller which takes care of converter protection and the outer controller handles VSC performance requirements. A block diagram of complete control of a VSC converter is displayed in Figure 3.3.

3.3.3.1 Outer controller

For real power control of a two terminal VSC-HVDC link, one terminal controls the active power at the PCC bus and the other terminal controls the DC voltage. Either reactive power or AC voltage magnitude at the PCC bus is controlled at each terminal. The outer controller gives the required reference currents to the inner controller. The *q* axis currents completely

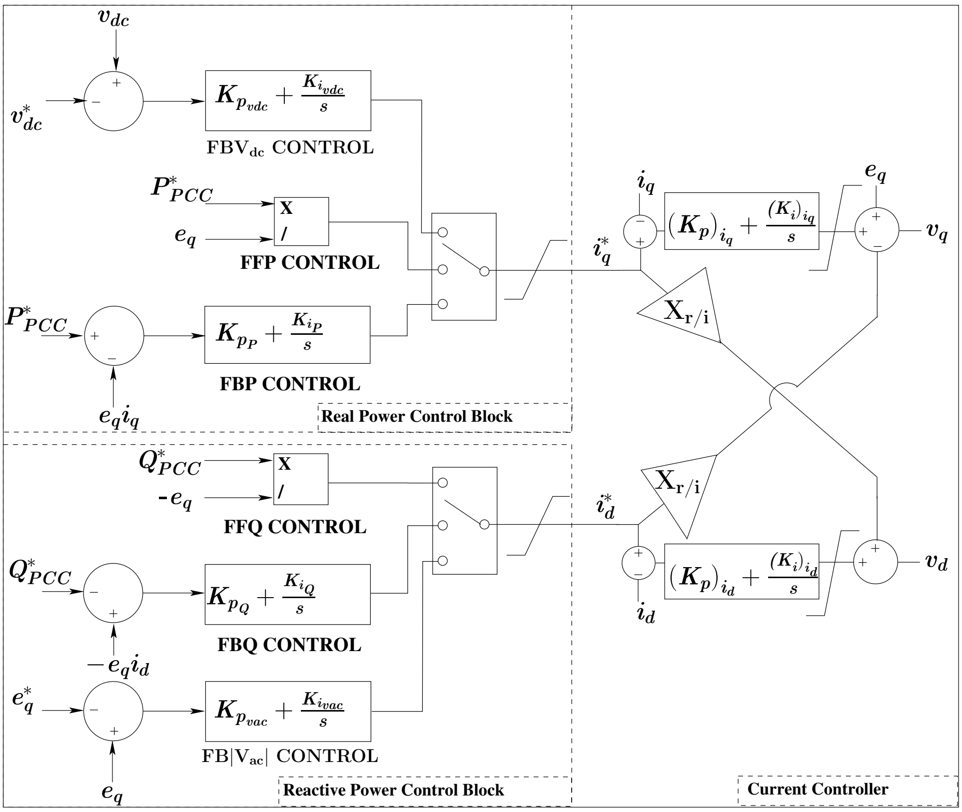

Figure 3.3: Control block of each converter

control the real power and the *d* axis current completely controls the reactive power as discussed in section 3.3.1.

The type of real and reactive power outer controller at each converter depends on the system and its requirements. Hence, a generalised control system model is presented. The subscripts '*r*' and '*i*' can be suitably attached to the controller parameters and quantities as applicable. The outer controller can be broadly classified as Feedforward (FF) and Feedback (FB) controller. The different types of controllers are :

- Feedback DC voltage control (FBV$_{\text{dc}}$ control): It maintains constant DC side voltage of the converter. A reference DC voltage (v^*_{dc}) is compared against measured DC voltage (v_{dc}) and is sent to a PI controller to obtain *q* axis reference current (i^*_q) as given in (3.9). The PI control constants are $K_{p_{vdc}}$ and K_{ivdc} .

$$i^*_q = (K_{p_{vdc}} + \frac{K_{ivdc}}{s})(v_{dc} - v^*_{dc}) \tag{3.9}$$

- Feedforward active and reactive power control (FFP and FFQ control): The real and reactive power references at the PCC (P^*_{PCC} and Q^*_{PCC}) directly decide the current references. There is no feedback loop involved. Hence, from (3.5) the reference currents can be obtained as :

$$\begin{aligned} i^*_q &= \frac{P^*_{PCC}}{e_q} \\ i^*_d &= \frac{-Q^*_{PCC}}{e_q} \end{aligned} \tag{3.10}$$

- Feedback active and reactive power control (FBP and FBQ control): The measured active and reactive power at the PCC bus are compared with the reference through a feedback loop and the error is sent to PI controllers to obtain the current references.

$$\begin{aligned} i^*_q &= (K_{pP} + \frac{K_{iP}}{s})(P^*_{PCC} - P_{PCC}) \\ i^*_d &= (K_{pQ} + \frac{K_{iQ}}{s})(Q_{PCC} - Q^*_{PCC}) \end{aligned} \tag{3.11}$$

  K_{pP}, K_{iP}, K_{pQ} and K_{iQ} are the PI constants.

- Feedback AC voltage control (FB|V$_{\text{ac}}$|): In this control, the AC voltage magnitude at the PCC, e_q, is maintained constant through a PI controller. The PI constants are $K_{p_{vac}}$ and $K_{i_{vac}}$.

$$i^*_d = (K_{p_{vac}} + \frac{K_{i_{vac}}}{s})(e_q - e^*_q) \tag{3.12}$$

Appropriate limits are applied to the reference currents.

3.3.3.2 Inner controller design

It can be seen from the converter model given in equations (3.7) and (3.8) that the q and d axis current can be controlled by the converter voltages v_q and v_d. The model also indicates that there exists a cross-coupling between the two components.

In order to decouple them, the converter voltages are controlled as follows :

$$\begin{aligned} v''_q &= u_q - Xi_d + e_q \\ v''_d &= u_d + Xi_q \end{aligned} \tag{3.13}$$

where v''_q and v''_d are the controlled converter voltages. The terms Xi_d and Xi_q are the feedforward terms used to compensate the coupling between the q and d axis current components.

u_q and u_d are the two new state variables obtained from the outer controller current references as :

$$\begin{aligned} u_q &= \left((K_p)_{i_q} + \frac{(K_i)_{i_q}}{s} \right) (i_q^* - i_q) \\ u_d &= \left((K_p)_{i_d} + \frac{(K_i)_{i_d}}{s} \right) (i_d^* - i_d) \end{aligned} \tag{3.14}$$

Appropriate limits are placed on u_q and u_d.

Under normal conditions *i.e.* with no modulation limits hit, the converter AC side voltages, $v_q = v''_q$ and $v_d = v''_d$. Substituting the control equation (3.13) in the converter equations (3.7) and (3.8), we get,

$$\begin{aligned} \frac{di_q}{dt} &= -\frac{\omega_{gB}}{X} R i_q + \frac{\omega_{gB}}{X} u_q \\ \frac{di_d}{dt} &= -\frac{\omega_{gB}}{X} R i_d + \frac{\omega_{gB}}{X} u_d \end{aligned} \tag{3.15}$$

Thus, with the control adopted, the currents respond to u_q and u_d as two separate first order systems without any coupling.

3.3.4 DC link model

The basic differential equations on the DC side of the converters in per-unit are given as :

$$\begin{aligned} \frac{dv_{dcr}}{dt} &= K_{dc}[i_{dc_1} - i_{cc}] \\ \frac{dv_{dci}}{dt} &= K_{dc}[i_{dc_2} + i_{cc}] \\ \frac{di_{cc}}{dt} &= \frac{\omega_{gB}}{L_{dc}}[v_{dcr} - v_{dci} - R_{dc} i_{cc}] \end{aligned} \tag{3.16}$$

where $K_{dc} = \frac{\omega_{gB}}{C_{dc}}$. The initial conditions of the above equations are obtained from DC power flow.

3.3.5 AC-DC coupling equations

The AC and DC equations are related to each other through power balance equations. As the converter losses are neglected in this study, the converter AC side power is assumed to be equal to the DC power. Hence, equations for i_{dc_1} and i_{dc_2} are :

$$\begin{aligned} i_{dc_1} &= \frac{-(v_{q_r}i_{q_r} + v_{d_r}i_{d_r})}{v_{dcr}} \\ i_{dc_2} &= \frac{-(v_{q_i}i_{q_i} + v_{d_i}i_{d_i})}{v_{dci}} \end{aligned} \tag{3.17}$$

3.3.6 Interfacing to the AC network

For interfacing VSC-HVDC to the network, currents in the dq frame have to be transformed back to DQ frame. The transformation is given as:

$$f_Q + jf_D = (f_q + jf_d)e^{j\theta} \tag{3.18}$$

The above equation is a non linear algebraic equation and to avoid its iterative solution, the following approach as discussed in (Shubhanga, 2018) is used to obtain the final injected currents i_{Q_r}, i_{Dr}, i_{Q_i} and i_{Di}.

$$\begin{aligned} \frac{di_{Q_r}}{dt} &= \frac{1}{T_L}(-i_{Q_r} + i'_{Q_r}) \ , \ \frac{di_{Dr}}{dt} = \frac{1}{T_L}(-i_{Dr} + i'_{Dr}) \\ \frac{di_{Q_i}}{dt} &= \frac{1}{T_L}(-i_{Q_i} + i'_{Q_i}) \ , \ \frac{di_{Di}}{dt} = \frac{1}{T_L}(-i_{Di} + i'_{Di}) \end{aligned} \tag{3.19}$$

where

$$\begin{aligned} i'_{Q_r} + ji'_{Dr} &= (i_{q_r} + ji_{d_r})e^{j\theta_r} \\ i'_{Q_i} + ji'_{Di} &= (i_{q_i} + ji_{d_i})e^{j\theta_i} \end{aligned} \tag{3.20}$$

Thus the complex VSC-HVDC current injections are given as :

$$\begin{aligned} \bar{I}_{DQ_r} &= i_{Q_r} + ji_{D_r} \\ \bar{I}_{DQ_i} &= i_{Q_i} + ji_{D_i} \end{aligned} \tag{3.21}$$

The current injection model of VSC-HVDC link is presented in Figure 3.4.

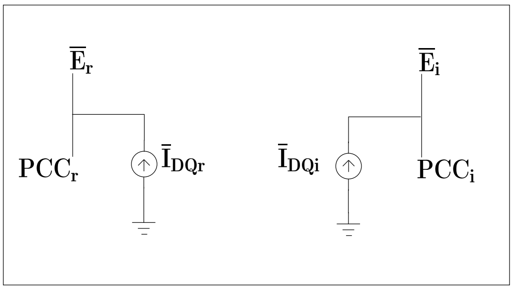

Figure 3.4: Current injection model of VSC-HVDC link

The VSC-HVDC currents are vectorised as :

$$\underline{\bar{I}}_{vschvdc} = \begin{cases} \bar{I}_{DQr} & : \text{At the rectifier side PCC bus.} \\ \bar{I}_{DQi} & : \text{At the inverter side PCC bus.} \\ 0 & : \text{At other buses.} \end{cases}$$

As vectorisation is done, this method can be adopted to a system containing any number of VSC-HVDC links.

The bus voltages of the network are calculated as :

$$\underline{\bar{E}}_{DQ} = (\underline{\bar{I}}_{Gs} - \underline{\bar{I}}_{Ls} - \underline{\bar{I}}_{vschvdc})/Y_{BUS} \tag{3.22}$$

where, $\underline{\bar{E}}_{DQ}$ is the bus voltage vector, $\underline{\bar{I}}_{Gs}$ is the vector of generator source currents, $\underline{\bar{I}}_{Ls}$ is the load current vector and Y_{BUS} is the admittance matrix of the system.

3.4 Impact of VSC-HVDC controls on ancillary frequency controllers

The basic real power control strategies employed for VSC-HVDC models donot respond to the frequency fluctuations of the power system. In order to provide frequency support, the frequency deviation can be detected and converted into an additional power reference in the active power controller. In this study, two such types of frequency support control strategies are used, namely droop control (R type) and PI control. The power frequency droop and PI based frequency controllers are respectively characterized as,

$$P_f^* = \big(-\frac{1}{R_f}\big)\delta F \tag{3.23}$$

$$P_f^* = -\big(K_{pf} + \frac{K_{if}}{s}\big)\delta F \tag{3.24}$$

where P_f^* is the modulated power reference and δF is the frequency deviation. The modulated power is added along with the initial power reference (P_{PCC}^*) to obtain the actual power reference.

$$P_{tPCC}^* = P_{PCC}^* + P_f^* \tag{3.25}$$

3.4.1 Linearized analytical model

In this section, analytical models of the FFP and FBP controllers are derived. The reactive power controllers can be modelled similarly. It is assumed that the PCC is connected via an impedance $R_l + jX_l$ to an AC system bus with voltage of $v_{lq} + jv_{ld}$.
Linearizing q-axis equation of (3.15),

$$\begin{aligned} s\Delta i_q &= -\frac{\omega_{gB}}{X}R\Delta i_q + \frac{\omega_{gB}}{X}\Delta u_q \\ \Delta u_q &= \frac{\frac{\omega_{gB}}{X}}{s + \frac{\omega_{gB}R}{X}}\Delta i_q \end{aligned} \tag{3.26}$$

From equation (3.14),

$$\Delta u_q = \left((K_p)_{i_q} + \frac{(K_i)_{i_q}}{s}\right)(\Delta i_q^* - \Delta i_q) \tag{3.27}$$

Combining the equations, the inner current controller transfer function is given as,

$$\frac{\Delta i_q}{\Delta i_q^*} = \frac{(K_p)_{i_q}\frac{\omega_{gB}}{X}s + (K_i)_{i_q}\frac{\omega_{gB}}{X}}{s^2 + \left(R + (K_p)_{i_q}\right)\frac{\omega_{gB}}{X}s + (K_i)_{i_q}\frac{\omega_{gB}}{X}} \tag{3.28}$$

The feedforward real power control can be linearized from q-axis equation of (3.10) as,

$$\Delta i_q^* = \frac{\Delta P_{PCC}^*}{e_{q0}} - \frac{P_{0PCC}^*}{e_{q0}^2}\Delta e_q \tag{3.29}$$

The feedback real power control can be linearized from q-axis equation of (3.11) as,

$$\Delta i_q^* = (K_{PP} + \frac{K_{iP}}{s})(\Delta P_{PCC}^* - \Delta P_{PCC}) \tag{3.30}$$

Linearizing real power equation, $P_{PCC} = e_q i_q$, ΔP_{PCC} can be obtained as,

$$\Delta P_{PCC} = e_{q0}\Delta i_q + i_{q0}\Delta e_q \tag{3.31}$$

The dynamic equations governing the current can be also written as,

$$\frac{di_q}{dt} = \frac{\omega_{gB}}{X_t}[v_q - R_t i_q + X_t i_d - v_{lq}] \tag{3.32}$$

$$\frac{di_d}{dt} = \frac{\omega_{gB}}{X_t}[v_d - R_t i_d - X_t i_q - v_{ld}] \tag{3.33}$$

where $X_t = X + X_l$ and $R_t = R + R_l$.
Combining equations (3.7) and (3.32), and then linearizing them,

$$\Delta e_q = \frac{X_s}{X_t}\Delta v_q + \frac{R_t X + X_t R}{X_t}\Delta i_q + \frac{X}{X_t}\Delta v_{sq} \tag{3.34}$$

From the q-axis equation of (3.13),

$$\Delta v_q = \Delta u_q - X\Delta i_d + \Delta e_q \tag{3.35}$$

From equations (3.34) and (3.35), Δe_q is

$$\Delta e_q = \frac{X_s}{X}\Delta u_q + \frac{R_t X + X_t R}{X}\Delta i_q + \Delta v_{sq} - X_s\Delta i_d \tag{3.36}$$

The closed loop transfer functions of the feedforward and feedback active power controllers can be obtained through equations (3.29), (3.30), (3.31), (3.28) and (3.36). In (Wang W. et al., 2014), it was observed that the feedforward power loop for rectifying operation of converter caused undesirable effects due to the positive feedback. In this work, the inverting operation of converter is studied. The inverter of the VSC-HVDC link performs active power control. The analysis done above reveals that the feedforward loop forms a negative feedback system for inverter operation. The effect of feedback loops is obtained through transfer function based bandwidth analysis where the bandwidth of FBP controllers are varied while all the other outer controllers are maintained at the initial settings.

3.4.2 Simulation and analysis

The two areas of the 4-machine system in Figure 2.7 are connected by a 200 km VSC-HVDC link carrying power from area-1 to area-2 forming an asynchronous system as shown in Figure 3.5 and is used for the study. The parameters of the VSC-HVDC link are given in the Appendix A2. Rectifier (converter associated with PCC bus-9) controls the DC link voltage and inverter (converter associated with PCC bus-10) controls the active power. The frequency controller is introduced alongside the real power controller of inverter. The frequency deviation in the receiving area *i.e.* area-2 is tracked at bus-10. The modulated power is obtained through frequency control strategies discussed. The feedback active power loops are tuned for a set of required bandwidths for comparison purpose. The gains are tuned using the analytical models in section 3.4.1 and by the method specified in

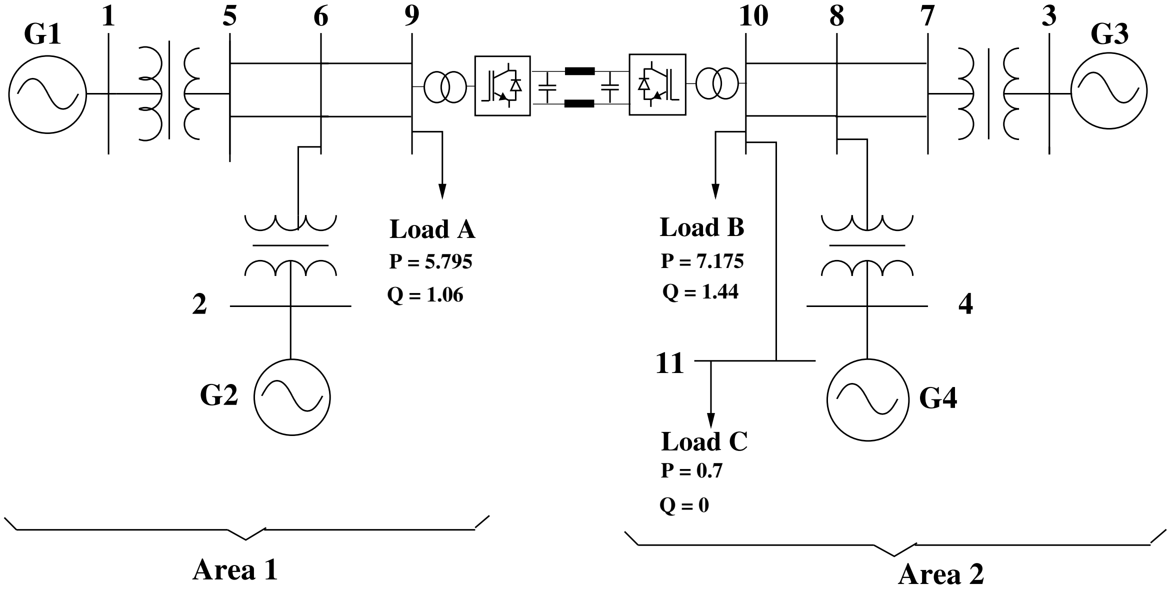

Figure 3.5: 2-area, 4-machine asynchronous VSC-HVDC system

(Li S. et al., 2016) and (Giddani et al., 2012). The frequency controller parameters are R_f = 0.05, K_{pf} = 20 and K_{if} = 100.

3.4.3 Impact of active power controller bandwidth

The impact of active power controller bandwidth on the performance of the frequency controllers is examined in this section. For this analysis, two independent events are applied in area-2. The first event pertains exclusively to real power load change in the system whereas the second event is a 3-phase to ground fault that affects both real and reactive power of the system. All the inner current controllers are maintained with a bandwidth of 240 Hz. The performance of each frequency controller added with a) FFP controller b) FBP controller with 15 Hz bandwidth c) FBP controller with 30 Hz bandwidth d) FBP controller with 60 Hz bandwidth is compared for each event. The outer DC voltage controller bandwidth is maintained at 6 Hz. For reactive power control, both VSCs employ FBQ controller with a bandwidth of 15 Hz.

3.4.3.1 Load change in area-2

At 1s, a purely real power load is added at bus-10 which constitutes to 4% of load increase in area-2. The behaviour of droop and PI type frequency control strategies is given in Figure 3.6 with FBP controller of 15 Hz bandwidth. The frequency deviation at bus-10 and the modulated power plots are presented. As expected, following the event, the frequency in area-2 decreases and the controller provides an additional power reference to maintain the frequency. It can be observed that with the onset of the event, there is a sudden initial transient in the quantities followed by a gradual change.

The impact of different active power controls on the performance of droop type frequency control strategy is given in Figure 3.7. It can be observed that with the onset of load change event, a greater initial frequency drop is detected with FFP control, whereas a lesser frequency drop is observed with FBP controller of 15 Hz bandwidth. The performance of droop control with FBP controller of 60Hz bandwidth is closest to that with FFP controller. The power output of the droop controller gets accordingly modified. The maximum power peak is found with FFP controller and minimum with FBP controller of 15 Hz. The PI type frequency control performs similarly with the different active power control cases. The frequency and power plots are given in Figure 3.8. Beyond 1.15s, the performance of the frequency controllers is similar with all the four active power control cases and they follow

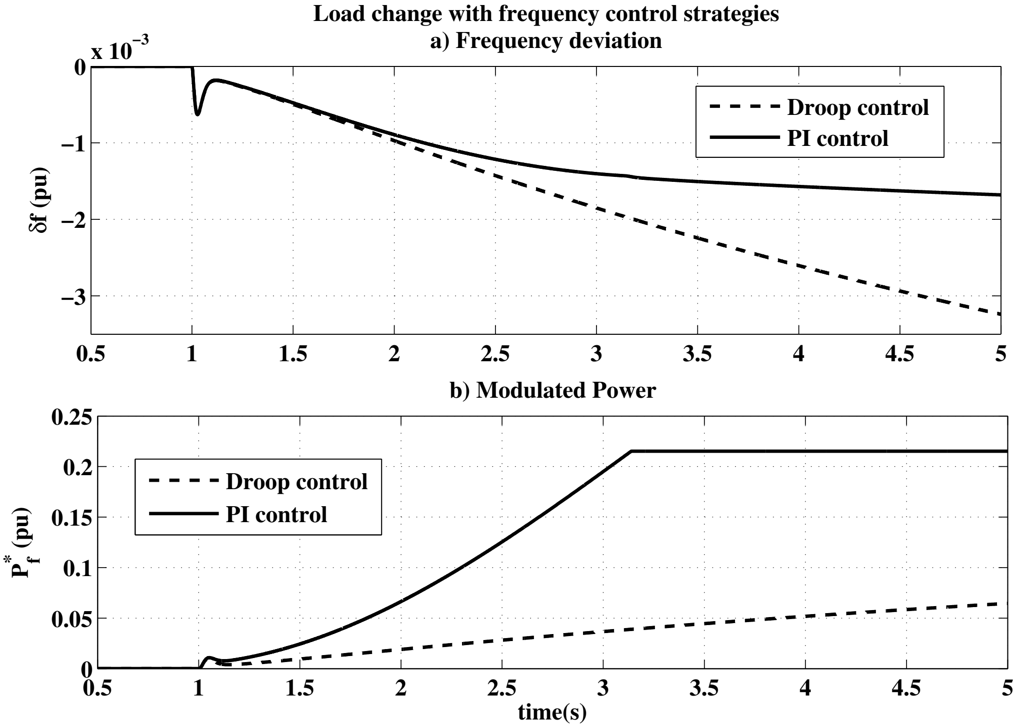

Figure 3.6: Performance of frequency control strategies for load change in area-2

the trajectory of Figure 3.6.

In order to bring about a quantitative comparison, the first swing maximum peaks of the modulated power following load change have been tabulated in Table 3.1. The power values are given in actuals (MW). It can be observed that, upon the onset of the event, there is a difference of 40 kW between the modulated power peaks with FFP control and that with FBP 15 Hz active power loop. This is observed when both droop and PI frequency controllers are used.

Table 3.1: The first swing maximum peaks of modulated power for load change

P_f^* (MW)	FFP	FBP 60Hz	FBP 30Hz	FBP 15Hz
Droop control	1.02	1.02	1.01	0.98
PI control	1.14	1.14	1.13	1.10

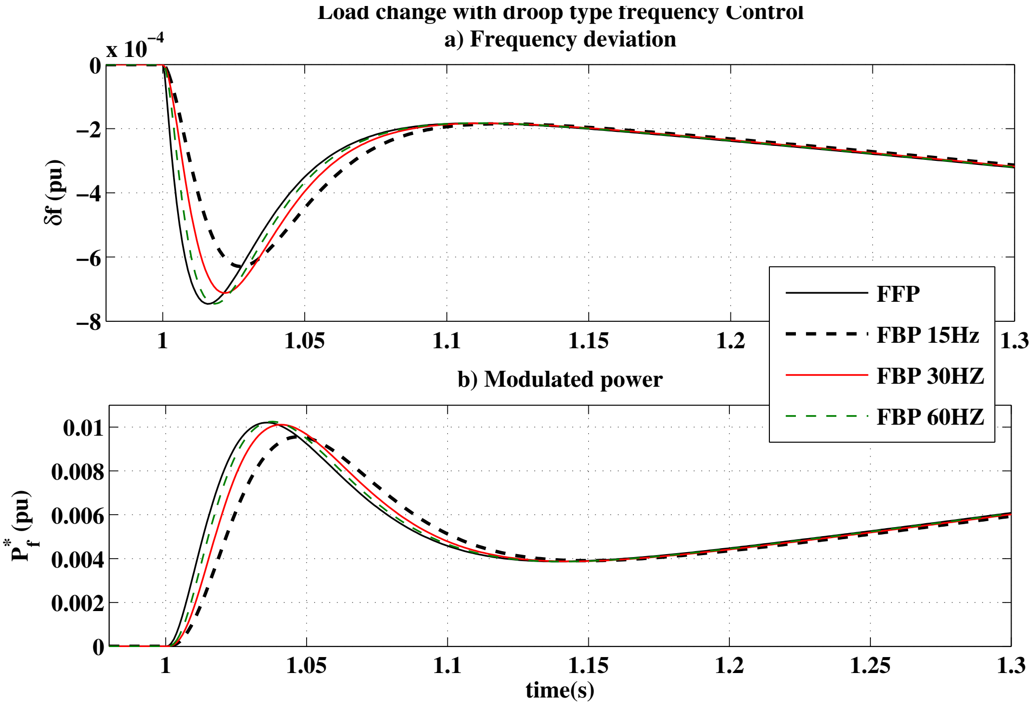

Figure 3.7: Load change : Comparison of performance of droop type frequency control with various active power loop bandwidths

3.4.3.2 3-phase to ground fault

A 3-phase to ground fault is applied at bus-7 at 1s. It leads to a voltage sag at bus-10. The performance of the two frequency controllers are provided through frequency and power plots in Figure 3.9. The controllers are added along with FBP control of 15 Hz bandwidth.

The performance of droop control and PI frequency control with various cases of active power control is given in Figure 3.10 and Figure 3.11 respectively. It can be observed that FF control provides a superior performance as compared to the various FB cases. Even here the performance with FBP of 60 Hz is closest to that of FFP controller. Beyond the initial high frequency oscillations, all the four active power controllers perform similarly according to plots in Figure 3.9.

The maximum peaks of the first swing of the modulated power following the 3-phase fault have been tabulated in Table 3.2. A large difference of 4.58 MW exists between the peaks of modulated power with FFP and that with FBP 15Hz active power loop. The plots

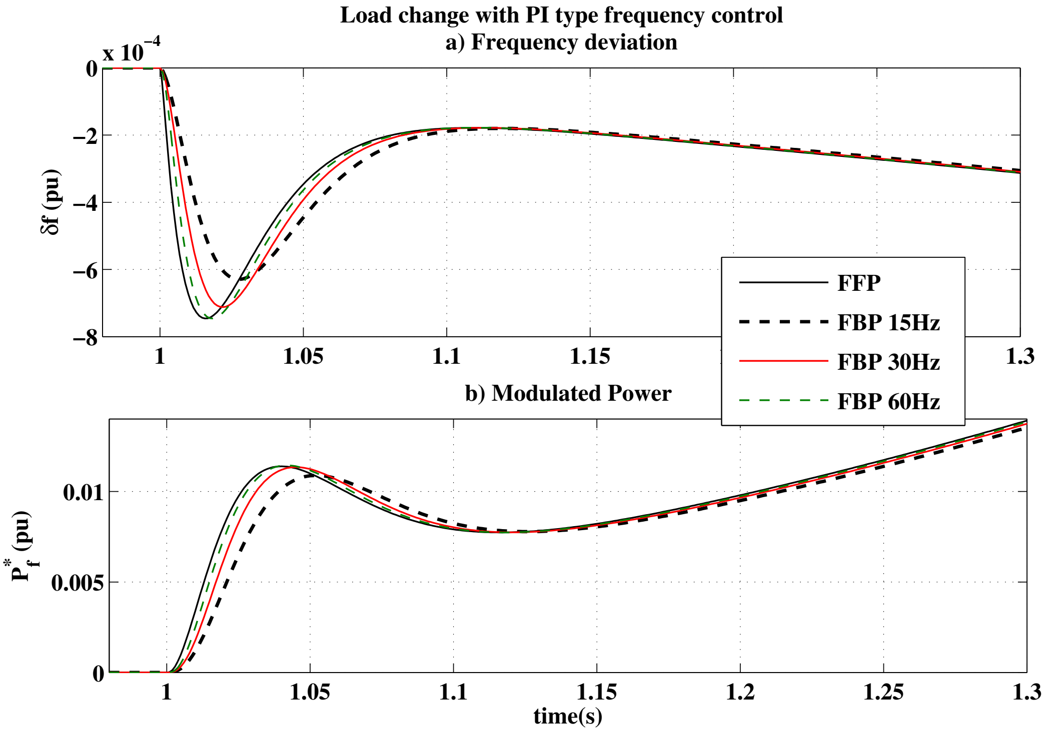

Figure 3.8: Load change : Comparison of performance of PI type frequency control for various active power loop bandwidths

are well differentiated in this case when compared to that with the load change.

Table 3.2: The first swing maximum peak of modulated power for 3-phase to ground fault

P_f^* (MW)	FFP	FBP 60Hz	FBP 30Hz	FBP 15Hz
Droop control	-0.55	0.72	2.04	4.03
PI control	-0.62	0.74	2.12	4.24

3.4.4 Dynamic performance comparison between Q and $|V_{AC}|$ control

In the previous case studies, the effect of active power control cases were examined using FBQ controller for reactive power control. In this section, the performance of frequency control is analysed for different type of reactive power controls *i.e.* FFQ controller, FBQ controller of 15 Hz bandwidth and $|V_{AC}|$ controller of 15 Hz bandwidth. This study allows us to determine if the influence of active power controller bandwidth must be explored

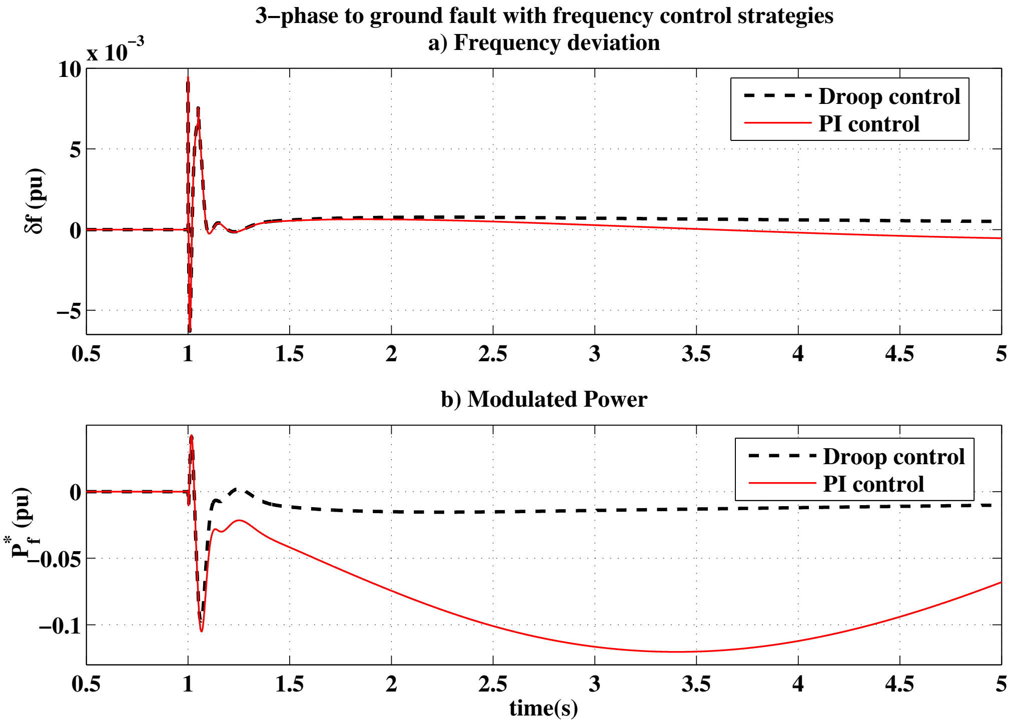

Figure 3.9: Performance of frequency control strategies for a 3-phase to ground fault in area-2

separately when other types of reactive power controllers are utilised. For the study, FBP controller of bandwidth 15 Hz is associated with the frequency controllers. All the inner controllers are of 240 Hz bandwidth. For a given case, both the VSC's use the same type of reactive power controller.

For a 4% increase of real power load in area-2, the performance of droop controller and PI frequency controller is respectively presented through modulated power plots in Figure 3.12a and Figure 3.12b. It can be observed that the performance is similar with all the three cases. This is due to the fact that load change is associated with real power control. Hence, the quantities pertaining to reactive power control remain unaffected due to the decoupling.

The modulated power plots of droop controller and PI frequency controller is given in Figure 3.13a and Figure 3.13b respectively for a 3-phase to ground fault in area-2. The behaviour of the frequency controllers remain similar with FFQ and FBQ controls. However, a significant difference can be observed in the behaviour with $|V_{AC}|$ type reactive power control. Due to the fault, there is a voltage sag in area-2 voltage which directly influences

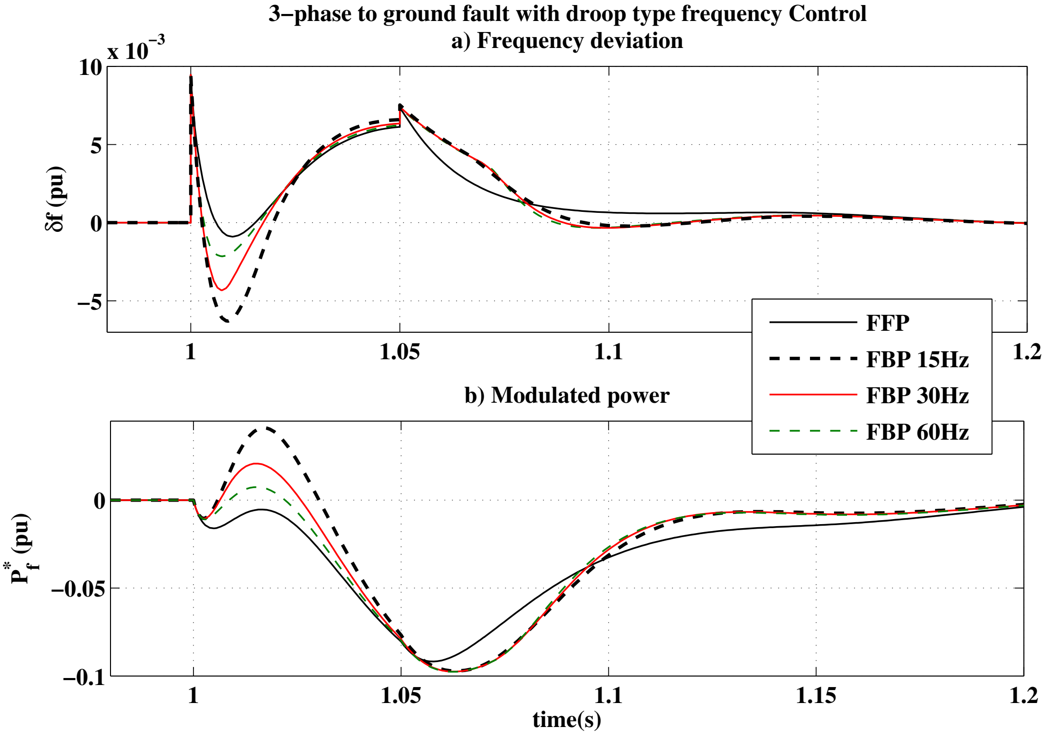

Figure 3.10: 3-phase to ground fault : Comparison of performance of droop type frequency control for various active power controller bandwidths

the real and reactive power control. As Q-controller and $|V_{AC}|$ controller control the reactive power differently, their interactions with the real power control vary and hence their behaviour.

3.4.5 Effect of active power control bandwidth with $|V_{AC}|$ type reactive power control

Based on the analysis done in the previous section, it is observed that the behaviour of the frequency controllers are similar with FFQ and FBQ controllers. However, it would be interesting to examine the performance with various active power control cases when $|V_{AC}|$ type reactive power controller is used for a 3-phase fault condition. The modulated power plots are provided in Figure 3.14 when PI type frequency controller is used. It was observed that with the onset of fault, the performance during the initial high frequency transient phase is similar to that shown in Figure 3.11 *i.e* with FBQ type reactive control. However,

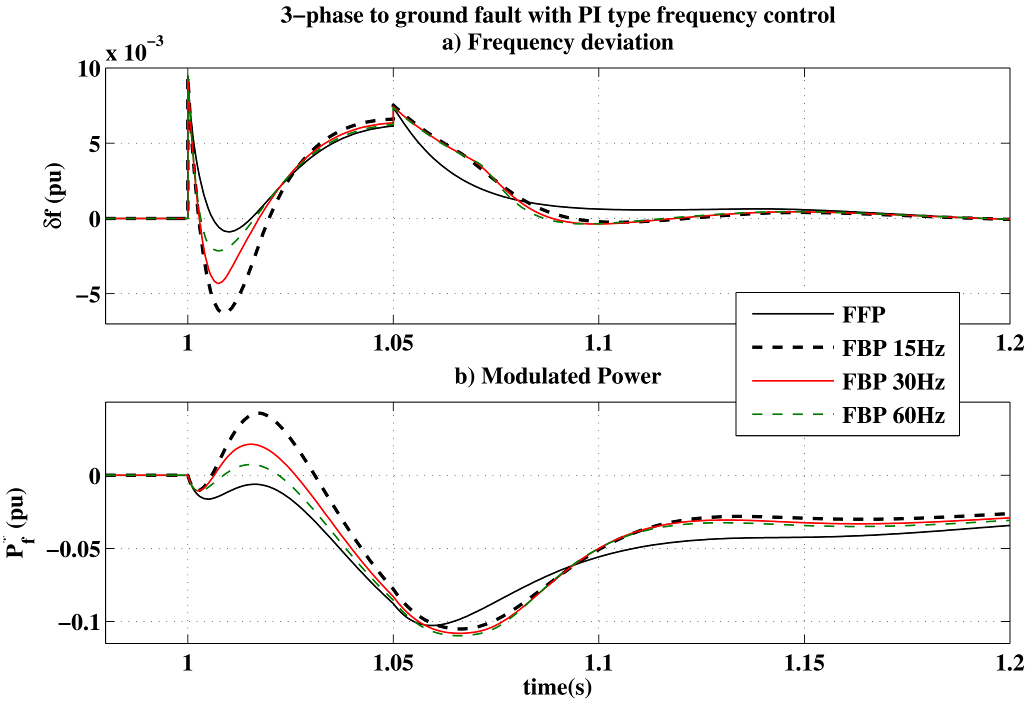

Figure 3.11: 3-phase to ground fault : Comparison of performance of PI type frequency control for various active power controller bandwidths

beyond 1.2s performance with FFP control displays larger low frequency oscillations when compared to FBP control cases. In the case with FBQ reactive control, performance with all active power control cases overlapped after 1.2s. The plots of droop frequency controller is not provided here as similar inferences were drawn.

3.5 Simplified model of VSC-HVDC

This section presents a simplified VSC-HVDC model designed for aiding AC system analysis. Existing literature encompasses a range of simplified approaches when it comes to modelling VSC-HVDC systems. It is proved in (Asvapoositkul and Preece, 2020), that representation of VSC-HVDC solely as power injections has reservations regarding location and control for small signal stability analysis. In addition, this kind of representation cannot be used for transient stability analysis. The simplified models obtained by eliminating time constants listed in literature survey are compared with full order models in

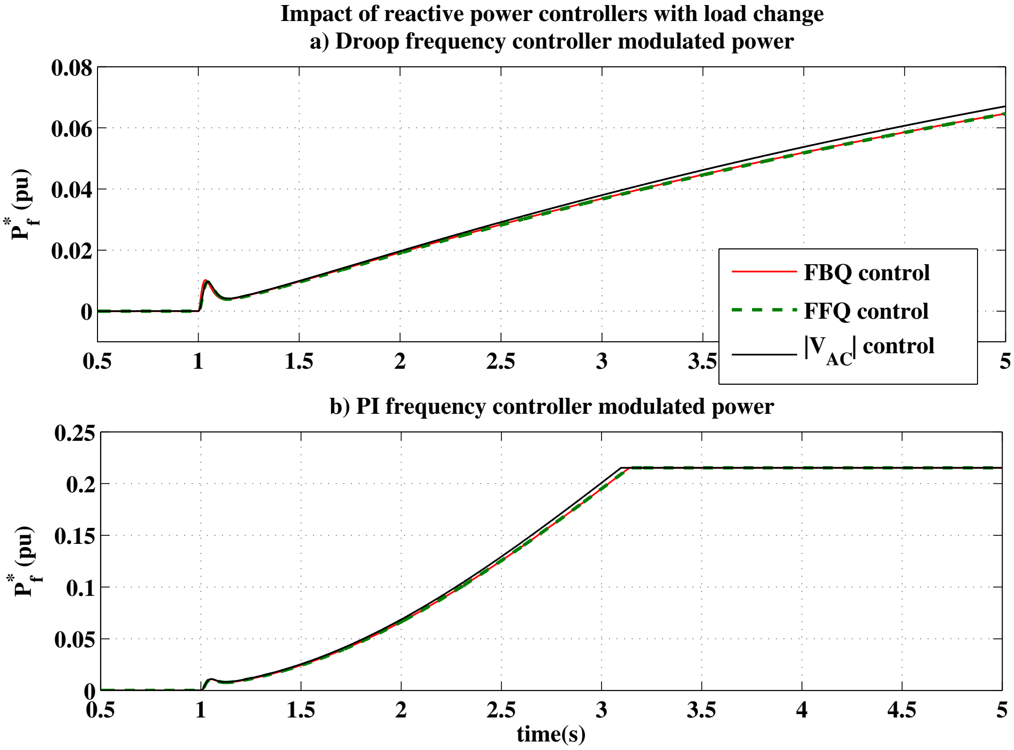

Figure 3.12: Effect of reactive power controllers for load change in area-2

(Cole and Ronnie, 2011). The dynamic performance of the models are insufficient for a VSC-HVDC system connected between two infinite buses rendering them unsuitable for multi-machine systems. Optimization and voltage source based reduction methodologies are out of scope of this research. In this study, a simplified model is presented and validated in multi-machine systems by comparing the modal and dynamic behaviour of the system to that of the system with model of section 3.3.

3.5.1 Dynamic model

In this section, the simplified model of VSC-HVDC is described. In the model, the DC circuit dynamics are eliminated. The phase reactor and transformer associated with the converter is considered as a part of the transmission network of the AC system in which the VSC-HVDC is connected. The control system is shifted from the control of PCC bus quantities to the control of converter bus quantities. This allows for the converter currents to be acquired directly from the real and reactive power controllers.

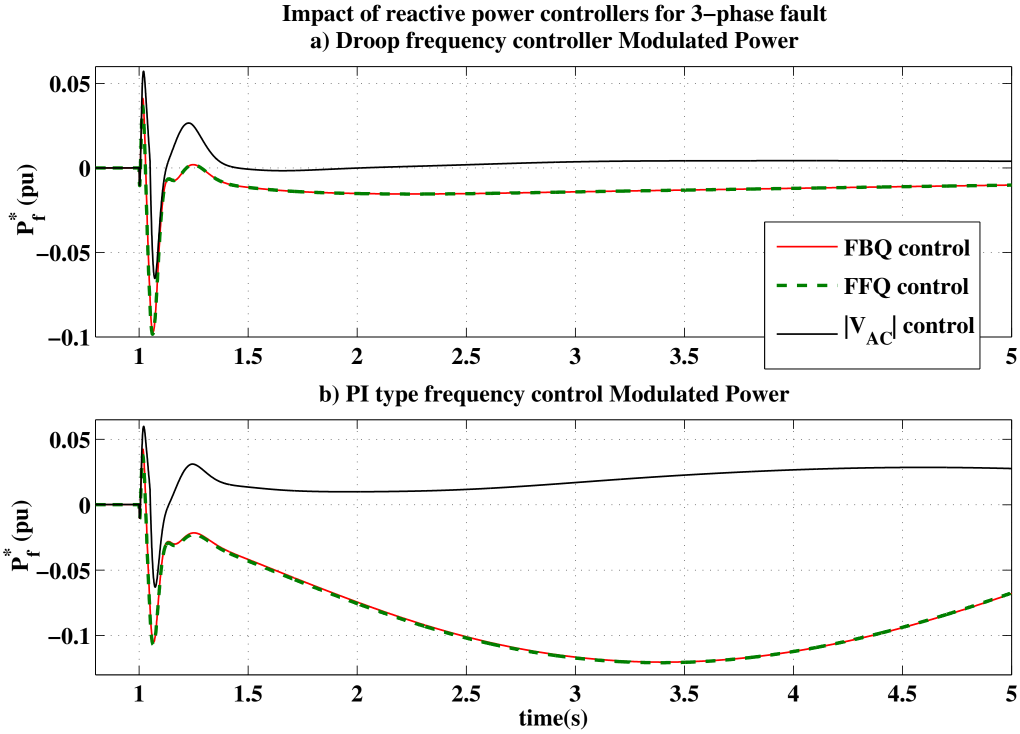

Figure 3.13: Effect of reactive power controllers for 3-phase to ground fault in area-2

In order to decouple the control process, the modelling is carried out in the dq frame. In this model, the quantities of converter buses (Bus-r and Bus-i) are controlled. The converter bus voltage is always aligned to the q-axis and d-axis is quadrature to it. The control system is presented in Figure 3.15.

Unlike full model, DC voltage control is not present in the simplified model due to the elimination of DC dynamics. Both the stations involve in real power control of the converter bus with equal real power references. Either reactive power or AC voltage magnitude of the converter bus is controlled. The real power controller directly provides the real part of the converter current, i_q, and the reactive power controller directly provides the reactive part, i_d. The control system is summarized below :

- Feedforward active and reactive power control (FFP and FFQ control): The active and reactive power references at the converter buses (P_c^* and Q_c^* respectively) directly

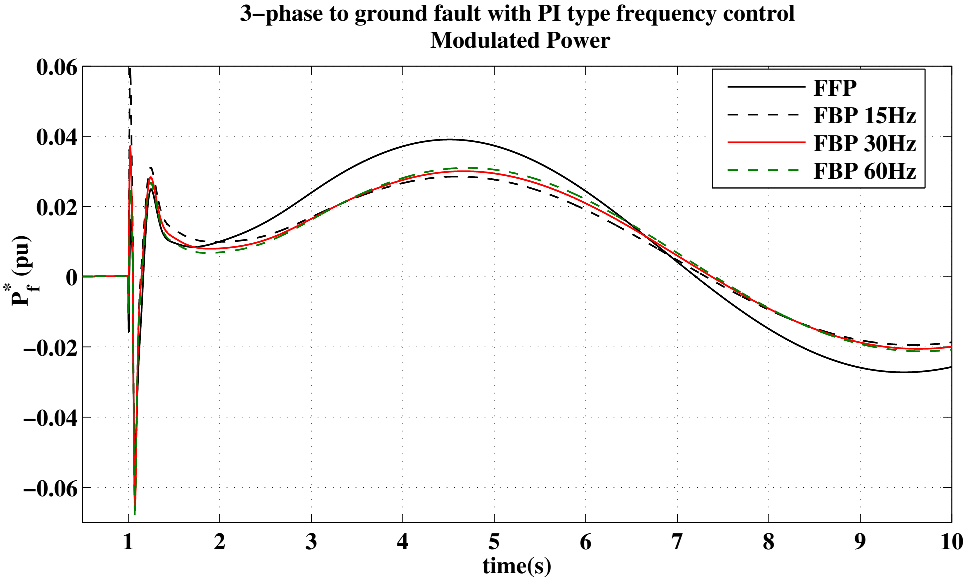

Figure 3.14: Comparison of performance of PI type frequency control for various active power controller bandwidths with $|V_{AC}|$ type reactive power controller

decide the current value.

$$i_q = \frac{P_c^*}{v_q} \;\; ; \;\; i_d = \frac{-Q_c^*}{v_q} \tag{3.37}$$

- Feedback AC voltage control (FB$|\mathrm{V_{ac}}|$ control): In this control, the AC voltage magnitude at the converter bus (v_q) is controlled using PI controller.

$$i_d = (K_{p_{vac}} + \frac{K_{ivac}}{s})(v_q - v_q^*) \tag{3.38}$$

- Feedback active and reactive power control (FBP and FBQ control): The measured active and reactive power at the converter bus (P_c and Q_c respectively) is compared with the reference through a feedback loop and the error is sent to PI controllers to obtain the currents directly.

$$\begin{aligned} i_q &= (K_{pP} + \frac{K_{iP}}{s})(P_c^* - P_c) \\ i_d &= (K_{pQ} + \frac{K_{iQ}}{s})(Q_c - Q_c^*) \end{aligned} \tag{3.39}$$

]

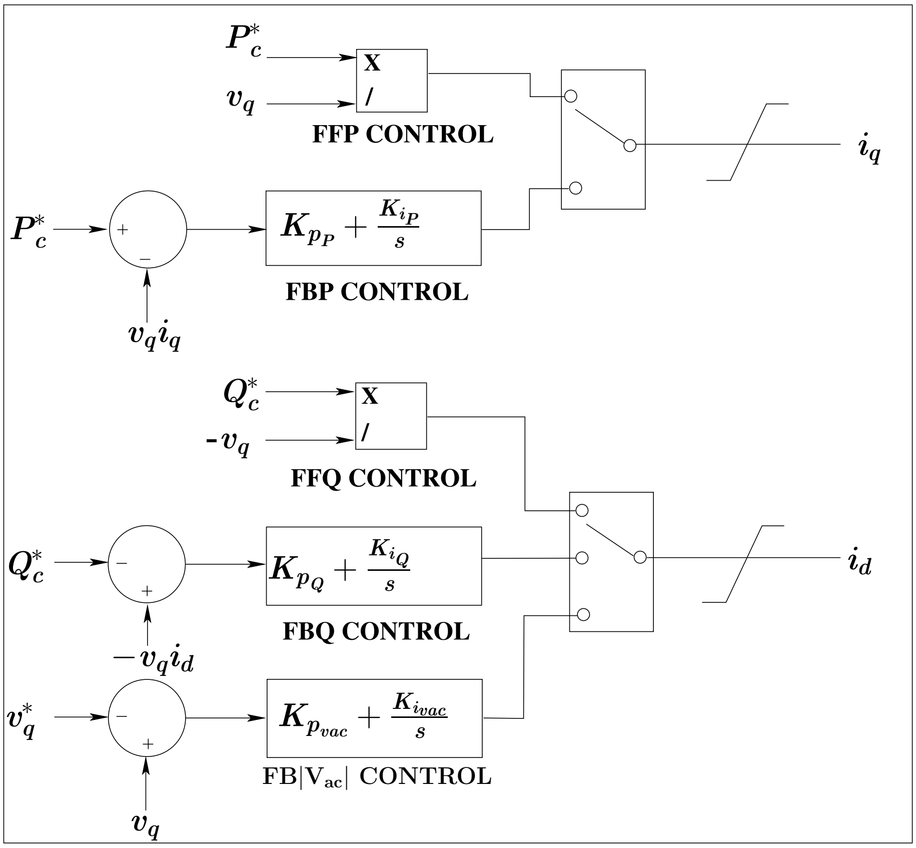

Figure 3.15: Control system of the simplified VSC-HVDC Model

The current injections obtained in dq frame are transformed back to DQ frame to interface to the network.

The currents are vectorised and are treated as current injections at the converter bus as :

$$\bar{\underline{I}}_{SM} = \begin{cases} \bar{I}_{DQr_{SM}} & \text{: At the rectifier converter bus.} \\ \bar{I}_{DQi_{SM}} & \text{: At the inverter converter bus.} \\ 0 & \text{: At other buses.} \end{cases}$$

The complex AC impedances $R_r + jX_r$ and $R_i + jX_i$ are included as a part of system transmission network. If n_{vsc} is the total number of two terminal VSC-HVDC links in the system, the number of transmission lines and number of buses increase by $2{*}n_{vsc}$ when a simplified model is used. Hence, the size of bus voltage vector and admittance matrix of the system gets modified accordingly. In this model, the converter as well as PCC bus voltages are calculated as a part of network solution. The bus voltages are calculated as :

$$\underline{\bar{V}}_{DQ} = (\underline{\bar{I}}_{Gs} - \underline{\bar{I}}_{Ls} - \underline{\bar{I}}_{SM})/Y_{BUS} \tag{3.40}$$

where, $\underline{\bar{V}}_{DQ}$ is the modified bus voltage vector, $\underline{\bar{I}}_{Gs}$ is the vector of generator source currents, $\underline{\bar{I}}_{Ls}$ is the load current vector and Y_{BUS} is the modified admittance matrix of the system. The simplified model is represented in Figure 3.16.

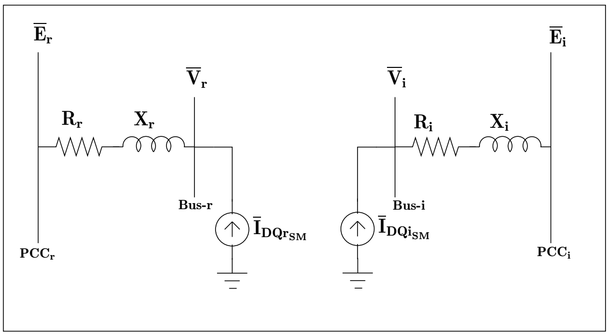

Figure 3.16: Simplified model

3.5.2 Case studies

In order to get an understanding on the behaviour of VSC-HVDC links with respect to its modelling intricacies, case studies have been undertaken using two multi-machine AC systems. A two-area, 4-machine system and a large 16-machine, 68-bus system is used. VSC-HVDC links are connected in appropriate locations to analyse the modal and dynamic performance of the AC systems with the discussed dynamic models.

The various control scenarios of a VSC-HVDC link used in this study are presented in Table 3.3. Converter - A represents the DC voltage controlling station and Converter - B represents the real power controlling station. The DC link voltage controller is replaced by a real power controller when simplified model is utilised.

The parameters of the VSC-HVDC link is given in the Appendix A2. All the quantities are per unitised on a base of 100 *MVA* for both the systems and applications.

The model discussed in section 3.3 will be referred as full model (FM) and the simplified model discussed in section 3.5.1 will be referred as simplified model (SM).

Table 3.3: VSC-HVDC control strategies

Q - control	Converter - A	Converter - B
FF - type	$\mathrm{FBV_{dc}}^{*}$, FFQ	FFP, FFQ
FB - type	$\mathrm{FBV_{dc}}^{**}$, FBQ	FBP, FBQ

$\mathbf{\lvert V_{ac} \rvert}$ **control**	Converter - A	Converter - B
FF - type	$\mathrm{FBV_{dc}}^{*}$, $\mathrm{FB\lvert V_{ac} \rvert}$	FFP, $\mathrm{FB\lvert V_{ac} \rvert}$
FB - type	$\mathrm{FBV_{dc}}^{**}$, $\mathrm{FB\lvert V_{ac} \rvert}$	FBP, $\mathrm{FB\lvert V_{ac} \rvert}$

* - FFP in case of simplified model

** - FBP in case of simplified model

3.5.2.1 Two-area, 4-machine system

The two-area, 4-machine system shown in Figure 2.7 is used in this study. Under this base case, the modes of the system and their attributes *i.e.* frequency (f) and damping factor (DF) are given in Table 3.4.

Table 3.4: Modes of two-area, 4-machine base system

	Eigenvalue	f (*Hz*)	DF
Inter-Area Mode	$-0.3863 \pm j3.3867$	0.5392 *Hz*	0.1133
Local mode Area-2	$-1.5576 \pm j4.9857$	0.7935 *Hz*	0.2982
Local mode Area-1	$-2.7765 \pm j6.2008$	0.9869 *Hz*	0.4087

In order to conduct case studies, a 200 km VSC-HVDC link is used to replace line-2 of the system, with rectifier (Converter-A) at bus-9 and inverter (Converter-B) at bus-10 as shown in Figure 3.17. For three levels of power in the HVDC link given in Table 3.5, the modal analysis results are presented in Table 3.6 and Table 3.7. $\mathrm{P_{HVDC}}$ refers to the power in the VSC-HVDC link and $\mathrm{P_3}$ refers to power in the AC line - 3 from bus-9. The characteristics of all the modes of the system with simplified model is compared to system with full model.

Table 3.5: Power levels in the VSC-HVDC link for the case studies

Case	% of total Power through VSC-HVDC (approx)	$\mathrm{P_{HVDC}}$	$\mathrm{P_3}$
1	25 %	0.2758	0.8267
2	50 %	0.5516	0.5509
3	75 %	0.8274	0.2750

The attributes of the inter-area mode with controls of Table 3.3 employed in the link

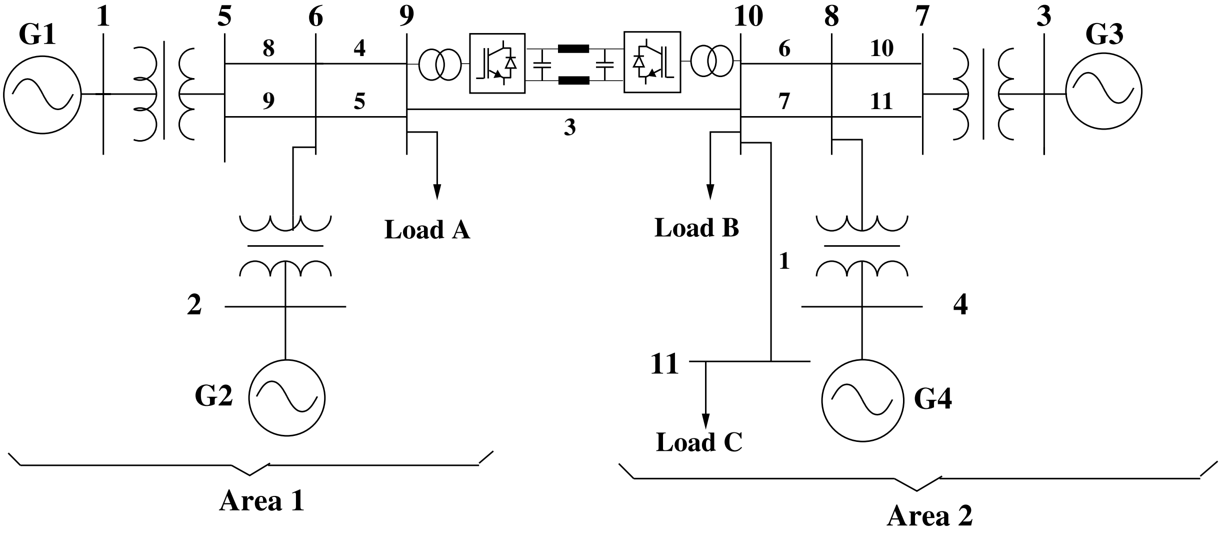

Figure 3.17: Two-area, 4-machine system

are given in Table 3.6. It can be clearly seen that the frequency and damping factor of the inter-area mode when simplified model is used is similar to that when full model is used for all cases of Table 3.5. The characteristics of inter-area mode for the system with full model of link reveal that, with reactive power control as $|V_{ac}|$ - control a higher frequency and damping factor is observed when compared to reactive power control as Q-control. In addition, as the power level in the HVDC link increases, the mode features with Q-control remain nearly the same. However, there is a variation in the frequency and damping factor with $|V_{ac}|$ - control. All of the aforementioned is well captured when simplified model of VSC-HVDC link is used.

Table 3.6: Attributes of Inter-area mode

Type of Model	Case	**Q-control**				**$|V_{ac}|$-control**			
		FF - type		FB - type		FF - type		FB - type	
		f (*Hz*)	DF	f (*Hz*)	DF	f (*Hz*)	DF	f (*Hz*)	DF
Full model	1	0.4390 *Hz*	0.0723	0.4390 *Hz*	0.0724	0.4416 *Hz*	0.0768	0.4417 *Hz*	0.0768
	2	0.4409 *Hz*	0.0723	0.4409 *Hz*	0.0723	0.4440 *Hz*	0.0885	0.4451 *Hz*	0.0838
	3	0.4421 *Hz*	0.0721	0.4418 *Hz*	0.0728	0.4474 *Hz*	0.0899	0.4459 *Hz*	0.0873
Simplified model	1	0.4389 *Hz*	0.0728	0.4392 *Hz*	0.0718	0.4403 *Hz*	0.0804	0.4406 *Hz*	0.0802
	2	0.4409 *Hz*	0.0725	0.4411 *Hz*	0.0734	0.4421 *Hz*	0.0865	0.4426 *Hz*	0.0830
	3	0.4417 *Hz*	0.0727	0.4422 *Hz*	0.0725	0.4436 *Hz*	0.0869	0.4432 *Hz*	0.0843

The properties of the local mode of area-2 is given in Table 3.7. They are identical for both the models. It can be observed that given a case with full model, the frequency with $|V_{ac}|$ - control is greater than that of Q - control whereas the damping factor of the mode does not show much variation. The system with simplified model also represents this effectively. Comparing the characteristics of the local mode of area-1 with the system with simplified model to that of the full model yields similar results, hence it is not reported here.

Table 3.7: Attributes of Local mode of area-2

Type of Model	Case	**Q-control**				**$\|V_{ac}\|$-control**			
		FF - type		FB - type		FF - type		FB - type	
		f (*Hz*)	DF	f (*Hz*)	DF	f (*Hz*)	DF	f (*Hz*)	DF
Full model	1	0.7899 *Hz*	0.3053	0.7900 *Hz*	0.3057	0.7982 *Hz*	0.3032	0.7988 *Hz*	0.3039
	2	0.7871 *Hz*	0.3068	0.7875 *Hz*	0.3069	0.8012 *Hz*	0.3097	0.8013 *Hz*	0.3032
	3	0.7860 *Hz*	0.3077	0.7867 *Hz*	0.3104	0.8021 *Hz*	0.3091	0.8031 *Hz*	0.3047
Simplified model	1	0.7896 *Hz*	0.3068	0.7907 *Hz*	0.3044	0.8015 *Hz*	0.3058	0.8016 *Hz*	0.3069
	2	0.7863 *Hz*	0.3078	0.7902 *Hz*	0.3086	0.8036 *Hz*	0.3112	0.8032 *Hz*	0.3067
	3	0.7848 *Hz*	0.3107	0.7873 *Hz*	0.3126	0.8052 *Hz*	0.3107	0.8061 *Hz*	0.3077

In order to compare the dynamic performance, the system is initially made to work with Case-2 power level *i.e.* around 0.5516 pu of power in the link as well as AC line-3. At 1s, a step change in the reference power is applied such that 75 % of total power flows through the VSC-HVDC link (case-3) upon step. The plots for power in the HVDC link (P_{HVDC}) and power in AC Line-3 (P_3) are given in Figures 3.18 and 3.19 for FF-control strategy of VSC-HVDC link in the system for both simplified and full models. It can be clearly observed that the plots of both the models exactly overlap each other. As Line-3 connects two areas, the oscillations in P_3 depict the inter-area mode, justifying the results of the modal analysis. The FB - control yields similar findings and hence the plots are not included here.

Further, the base two-area system in Figure 2.7 is modified by replacing both Line-2 and Line-3 by a single VSC-HVDC link to form an asynchronous system. The VSC-HVDC link carries the total power from area-1 to area-2. The system would only have local modes. The frequency and damping factor of the modes obtained for the control strategies in Table 3.3 is presented in Table 3.8. The attributes of the modes with simplified and full model are similar.

The dynamic response of the asynchronous system is verified in the next section by introducing additional frequency control to the link. From the above analysis, it can be proven that the generic 4-machine system modelled with simplified VSC-HVDC performs

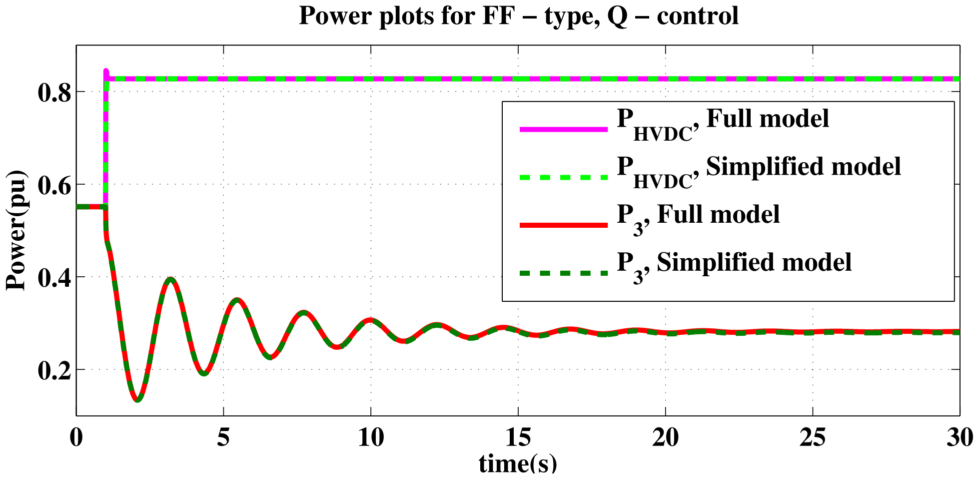

Figure 3.18: P_{HVDC} and P_3 plots for FF - type, Q-control

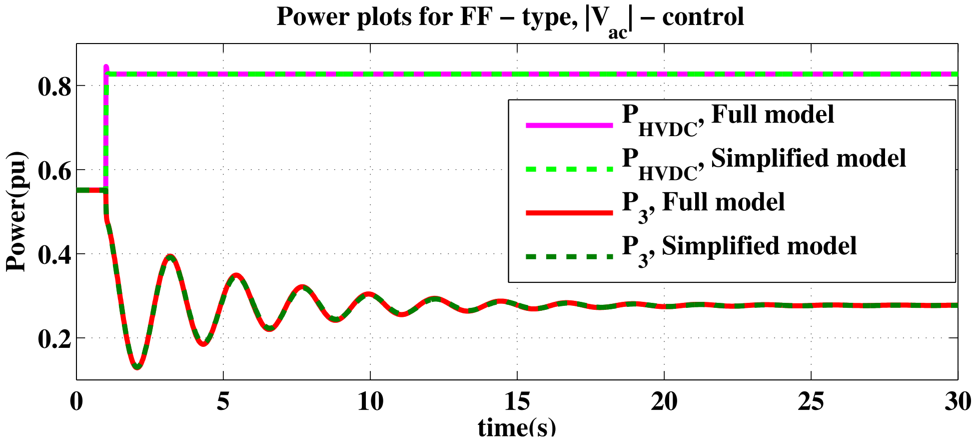

Figure 3.19: P_{HVDC} and P_3 plots for FF - type, $|V_{ac}|$ - control

similar to that modelled with full model. In order to further prove the efficiency of the simplified model, case studies are conducted with a larger test system with multiple DC links in section 3.5.2.3.

3.5.2.2 Influence of dynamic modelling on the working of frequency control strategies

In this section, the asynchronous VSC-HVDC system discussed in Figure 3.5 with frequency control strategies is used. The case study is conducted for load-C tripped at 1s. The

Table 3.8: Modes for Asynchronous 4 - machine system

	Local mode of area-2				**Local mode of area-1**			
Type of Model	FF - type		FB - type		FF - type		FB - type	
	f (*Hz*)	DF	f (*Hz*)	DF	f (*Hz*)	DF	f (*Hz*)	DF
	Q-control				**Q-control**			
FM	0.8098 *Hz*	0.3024	0.8101 *Hz*	0.3025	0.9705 *Hz*	0.3462	0.9834 *Hz*	0.3449
SM	0.8099 *Hz*	0.3026	0.8102 *Hz*	0.3017	0.9728 *Hz*	0.3459	0.9835 *Hz*	0.3438
	$\|\mathbf{V_{ac}}\|$-control				**$\|\mathbf{V_{ac}}\|$-control**			
FM	0.8092 *Hz*	0.3007	0.7922 *Hz*	0.3007	0.9769 *Hz*	0.3345	1.0077 *Hz*	0.3466
SM	0.8045 *Hz*	0.3017	0.8013 *Hz*	0.3013	0.9758 *Hz*	0.3342	0.9989 *Hz*	0.3464

power through the HVDC link employing FB - type Q-control with PI type frequency controller (FC) is presented in Figure 3.20(i). Similarly, the power through the link employing FB - type $|\mathrm{V_{ac}}|$ - control along with R type (droop type) frequency controller is given in Figure 3.20(ii). The performance of the system with the two models are overlapped and are presented.

Further, the average system frequency (refer section 2.3.1) denoted by *sysCOI* is studied under this condition of load trip. The *sysCOI* of both the areas with no frequency control (NFC) and with PI type frequency controller when the VSC-HVDC link is operating with FB-type, Q-control is presented in Figure 3.21. Due to load trip, as expected, sysCOI of the area-2 increases. Under frequency control, there is an increase in the average frequency of area-1 too. There is a negligible deviation in the *sysCOI* plots of the system with simplified model from that of full model.

3.5.2.3 16-machine, 68-bus system

In this section, a 16-machine, 68-bus system given in Figure 3.22 is used to further prove the effectiveness of the simplified model. The generator and network details of the system are adopted from (Pal and Chaudhuri, 2005). The system is per-unitised on a base of 100 MVA. Due to the large size of the system, only selected eigenvalues are considered. The dominant modes of the base system used in our study is given in Table 3.9.

Three VSC-HVDC links of different lengths are introduced in the system by replacing the existing transmission lines to conduct case studies. The DC links carry the same amount of power as that previously carried by the AC transmission lines. The details of the VSC-HVDC links are as follows (Rectifier - Converter-A, Inverter - Converter-B):

- Link-1 : A 400 km link between buses 41 and 40 to carry 6.2378 pu of power from

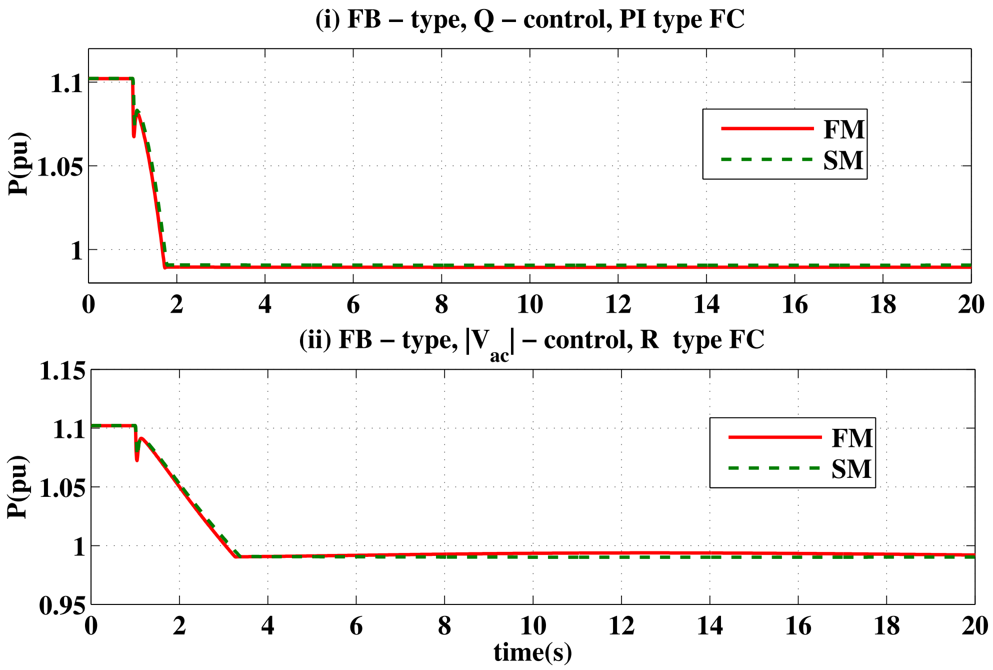

Figure 3.20: Power through VSC-HVDC link for load trip in asynchronous VSC-HVDC system

Table 3.9: Dominant modes of 16-machine base system

	Eigenvalue	f (*Hz*)	DF
Mode-1	-0.1212 ± j2.4817	0.3949 *Hz*	0.0487
Mode-2	-0.0835 ± j3.0928	0.4922 *Hz*	0.0269
Mode-3	-0.1911 ± j4.9266	0.7841 *Hz*	0.0387

bus 41 to bus 40.

- Link-2 : A 200 km link between buses 2 and 1 to carry 0.8387 pu of power from bus 2 to bus 1.
- Link-3 : A 100 km link between buses 8 and 9 to carry 0.2004 pu of power from bus 8 to bus 9.

The modal analysis of the system is given in Table 3.10 using prony method. The attributes of the dominant modes of the AC system with simplified and full models of VSC-HVDC links operating with FB - type, Q - control and FB - type, $|V_{ac}|$ - control is

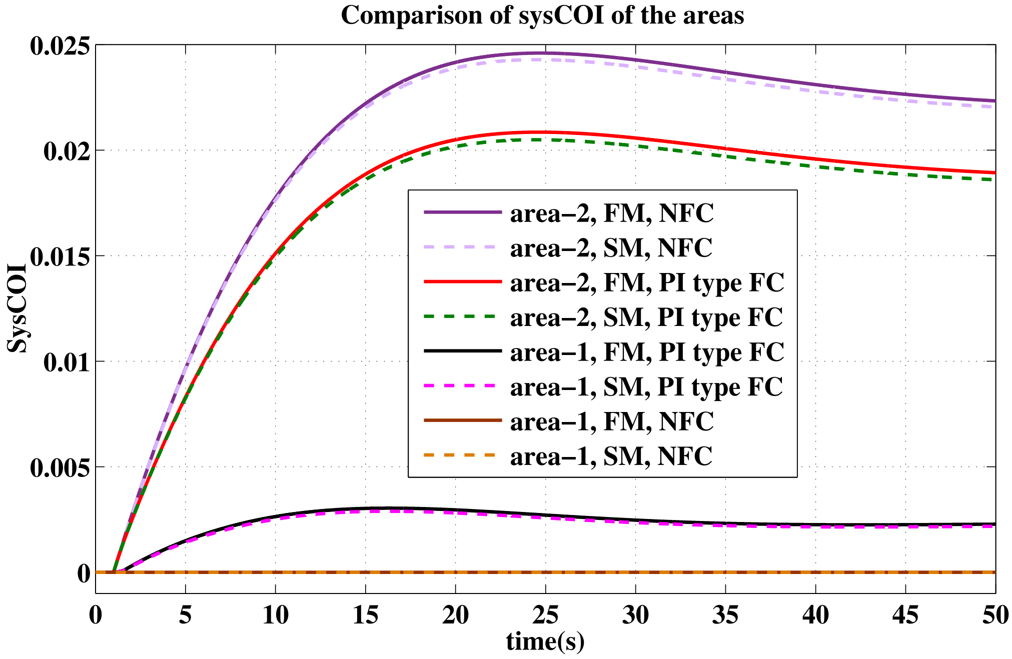

Figure 3.21: Comparison of sysCOI of areas for load trip in asynchronous VSC-HVDC system

presented. It can be observed that the mode features are similar for both the models. The analysis with FF - type controls provide similar results and are hence not presented here.

Table 3.10: Attributes of the Dominant modes of the 16-machine system with embedded VSC-HVDC links

Dominant Modes	Type of Model	Q - control, FB - type		$\lvert V_{ac}\rvert$ - control, FB - type	
		f (*Hz*)	DF	f (*Hz*)	DF
Mode-1	FM	0.3649 *Hz*	0.0054	0.3599 *Hz*	0.0195
	SM	0.3630 *Hz*	0.0051	0.3581 *Hz*	0.0163
Mode-2	FM	0.4883 *Hz*	0.0277	0.4812 *Hz*	0.0317
	SM	0.4981 *Hz*	0.0289	0.4971 *Hz*	0.0291
Mode-3	FM	0.7705 *Hz*	0.0372	0.7731 *Hz*	0.0352
	SM	0.7757 *Hz*	0.0379	0.7661 *Hz*	0.0357

A large and severe 3-phase to ground fault is applied at 1s on bus-48 of the system with VSC-HVDC links operating with FB - type $\lvert V_{ac}\rvert$ - control. Upon fault clearance after 3 cycles, one of the lines between buses 48 and 47 is tripped. For the event, computing times are measured for a 10 s simulation period. The simulations were run on a personal computer with a 3.60 GHz Intel Core i7-7700 processor and 16GB of RAM. The system

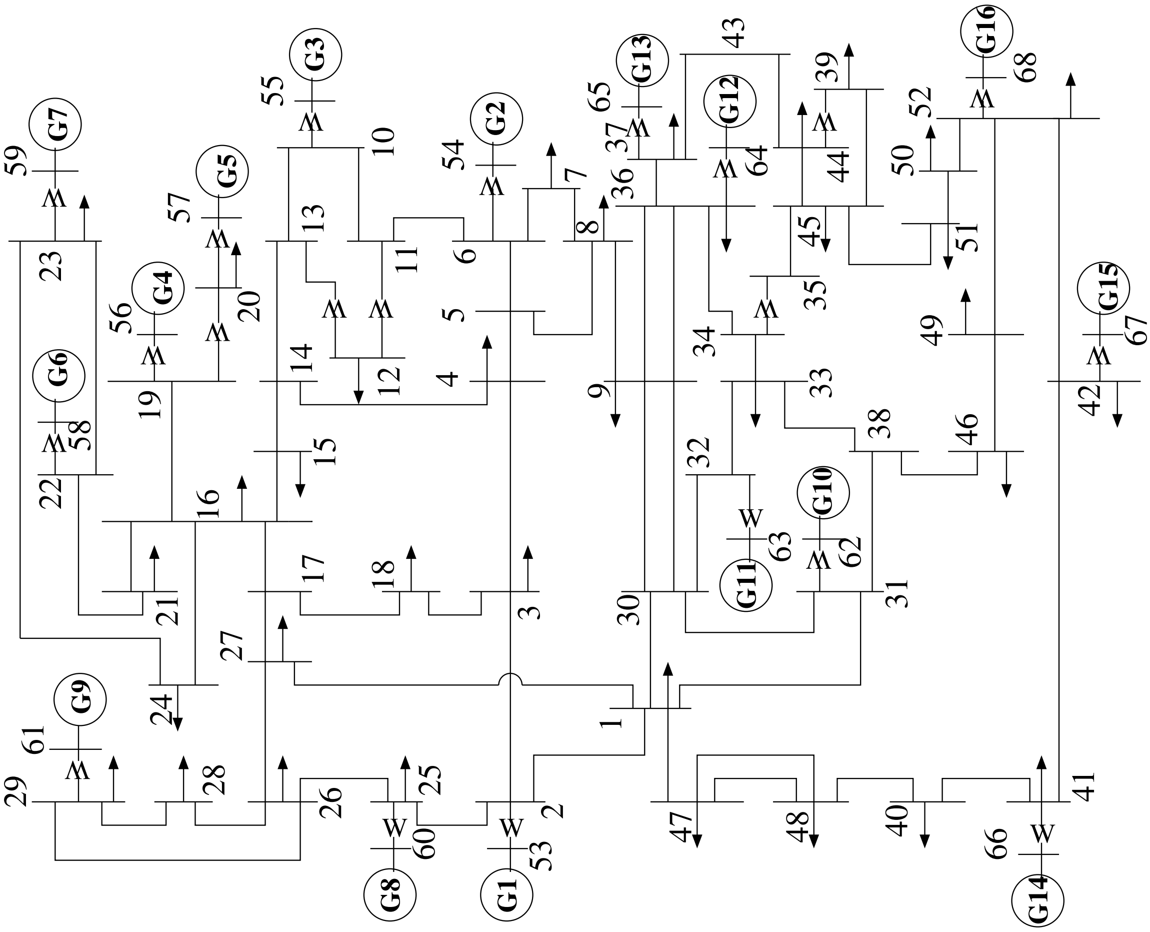

Figure 3.22: 16-machine, 68-bus base system

with full model of VSC-HVDC required a minimum time step of 10μs. Larger time steps displayed erroneous results. However, the system with simplified model provided accurate results even with 100μs step time. The CPU time taken is provided in Table 3.11. It can be observed that for a given time step of 10μs, the system with simplified model exhibits much lower computation time as compared to system with full model. With a time step of 100μs, excellent computation speed can be observed with usage of simplified VSC-HVDC model in the system.

The dynamic response of the system under this event is presented through plots given in Figure 3.23 and Figure 3.24. The PCC bus voltage magnitudes of the inverter of the three links, *i.e.* bus-40, bus-1 and bus-9 are presented in Figure 3.23. The bus-48 voltage magnitude and power in the un-tripped line between bus-48 and bus-47 is presented in

Table 3.11: CPU time taken for a simulation time of 10 seconds

Type	Full Model	Simplified Model	
Step time	10μs	10μs	100μs
CPU time	1264 s	772 s	84 s

Figure 3.24. In-spite of the severity of the fault, it can be observed that the system with simplified model is able to quickly respond to the event and provide support similar to the system with full model. This proves the efficacy of the simplified model in the analysis of multi-machine systems embedded with VSC-HVDC links even under adverse events.

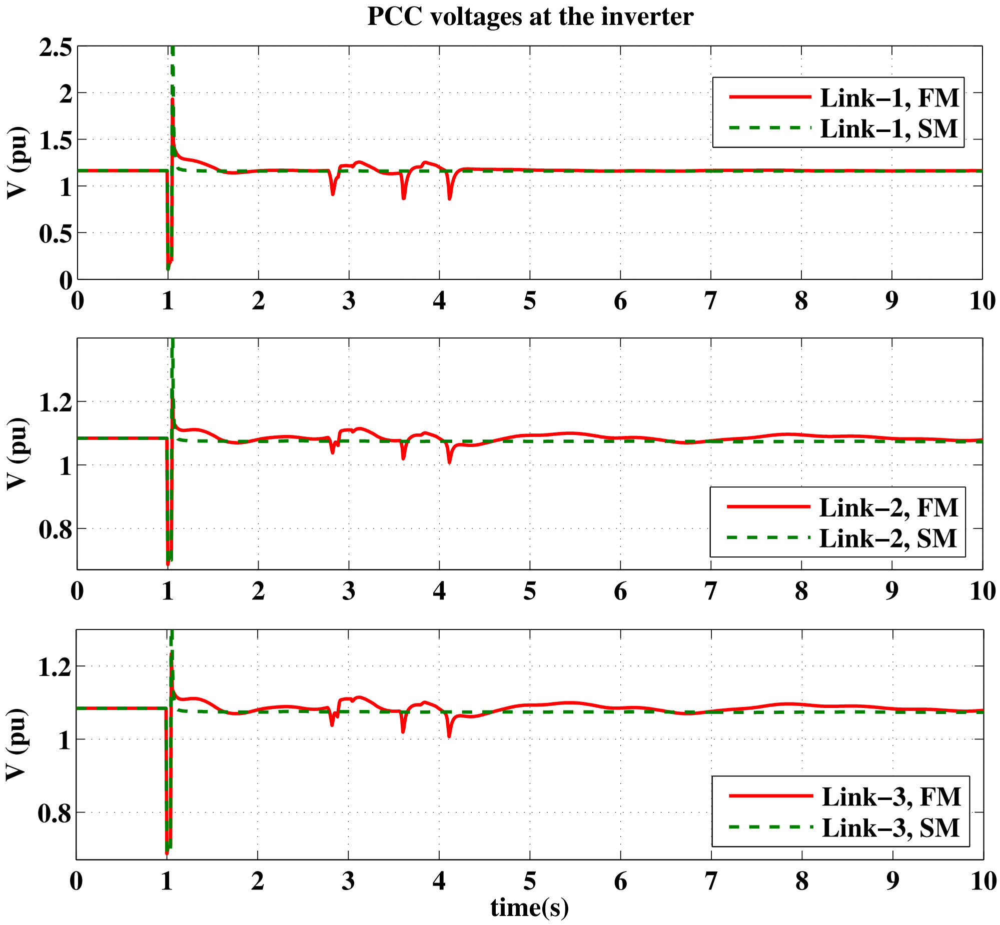

Figure 3.23: PCC voltages of the inverter of the three links (bus - 40, bus - 1 and bus - 9) of 16-machine, 68-bus system

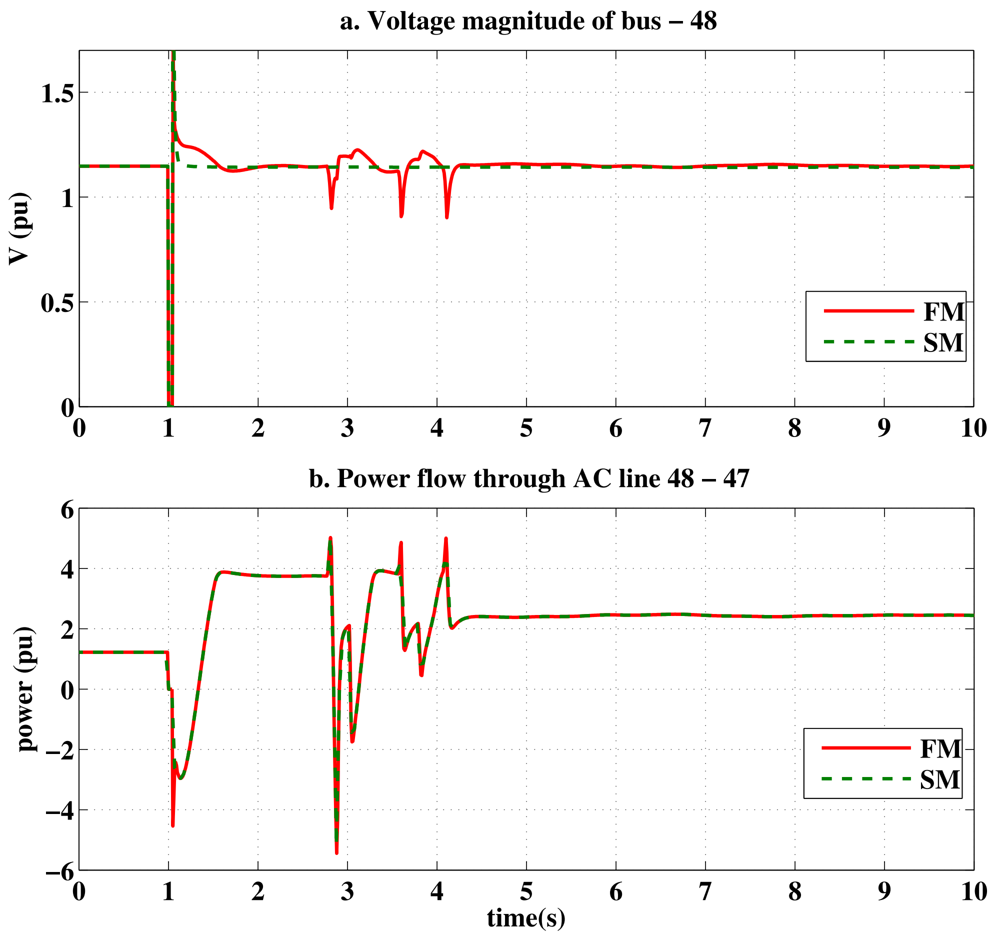

Figure 3.24: Bus-48 voltage magnitude and power in the line between buses 48 and 47 of 16-machine, 68-bus system

3.6 Summary

This chapter explores the modelling, control, and integration of VSC-HVDC links into multi-machine systems. Studies carried out and observations made in this chapter are given below:

- The effect of VSC-HVDC outer real and reactive controls on the behaviours of frequency controllers is analyzed. Simulations are performed on an asynchronous system with the inverter controlling the active power.

- It was observed that the performance of frequency controllers with feedback real power controller of lowest bandwidth was more robust for an event that solely affects the real power in the system. However, it was shown that frequency controllers along with feedforward active power controllers performed better during the initial transients for a system event that affected both real and reactive power.
- The influence on the type of reactive power controllers on the behaviour of frequency controllers is also presented. The difference was prominent for systems events affecting both real and reactive power. After the initial high frequency transients settled, larger low frequency oscillations were observed with frequency controllers added to feedforward active power control when AC voltage control was used for reactive power control.
- A simplified model of a VSC-HVDC link has been presented. The distinctive features of this model are the elimination of DC part dynamics, the inclusion of converter associated impedances as part of the AC system transmission network, and modification of the control system to control the converter related AC quantities. It allows for the direct determination of converter currents, making it a very simple model.
- Case studies are conducted for VSC-HVDC links embedded in 4-machine and 16-machine systems to validate the model. The model effectively captured the impact of different types of controllers, varying power levels in the links and influence of multiple VSC links in the system. It was also effective in providing frequency support in asynchronous system.
- The system with the simplified model exhibited significantly lower CPU time for simulation when compared to that with a full model.

In summary, this chapter has offered a comprehensive understanding of VSC-HVDC links, covering their modelling and control strategies. Building upon this foundational knowledge, the upcoming chapter will shift its focus to the pivotal role of VSC-HVDC links in the context of offshore wind farms. Due to its advanced control capabilities, VSC-HVDC remains the most attractive and cost-effective choice for integrating offshore wind farms into the grid. The next chapter will explore into the integration of VSC-HVDC based offshore wind farms into multi-machine systems, focusing on the dynamic modelling, power flow, and initial condition techniques of the system.

Chapter 4

VSC-HVDC CONNECTED OFFSHORE WIND FARMS

4.1 Introduction

Concerns about the depletion of fossil fuel resources and the increasing demand for sustainable power has made renewable energy systems very relevant today. Wind energy conversion systems, in particular, has grown rapidly over the last decade as a result of excellent technological developments and lower costs. Moreover, offshore wind farms are becoming increasingly popular due to abundant wind resources at sea, lower acoustic impact and the provision to deploy turbines with bigger capacities and sizes. Type-4 WECS with permanent magnet synchronous generators is a common choice in offshore systems. VSC-HVDC links are considered as the most economical choice to deliver power from the offshore wind farms. In the last chapter, a thorough analysis on the modelling and control interactions of VSC-HVDC links has been established.

As more VSC based renewable energy sources are connected to the grid, it becomes crucial to study the dynamics of the integrated power system. However, for studies focusing on the dynamic aspects and control of these systems, extensive methodologies for power flow and initial condition calculations may not be necessary. In such cases, researchers often turn to electromagnetic transient packages to avoid these calculations. Hence, in this chapter, a novel approach to the power flow and initial condition calculations of the VSC-HVDC connected DD-PMSG based wind farms integrated to multi-machine systems is proposed which would be required to aid its dynamic analysis. Effective methods have been described for most typically provided specified quantities of the wind farm. The approach allows the user to build the dynamic model in any basic dynamic modeller without the requirement of electromagnetic transient packages.

4.2 System description

An offshore wind farm consisting of N_{WT} variable speed WECS equipped with DD-PMSG is interfaced to a multi-machine system through a VSC-HVDC link. A single line diagram of the system is given in Figure 4.1.

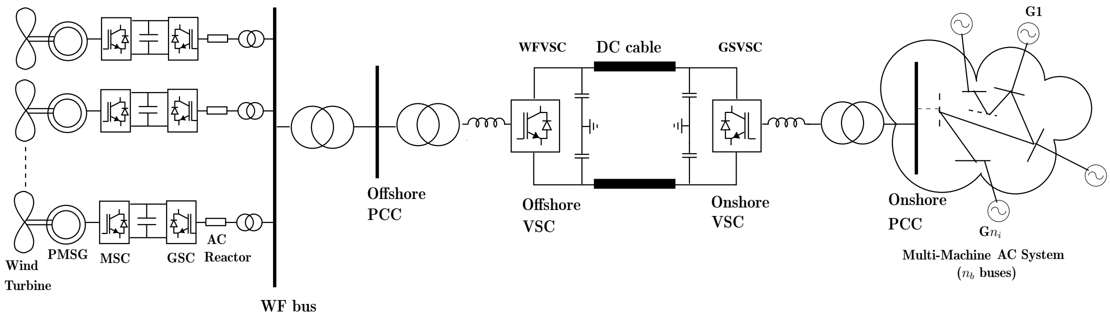

Figure 4.1: VSC-HVDC connected DD-PMSG offshore wind farm interfaced to multi-machine system

Individual wind turbine comprises of full scale back to back VSC's, decoupling PMSG from the rest of the system. Machine side converter (MSC) connects to the stator windings of the PMSG. The other converter, grid side converter (GSC), connects to the wind farm bus (WF bus) via a line reactor, filter and transformer. The wind farm's power is first transferred to the offshore AC network. The offshore network is passive in nature. The offshore VSC connects to the offshore network and is responsible in maintaining the voltage and frequency of the offshore PCC constant. The VSC-HVDC link transmits the power to the multi-machine system. The VSC associated with onshore PCC is referred as onshore VSC or grid side VSC (GSVSC) and the VSC associated with offshore converter is referred as offshore VSC or wind farm side VSC (WFVSC).

In this study, an aggregated model of wind farm is used. Individual wind turbine's mechanical and electrical attributes are scaled properly to be replaced by an equivalent wind turbine in the aggregated representation of the wind farm (Ali et al., 2011). All wind turbines in the wind farm are assumed to receive the same wind speed. This method would be appropriate for this study as the wind speed remains mostly constant in offshore conditions. Using this method for modelling, the order of the wind farm and computation time gets greatly reduced.

The machine reference frame (dq frame) is used to build the dynamic model of the PMSG of the wind farm and the synchronous generators of the multi-machine system. The synchronous reference frame (DQ frame) is used to model the remainder of the network. Per-unitisation is applied to all parameters and quantities.

4.3 Dynamic model of the system

In this section, an overview of the dynamic modelling of the system is described to assist the understanding of the proposed power flow and initial condition methodologies.

4.3.1 Dynamic model of the DD-PMSG offshore wind farm

4.3.1.1 Aggregated model of wind farm

Consider a single unit wind turbine. Let P_{mact} be the mechanical output and P_{WF} be the output at WF bus of each wind turbine. Let R_{sact}, x_{dact}, x_{qact}, $\psi_{f\,act}$ and J be the PMSG stator resistance, d-axis reactance, q-axis reactance, stator flux linkage and moment of inertia respectively in actuals. C_{dcact} is the DC link capacitance. R_{act} and X_{act} be the GSC side resistance and reactance respectively. Similar N_{WT} wind turbines constitute a wind farm.

In order to aggregate, the radially connected N_{WT} wind turbines are replaced by a single unit. The equivalent mechanical output of wind turbine is $N_{\mathrm{WT}}P_{mact}$ and equivalent output at wind farm bus is $N_{\mathrm{WT}}P_{\mathrm{WF}}$. Due to radial connection, the voltages and speed quantities remain the same in the aggregated model. Hence flux linkage of the equivalent wind turbine is the same as that of individual wind turbine. Equivalent current quantities are N_{WT} times the individual currents. The other parameters are scaled as :

$$\frac{R_{sact}}{N_{\mathrm{WT}}}, \frac{x_{dact}}{N_{\mathrm{WT}}}, \frac{x_{qact}}{N_{\mathrm{WT}}}, N_{\mathrm{WT}}J, N_{\mathrm{WT}}C_{dcact}, \frac{R_{act}}{N_{\mathrm{WT}}}, \frac{X_{act}}{N_{\mathrm{WT}}}$$

Per unitisation has been carried out on the following base: S_{sys} MVA (multi-machine system MVA rating, power base for entire system), V_{mb} V (voltage base on PMSG side of the transformer), ω_{rB} rad/s (PMSG frequency base), ω_{gB} rad/s (network frequency base).

In case the parameters are already given in per unit for a single wind turbine connected to a grid then following steps are adopted. Let R_{smb}, x_{dmb}, $x_{q_{mb}}$, ψ_F, C_{dcmb}, H_{mb} be the parameters of a single wind turbine in per-unit on individual machine base S_{mb} MVA and V_{mb} V.

Upon aggregation, the base is S_T = $N_{\mathrm{WT}}S_{mb}$ MVA whereas the voltage and frequency bases remain the same. The stator flux linkage in per-unit on the aggregated base remains to be ψ_F. The stator resistance in per-unit can be calculated as follows.

$$R_{saggr} = \frac{\frac{R_{smb}\frac{V^2{}_{mb}}{S_{mb}}}{N_{\mathrm{WT}}}}{\frac{V^2{}_{mb}}{S_T}} = R_{smb} \tag{4.1}$$

Similar calculations are done for the other parameters and quantities. It is understood that the per unit values of the aggregated wind farm on the aggregated base is equal to the per unit values of individual wind turbines on its own machine base.

All the per-unit values are transferred to multi-machine system base S_{sys} MVA. The voltage base and base rotational speed remain the same. The stator flux linkage ψ_F remains the same. The other parameters are calculated as follows. The stator resistance, reactances and inertia of PMSG are given as

$$R_s = R_{smb}\frac{S_{sys}}{S_T}, \;\; x_{sd} = x_{dmb}\frac{S_{sys}}{S_T}, \;\; x_{sq} = x_{q_{mb}}\frac{S_{sys}}{S_T}$$
$$H_s = H_{mb}\frac{S_T}{S_{sys}}$$

The DC link capacitance on the new base is,

$$(C_{dc})_{\mathrm{WF}} = C_{dcmb}\frac{S_T}{S_{sys}}$$

The GSC parameters are,

$$R_{\mathrm{GSC}} = R_{mb}\frac{S_{sys}}{S_T}, \;\; X_{\mathrm{GSC}} = X_{mb}\frac{S_{sys}}{S_T}$$

4.3.1.2 Wind turbine model

The mechanical power output of a wind turbine in watts, $P_{m_{act}}$ is given as,

$$P_{m_{act}} = \frac{1}{2}\rho A_{\mathrm{WT}} C_p V_{\mathrm{w}}^3 \tag{4.2}$$

where ρ is air density in kg/m^3, V_{w} is wind velocity in m/s and A_{WT} is the surface area of blades in m^2. C_p is the performance coefficient which is the function of tip speed ratio, λ given as,

$$C_p = c_1(\frac{c_2}{\lambda_i} - c_3\beta - c_4)e^{\frac{-c_5}{\lambda_i}} + c_6\lambda \tag{4.3}$$

where c_1 to c_6 are the wind turbine coefficients and λ_i is given as,

$$\frac{1}{\lambda_i} = \frac{1}{\lambda + 0.08\beta} - \frac{0.035}{\beta^3 + 1} \tag{4.4}$$

where β is the blade pitch angle. The tip speed ratio is defined as,

$$\lambda = \frac{\omega_{rm} R_{\mathrm{WT}}}{V_{\mathrm{w}}} \tag{4.5}$$

where ω_{rm} is the speed of the rotor of wind turbine in rad/s (mechanical). The maximum power coefficient occurs at the optimal tip speed ratio with the optimal pitch angle. For a given blade the optimal tip speed ratio is a constant. For N_{WT} wind turbines, the mechanical power output in per-unit can be obtained as

$$P_m = \frac{N_{\mathrm{WT}} P_{m_{act}}}{S_{sys}} \tag{4.6}$$

The per-unit mechanical torque output which drives the PMSG is given as,

$$T_m = \frac{P_m}{\omega_r} \tag{4.7}$$

ω_r is the per-unit rotor speed.

<u>Note</u>: ω_r is calculated as $\omega_r = \frac{\omega_{rm}}{\omega_{rmB}} = \frac{\omega_{re}}{\omega_{rB}}$ where ω_{rm} is the rotor speed in mechanical rad/s , ω_{rmB} is the base rotor speed in mechanical rad/s , ω_{re} is the rotor speed in electrical rad/s, ω_{rB} is the base rotor speed in electrical rad/s.

4.3.1.3 PMSG modelling

The modelling equations of a synchronous machine is already elaborated in (Padiyar K.R., 2002). The modelling of a permanent magnet synchronous machine can be done in similar way (Chia-Nan et al., 2014). As rotor coils donot exist in a PMSG, only stator currents need to be modelled. The per-unit equations of the PMSG dynamic model in the rotor reference frame is given here.

The stator current components, i_{sq} and i_{sd} are modelled as,

$$\begin{aligned}\frac{di_{sq}}{dt} &= \frac{-\omega_{rB}}{x_{sq}}(R_s i_{sq} - \omega_r \psi_{sd} + v_{sq}) \\ \frac{di_{sd}}{dt} &= \frac{-\omega_{rB}}{x_{sd}}(R_s i_{sd} + \omega_r \psi_{sq} + v_{sd})\end{aligned} \tag{4.8}$$

where,

$$\psi_{sq} = x_{sq} i_{sq} \text{ and } \psi_{sd} = x_{sd} i_{sd} + \psi_F$$

R_s, x_{sq} and x_{sd} are the PMSG stator resistance, q-axis reactance and d-axis reactance respectively. The stator voltages v_{sq} and v_{sd} are obtained as output from the controller of machine side converter (MSC).
The mechanical equation is,

$$2H_s \frac{d\omega_r}{dt} = T_m - T_{eg} \tag{4.9}$$

where the electromagnetic torque T_{eg} is given as,

$$T_{eg} = \psi_{sd} i_{sq} - \psi_{sq} i_{sd} \tag{4.10}$$

The power output at the PMSG is calculated as,

$$P_s = v_{sq} i_{sq} + v_{sd} i_{sd} \tag{4.11}$$

4.3.1.4 Machine side converter

At wind speeds above cut-in and below rated, machine side converter controls the PMSG to ensure maximum power point (MPP) operation. Cascaded control structure with outer MPP controller and inner current controller is used.

An optimal tip speed ratio is maintained in order to obtain maximum power at any wind speed. Accordingly, the optimal speed or torque reference is determined. The outer control loop of the MSC handles this MPP operation. Also, maximum torque is maintained with minimum stator current by setting d-axis current to zero. It is also required to protect the converter from over currents. The fast inner current control loop controls the d and q axes currents of the PMSG.

Let λ_{opt} be the optimal tip speed ratio which is maintained constant. At this tip speed ratio, the performance coefficient is $C_{p_{opt}}$ for an optimum blade pitch angle β. For a given wind speed, the optimal rotor speed can be obtained from (4.5). For a given wind speed V_{W},

$$\omega_{rm} = \lambda_{opt} \frac{V_{\mathrm{W}}}{R_{WT}} \tag{4.12}$$

In this study, MPPT with optimal torque control method is used. Zero d-axis control is adopted. The desired torque reference is obtained using the optimum speed.
From (4.6),

$$\begin{aligned} P_m^* &= \frac{N_{\mathrm{WT}}(\frac{1}{2}\rho A_{\mathrm{WT}} C_{p_{opt}} V_{\mathrm{W}}^3)}{S_{sys}} \\ &= \frac{N_{\mathrm{WT}}\frac{1}{2}\rho A_{\mathrm{WT}} C_{p_{opt}} (\frac{\omega_{rm}^3 R_{\mathrm{WT}}^3}{\lambda_{opt}^3})}{S_{sys}} \\ &= \frac{N_{\mathrm{WT}}\frac{1}{2}\rho A_{\mathrm{WT}} C_{p_{opt}} \frac{\omega_{rm}^3 R_{\mathrm{WT}}^3}{\lambda_{opt}^3} (\frac{\omega_{rmB}^3}{\omega_{rmB}^3})}{S_{sys}} \\ P_m^* &= K_{opt}\,\omega_r^3 \end{aligned} \tag{4.13}$$

where

$$K_{opt} = \frac{N_{\mathrm{WT}}\frac{1}{2}\rho A_{\mathrm{WT}} C_{p_{opt}} R_{\mathrm{WT}}^3 \omega_{rmB}^3}{S_{sys}\lambda_{opt}^3} \tag{4.14}$$

From (4.7),

$$T_m^* = K_{opt}\,\omega_r^2 \tag{4.15}$$

As zero d-axis current control strategy is used, the q-axis reference current is obtained from (4.10) as,

$$i_{sq}^* = \frac{T_m^*}{\psi_F} \tag{4.16}$$

The reference inputs for the inner current controller are i_{sq}^* and $i_{sd}^* = 0$. The inner current control structure is similar to that discussed in chapter 3. The entire control scheme is given in Figure 4.2. In the figure, $v_{sq_{in}}$ and v_{sdin} are the intermediate state variables obtained from inner current PI controllers whose constants are K_{psq}, K_{isq}, K_{psd} and K_{isd}. The back to back DC link is modelled in the conventional manner.

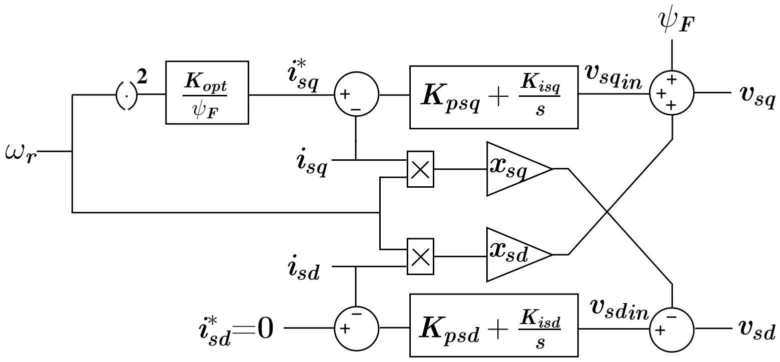

Figure 4.2: MSC control system

4.3.1.5 Grid side converter model

The GSC controls the DC link voltage of the wind farm and the reactive power exchanged with the WF bus. The vector control strategy is used. A slow outer loop manages the DC voltage and reactive power control whereas a fast inner loop does the current control.

In order to achieve decoupled control, the converter model is derived in dq frame, where the instantaneous voltage at the wind farm bus is assumed to be always aligned towards the q-axis and d-axis is quadrature to it. The converter model in dq frame is given as,

$$\begin{aligned}\frac{di_{qOFF}}{dt} &= \frac{\omega_{gB}}{X_{\mathrm{GSC}}}[v_{qGSC} - R_{\mathrm{GSC}}i_{qOFF} + \frac{\omega_g}{\omega_{gB}}X_{\mathrm{GSC}}i_{dOFF} - V_{qWF}] \\ \frac{di_{dOFF}}{dt} &= \frac{\omega_{gB}}{X_{\mathrm{GSC}}}[v_{dGSC} - R_{\mathrm{GSC}}i_{dOFF} - \frac{\omega_g}{\omega_{gB}}X_{\mathrm{GSC}}i_{qOFF}]\end{aligned} \tag{4.17}$$

where R_{GSC} and X_{GSC} is the GSC side resistance and reactance respectively, $v_{qGSC}+jv_{dGSC}$ is the GSC converter bus voltage and $v_{qWF}+jv_{dWF}$ is the wind farm bus voltage.

The modelling and control of GSC is similar to that discussed for VSC in Chapter 3. The currents obtained in dq frame in the GSC controller is transformed back to the DQ frame in order to be compatible with the offshore network model. Current injection model of the converter is adopted.

4.3.2 Dynamic model of VSC-HVDC

The offshore PCC is controlled in such a way as to behave like an infinite grid since the offshore network is passive. The offshore VSC is in charge of transferring the wind farm's power as well as keeping the voltage magnitude and frequency of the offshore PCC constant.

Consider that $e_{Q_{\text{OFF}}} + je_{D_{\text{OFF}}}$ is the voltage at the offshore PCC. The control requires that the magnitude of the voltage *i.e.* $\sqrt{e^2_{Q_{\text{OFF}}} + e^2_{D_{\text{OFF}}}}$ is a constant. In the synchronous rotating frame, constant frequency at the offshore bus can be obtained by controlling the frequency deviation (rate of change of bus angle) at the bus to zero. The frequency deviation in rad/s is given as,

$$\begin{aligned}\frac{d\theta_{\text{OFF}}}{dt} &= \frac{d}{dt}(tan^{-1}\frac{e_{D_{\text{OFF}}}}{e_{Q_{\text{OFF}}}}) \\ &= \frac{e_{Q_{\text{OFF}}}\frac{de_{D_{\text{OFF}}}}{dt} - e_{D_{\text{OFF}}}\frac{de_{Q_{\text{OFF}}}}{dt}}{e^2_{Q_{\text{OFF}}} + e^2_{D_{\text{OFF}}}}\end{aligned} \tag{4.18}$$

Thus, by maintaining each component of the voltage constant, both the control requirements can be satisfied.

As the current in the offshore network is known, the converter AC side voltage equation can be described as,

$$\begin{aligned}e_{Q_{\text{OFF}}} + je_{D_{\text{OFF}}} = v_{Q_{\text{OFF}}} + jv_{D_{\text{OFF}}} + \\ (i_{Q_{\text{OFF}}} + ji_{D_{\text{OFF}}})(R_R + jX_R)\end{aligned} \tag{4.19}$$

where $v_{Q_{\text{OFF}}}$ + j $v_{D_{\text{OFF}}}$ is the offshore VSC converter side voltage and R_R, X_R are the reactances associated with offshore VSC.

The individual components of the offshore voltage can be given as,

$$\begin{aligned}e_{Q_{\text{OFF}}} &= v_{Q_{\text{OFF}}} + i_{Q_{\text{OFF}}}R_R - i_{D_{\text{OFF}}}X_R \\ e_{D_{\text{OFF}}} &= v_{D_{\text{OFF}}} + i_{D_{\text{OFF}}}R_R + i_{Q_{\text{OFF}}}X_R\end{aligned} \tag{4.20}$$

From the equations, it can be seen that the converter AC voltages $v_{Q_{\text{OFF}}}$ and $v_{D_{\text{OFF}}}$ can be used for the control. It can be also seen that cross coupling terms exist and hence to achieve decoupled control, feedforward terms are introduced. The control voltage loop can be expressed as,

$$\begin{aligned} v_{Q_{\mathrm{OFF}}} &= \left((K_p)_{eQ} + \frac{(K_i)_{eQ}}{s}\right)(e^*_{Q_{\mathrm{OFF}}} - e_{Q_{\mathrm{OFF}}}) + i_{D_{\mathrm{OFF}}} X_R \\ v_{D_{\mathrm{OFF}}} &= \left((K_p)_{eD} + \frac{(K_i)_{eD}}{s}\right)(e^*_{D_{\mathrm{OFF}}} - e_{D_{\mathrm{OFF}}}) - i_{Q_{\mathrm{OFF}}} X_R \end{aligned} \tag{4.21}$$

where $(K_p)_{eQ}$, $(K_i)_{eQ}$, $(K_p)_{eD}$ and $(K_i)_{eD}$ are the PI constants.

The onshore VSC controls the DC link voltage $(v_{dc})_{\mathrm{ON}}$ of the VSC-HVDC link and maintains reactive power at the onshore PCC to zero. The modelling of the DC link and onshore converter of the VSC-HVDC is similar to that discussed in Chapter 3.

4.3.3 Interfacing to the AC network

The entire VSC-HVDC connected PMSG wind farm is interfaced to the multi-machine system at the onshore PCC. The modelling of onshore converter is done in the *dq* frame. The currents in the *dq* frame are transferred back to the *DQ* frame and treated as current injections $\bar{I}_{DQ_{ON}}$ at onshore PCC for the interface. Further, vectorisation is done in order to include any number of VSC-HVDC connected wind farms in the multi-machine system. The procedure is described in Chapter 3. The vectorised currents are,

$$\underline{\bar{I}}_{\mathrm{PCC}} = \begin{cases} \bar{I}_{DQ_{ON}} & : \text{At onshore PCC buses} \\ 0 & : \text{At other buses} \end{cases}$$

The bus voltages of the network of multi-machine system are calculated as :

$$\underline{\bar{E}}_{DQ} = (\underline{\bar{I}}_{Gs} - \underline{\bar{I}}_{Ls} - \underline{\bar{I}}_{PCC})/Y_{BUS} \tag{4.22}$$

where, $\underline{\bar{E}}_{DQ}$ is the bus voltage vector, $\underline{\bar{I}}_{Gs}$ is the vector of generator source currents, $\underline{\bar{I}}_{Ls}$ is the load current vector and Y_{BUS} is the admittance matrix of the system.

4.4 Power flow and initial condition calculations

The steady state equivalent circuit of the system is given in Figure 4.3. R_{OFF} and X_{OFF} are the offshore network resistance and reactance. Each of the VSC's of the VSC-HVDC link are connected to their respective PCC's via a reactor and coupling transformer. R_{R} and

X_{R} are the resistance and reactance relating to the offshore VSC while R_{I} and X_{I} are those pertaining to onshore VSC.

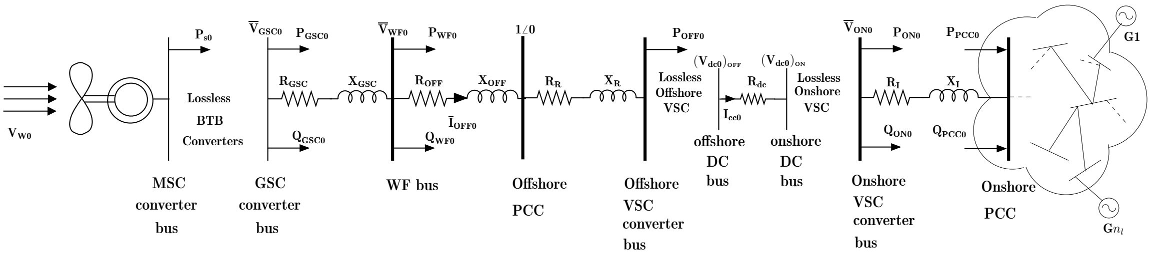

Figure 4.3: Equivalent circuit for initial condition calculations

The known quantities of the system are as follows,

- The reactive power at the the wind farm bus, $Q_{\mathrm{WF0}} = 0$ pu.
- The voltage at the offshore PCC bus, $(\overline{V}_{\mathrm{OFF0}})_{\mathrm{PCC}} = 1\angle 0$ pu.
- The DC voltage of the onshore converter, $(V_{dc0})_{\mathrm{ON}}$.
- The reactive power at onshore PCC bus, $Q_{\mathrm{PCC0}} = 0$ pu.

Based on the given specifications of the offshore wind farm, the proposed method is subdivided into following three cases.

4.4.1 Case 1 : The total output of the wind farm (P_{WF0} pu) and the total number of wind turbines in the wind farm (N_{WT}) are known :

In this case, the procedure begins by calculating the offshore AC network's power flow. The obtained offshore current would be required to calculate the power flow and initial conditions of PMSG wind farm. In this case, even the initial wind speed has to be calculated and a method has been described for the same. The power at the offshore converter can be computed from the offshore AC network power flow, allowing the user to conduct the load flow of the DC section of the HVDC link. The real power at the onshore VSC converter bus is derived from this. The calculations for the onshore converter bus are incorporated in the load flow of the multi-machine system to simplify the procedure. The following is a detailed description of the entire method.

4.4.1.1 Power flow and initial conditions of offshore AC network

- The real power output at the wind farm bus is given and the reactive power is maintained at zero. Thus, the total power output at the wind farm bus is known *i.e.* $P_{\text{WF0}} + j0$. The offshore PCC bus voltage is held constant at $1\angle 0$.

- The equations governing the offshore network are :

$$\begin{aligned} \overline{I}_{\text{OFF0}} &= \frac{\overline{V}_{\text{WF}} - 1}{R_{\text{OFF}} + jX_{\text{OFF}}} \\ P_{\text{WF0}} + j0 &= \overline{V}_{\text{WF0}} \overline{I}^{*}_{\text{OFF0}} \end{aligned} \tag{4.23}$$

- Solving the above equations, $\overline{V}_{\text{WF0}}$ and $\overline{I}_{\text{OFF0}}$ can be obtained.

- Through this, the real and reactive power flows at the offshore AC network buses can be calculated.

4.4.1.2 Power flow and initial conditions of the DC part of VSC-HVDC link

- Under steady state, the DC part of the HVDC link is reduced to a series resistor between the DC buses.

- The DC voltage of the onshore VSC is a constant at $(V_{dc0})_{\text{ON}}$.

- The power at the offshore VSC converter bus, P_{OFF0}, can be obtained as

$$P_{\text{OFF0}} = \text{real}\{(1 - [R_{\text{R}} + jX_{\text{R}}]\overline{I}_{\text{OFF0}})\overline{I}^{*}_{\text{OFF0}}\} \tag{4.24}$$

- The power at the offshore DC bus is P_{OFF0}.

- The equations governing the DC circuit are,

$$\begin{aligned} (V_{dc0})_{\text{OFF}} &= I_{\text{cc0}} R_{dc} + (V_{dc0})_{\text{ON}} \\ I_{\text{cc0}} &= \frac{P_{\text{OFF0}}}{(V_{dc0})_{\text{OFF}}} \end{aligned} \tag{4.25}$$

- From the above equations $(V_{dc0})_{\text{OFF}}$ and I_{cc0} can be obtained which are the initial conditions for the DC link model.

- The real power at onshore VSC converter bus is calculated as

$$P_{\mathrm{ON0}} = (V_{dc0})_{\mathrm{ON}} I_{\mathrm{cc0}} \tag{4.26}$$

- However, the calculation of reactive power at the onshore VSC converter bus is not straightforward. Hence, an algorithm is proposed, where the onshore VSC converter bus is included in the load flow of the multi-machine system. It is described in the following section.

4.4.1.3 Power flow and initial conditions of the multi-machine system

- The onshore VSC converter bus, reactor and coupling transformer are included in the load flow of the multi-machine system. Therefore, for a multi-machine system with n_b buses and n_l transmission lines, the load flow would contain $n_b + 1$ buses and $n_l + 1$ transmission lines.

- The reactive power at onshore PCC is maintained at zero. But, in order to avoid complex alterations to the existing load flow program, initially the reactive power at onshore VSC converter bus is considered to be zero.

- A simple iterative algorithm is adopted as follows. The onshore VSC converter bus is considered as a *PQ* bus (load bus) with real power $P = P_{\mathrm{ON0}}$. Initially, in the first iteration, the reactive power (Q) is taken to be zero *i.e.* $Q_1 = 0$. Load flow is performed for the modified multi-machine system. After the convergence, the reactive power at the onshore PCC bus, Q_{PCC0} is noted. For the next iteration, load flow is initialized by adding Q_{PCC0} to the existing reactive power at the onshore VSC converter bus *i.e.* $Q_2 = Q_1 + Q_{\mathrm{PCC0}}$. This process is repeated until reactive power requirement at the onshore PCC bus is zero, *i.e.*, $Q_{\mathrm{PCC0}} = 0$. This algorithm is written as an external loop to the main load flow program.

- Once the final load flow convergence is obtained, the reactive power at the onshore PCC is given as $Q_{\mathrm{ON0}} = -Q_l$ where Q_l is the reactive power noted at the onshore VSC converter bus for last iteration. The initial conditions of the multi-machine system are calculated as given in (Padiyar K.R., 2002).

4.4.1.4 Power flow and initial conditions of PMSG aggregated wind farm

- Using the system base values and N_{WT}, the parameters of the aggregated wind farm can be calculated.

- The initial conditions, I_{q0} and I_{d0} for (4.17) is given as,

$$I_{q0} + jI_{d0} = (\bar{I}_{\mathrm{OFF0}})e^{-j\theta_{\mathrm{WF0}}} \tag{4.27}$$

- The power at GSC bus can be calculated as

$$P_{\mathrm{GSC0}} = P_{\mathrm{WF0}} + (I_{q0}^2 + I_{d0}^2) * R_{GSC} \tag{4.28}$$

  Due to no loss back to back converter, this power equals the power output at PMSG.

$$P_{\mathrm{s0}} = P_{\mathrm{GSC0}} \tag{4.29}$$

- The controller of MSC is equipped with zero d axis current control *i.e.* $i_{sd0} = 0$. Hence, $i_{sq0} = \frac{T_{m0}}{\psi_F}$.

- The power output at PMSG can be written as :

$$\begin{aligned} P_{\mathrm{s0}} &= v_{sq0} i_{sq0} \\ &= (-R_s i_{sq0} + \omega_{r0}\psi_F) i_{sq0} \\ &= -R_s \frac{T_{m0}^2}{\psi_F^2} + \omega_{r0} T_{m0} \\ &= -R_s \frac{(K_{opt}^2 \omega_{r0}^4)}{\psi_F^2} + \omega_{r0}(K_{opt0}\omega_{r0}^2) \end{aligned} \tag{4.30}$$

- This equation can be written in terms of ω_{r0} as,

$$\frac{R_s K_{opt}^2}{\psi_F^2}\omega_{r0}^4 - K_{opt}\omega_{r0}^3 + P_{\mathrm{s0}} = 0 \tag{4.31}$$

  The required ω_{r0} is one of the solutions of the above equation. Upon analysis it can be found that only one pole can be between '0' and '1' which is the required solution to ω_{r0}. This value is the initial condition for (4.9).

- i_{sd0} and i_{sq0} are the initial conditions for (4.8).

- The initial wind speed can be calculated from (4.5) as,

$$V_{\mathrm{w0}} = \frac{\omega_{r0}\omega_{rmB}R_{\mathrm{WT}}}{\lambda_{opt}} \tag{4.32}$$

4.4.2 Case 2 - The output from each wind turbine and the total output of wind farm are given :

If the output from each wind turbine P_{wt0} pu on individual turbine base is known then the total number of wind turbines N_{WT} can be calculated as,

$$N_{\mathrm{WT}} = \frac{P_{\mathrm{wf0}} * S_{sys}}{P_{\mathrm{wt0}} * S_{mb}} \tag{4.33}$$

The value is rounded off to the next whole number. The rest of the calculations are obtained as per Case 1.

4.4.3 Case 3 - The initial wind speed and the total number of wind turbines in the wind farm are given :

In this case, the aggregated PMSG wind farm calculations are obtained first, followed by the offshore network, DC link and the multi-machine system. An iterative approach is proposed to acquire the real power output at the wind farm bus while keeping the reactive power at the bus at zero. The GSC bus is included in the power flow of offshore network for this algorithm. The complete description of the method is given below.

4.4.3.1 Power flow and initial conditions of PMSG aggregated wind farm

- The initial wind speed V_{w0} is the known quantity.

- The optimum rotor speed for the given wind speed is,

$$\omega_{r0} = \frac{\left(\frac{V_{\mathrm{w0}}\lambda_{opt}}{R_{\mathrm{WT}}}\right)}{\omega_{rmB}} \tag{4.34}$$

- The torque can be calculated as,

$$T_{m0} = K_{opt}\omega_{r0}^2 \tag{4.35}$$

Hence, the q-axis reference current can be obtained as,

$$i_{sq0} = \frac{T_{m0}}{\psi_F} \tag{4.36}$$

- The initial power at MSC bus is given as,

$$P_{s0} = v_{sq0}i_{sq0} \tag{4.37}$$

where v_{sq0} can be obtained as,

$$v_{sq0} = -R_s i_{sq0} + \omega_{r0}\psi_F \tag{4.38}$$

- The real power at GSC bus is,

$$P_{\mathrm{GSC0}} = P_{\mathrm{s0}} \tag{4.39}$$

- The real power at the wind farm bus cannot be obtained in a straightforward manner as the current is unknown. Hence the calculations of power flow at wind farm bus is included with that of offshore grid calculations.

4.4.3.2 Power flow and initial conditions of offshore network

- The real power at the GSC bus, the reactive power at the wind farm bus and the voltage at the offshore PCC are the known quantities. As there are differences in data specified for the three different buses and in order to avoid complex calculations an efficient algorithm is developed.

- The reactive power at the GSC bus is initially taken to be zero. The voltage at GSC bus can be obtained. The offshore current $\bar{I}_{\mathrm{OFF0}}$ can be calculated. The reactive power at wind farm bus is calculated which is the power required by GSC reactor and is to be compensated by GSC converter. This reactive power is added to the GSC bus and the above calculations are again repeated. The process is repeated until the reactive power at wind farm bus is zero.

```
Initially $Q_{\mathrm{GSC}01} = 0$
Repeat following steps until $Q_{\mathrm{WF}0}$ equals zero
    Let k be the iteration counter
    Solve for $\overline{V}_{\mathrm{GSC}0k}$,
        $P_{\mathrm{GSC}0} + jQ_{\mathrm{GSC}0k} = \overline{V}_{\mathrm{GSC}0k}\left(\frac{\overline{V}_{\mathrm{GSC}0k} - 1}{R_{\mathrm{GSC}} + R_{\mathrm{OFF}} + j(X_{\mathrm{GSC}} + X_{\mathrm{OFF}})}\right)^*$    (4.40)
    Calculate,
        $\overline{I}_{\mathrm{OFF}0k} = \frac{\overline{V}_{\mathrm{GSC}0k} - 1}{R_{\mathrm{GSC}} + R_{\mathrm{OFF}} + j(X_{\mathrm{GSC}} + X_{\mathrm{OFF}})}$
        $\overline{V}_{\mathrm{WF}0k} = \overline{V}_{\mathrm{GSC}0k} - \overline{I}_{\mathrm{OFF}0k}(R_{\mathrm{GSC}} + jX_{\mathrm{GSC}})$
        $Q_{\mathrm{WF}0k} = Imag\{\overline{V}_{\mathrm{WF}0k}\overline{I}^*_{\mathrm{OFF}0k}\}$
        $Q_{\mathrm{GSC}0k} = Q_{\mathrm{GSC}0k-1} - Q_{\mathrm{WF}0k}$
```

- The power at the offshore converter $P_{\mathrm{OFF}0}$ is calculated.
- The rest of the load flow and initial conditions calculations of DC link and multi-machine system remain the same as that in Case-1.

As vectorisation is done the proposed method can be extended to a multi-machine system containing any number of VSC-HVDC connected DD-PMSG wind farms.

4.5 Case studies

For the validation of the proposed power flow and initial condition technique, two case studies have been taken up which are implemented in MATLAB.

4.5.1 Case study 1 : Two area, 4-machine system

The two-area, 4-machine system in Figure 2.7 is used for the study. The system is modified with a offshore wind farm connected to bus-9 (onshore PCC) of the system via a VSC-HVDC link as shown in the Figure 4.4. The parameters of the wind turbine and VSC-

HVDC link is given in the Appendix A2, A3.

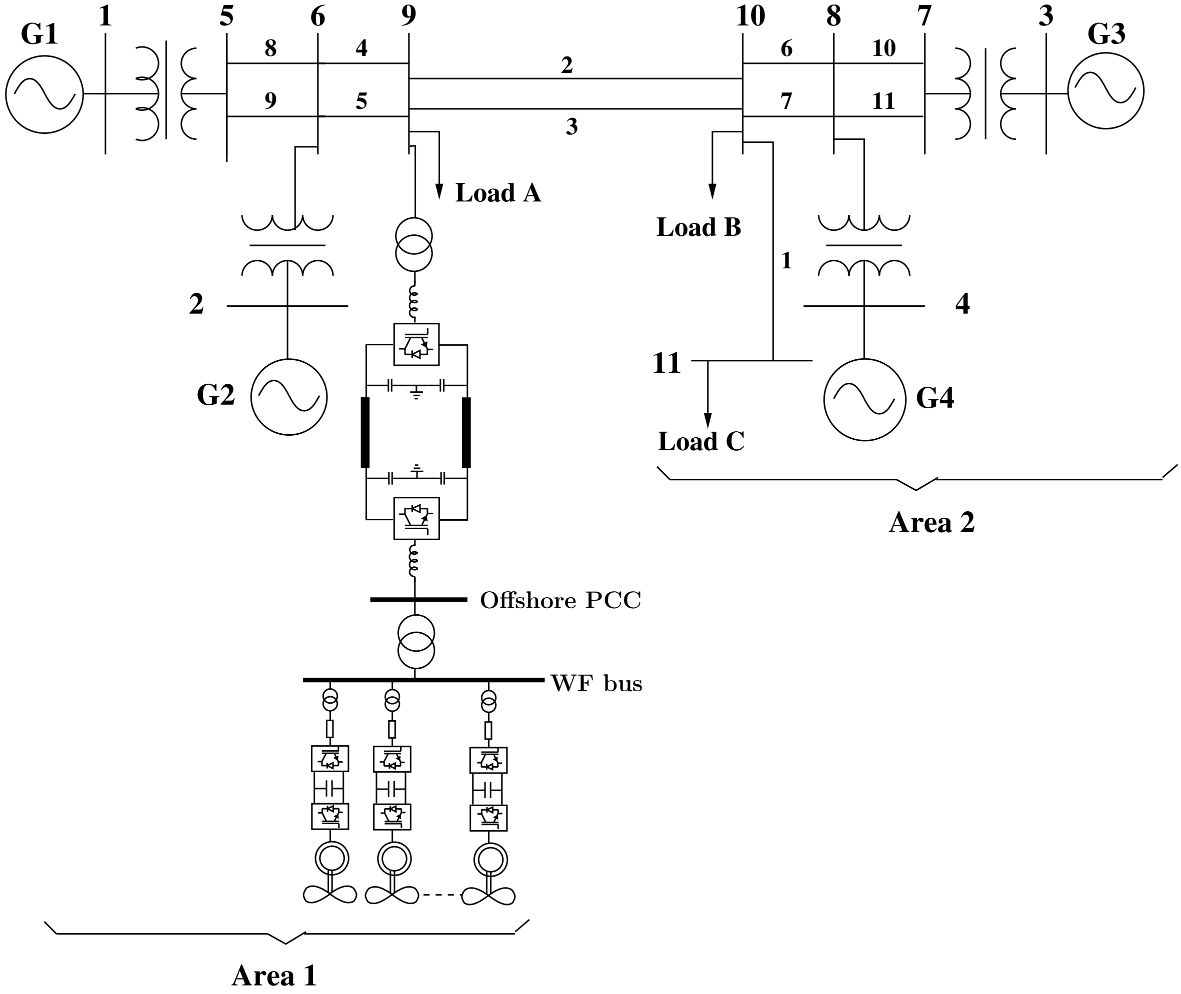

Figure 4.4: Two-area, 4-machine system with offshore wind farm

1. The wind farm is assumed to be injecting 0.2 pu of power at the wind farm bus and the total wind turbines in the wind farm is given as 18.

The study corresponds to case-1 of the proposed load flow and initial condition calculation method. The results are shown in Table 4.1. The specified quantities are provided in the first row, followed by the significant results of the proposed method. The offshore network results are provided first followed by DC network and multi-machine results. The complete load flow and initial condition data of the multi-machine system is not presented here as it is not the focus of method presented. The reactive power at onshore PCC is obtained as zero in two iterations. The aggregated parameters of the PMSG wind farm are determined using the parameters of a single wind turbine listed in Appendix A3. The offshore PMSG wind farm quantities are computed backwards from the wind farm bus quantities to finally obtain the wind speed.

Table 4.1: Load flow and initial condition calculations (Case-1)

Specified Quantities	P_{WF0} = 0.2 pu, Q_{WF0} = 0 pu, $(\overline{V}_{\text{OFF0}})_{\text{PCC}} = 1\angle 0$ $(V_{dc0})_{\text{ON}}$ = 1.5 pu, Q_{PCC0} = 0 pu N_{WT} = 18, i_{sd0} = 0 pu		
Load flow and Initial condition calculations			
Offshore Grid		VSC-HVDC link	
$\overline{I}_{\text{OFF0}}$	$0.1999\angle 0.14$ pu	P_{OFF0}	0.1996 pu
$\overline{V}_{\text{WF}}$	$1.0002\angle 0.14$ pu	$(V_{dc0})_{\text{OFF}}$	1.5003 pu
		I_{cc0}	0.1330 pu
Multi-machine AC system			
Iteration-1, $Q_1 = 0$			
$\overline{V}_{\text{ON0}}$	$0.9966\angle -0.70$ pu	P_{ON0}	0.1995 pu
Q_{PCC0}	-0.004 pu	$\overline{V}_9$	$0.9948\angle -1.85$ pu
Iteration-2, $Q_2 = -0.004$ pu			
$\overline{V}_{\text{ON0}}$	$0.9971\angle -0.71$ pu	P_{ON0}	0.1995 pu
Q_{PCC0}	0 pu	$\overline{V}_9$	$0.9949\angle -1.86$ pu
$Q_{\text{ON0}} = -Q_2 = 0.004$ pu			
PMSG aggregated wind farm			
Aggregated Parameters	R_s = 0.0085 pu, x_{sd} = 0.9981 pu, x_{sq} = 1.9053 pu H_s = 0.1613, R_{GSC} = 0.005 pu, X_{GSC} = 0.05 pu		
$I_{q0} + jI_{d0}$	$0.1999 + j0$ pu	P_{GSC0}	0.2002 pu
ω_{r0}	0.7019 pu	i_{sq0}	0.34404 pu
V_{w0}	9.8052 m/s		

2. The initial wind speed is given as 9.8052 m/s and the total wind turbines in the wind farm is given as 18.

This study corresponds to case-3 of the proposed method. The results are tabulated in Table 4.2. By applying the proposed iterative algorithm for the offshore AC network, the reactive power at the WF bus is obtained as zero in two iterations. The results for the VSC-HVDC link and multi-machine system remain the same as that of the previous case study.

Table 4.2: Load flow and initial condition calculations (Case-3)

Specified Quantities	V_{w0} = 9.8052 m/s, N_{WT} = 18, Q_{WF0} = 0 pu $(\overline{V}_{\mathrm{OFF0}})_{\mathrm{PCC}} = 1\angle 0$ $(V_{dc0})_{\mathrm{ON}}$ = 1.5 pu, Q_{PCC0} = 0 pu		
Load flow and Initial condition calculations			
PMSG aggregated wind farm			
ω_{r0}	0.7019 pu	T_{m0}	0.28668 pu
i_{sq0}	0.34404 pu	v_{sq0}	0.5819 pu
$P_{\mathrm{GSC0}} = P_{s0}$ = 0.2002 pu			
Offshore AC Network			
Iteration-1, Q_{GSC0} = 0 pu			
$\overline{V}_{\mathrm{GSC0}}$	$1.0011\angle 0.71$ pu	$\overline{I}_{\mathrm{OFF0}}$	$0.1999\angle 0.71$ pu
$\overline{V}_{\mathrm{WF0}}$	$1.0002\angle 0.14$ pu	Q_{WF0}	-0.0019 pu
Iteration-2, Q_{GSC0} = 0.0019 pu			
$\overline{V}_{\mathrm{GSC0}}$	$1.0012\angle 0.71$ pu	$\overline{I}_{\mathrm{OFF0}}$	$0.1999\angle 0.14$ pu
$\overline{V}_{\mathrm{WF0}}$	$1.0002\angle 0.14$ pu	Q_{WF0}	0 pu

3. 3-phase fault on the onshore PCC

A 3-phase to ground fault is applied on the onshore PCC (bus-9) at 1s. Basic blocks in SIMULINK is used to build the model. The wind speed at the wind farm is 9.8052 m/s as shown in Figure 4.5a. At this wind speed, the PMSG rotor speed, torque and stator power output are given in Figure 4.5b, Figure 4.5c and Figure 4.5d respectively. The offshore VSC maintains constant voltage and frequency at offshore grid as displayed in Figure 4.6a and Figure 4.6b respectively. It can be seen that the fault on the onshore AC system does not have an effect on these quantities. This is due to the fact that the VSC-HVDC link decouples the offshore wind farm and offshore grid from the AC system. The waveforms in Figure 4.5a – Figure 4.6b exhibit the calculated initial conditions right from the beginning of the simulation proving the efficiency of the proposed approach.

The power delivered by the wind farm at the onshore converter is given in Figure 4.6c and the electromagnetic torques of the system generators are given in Figure 4.6d. The initial operating conditions are displayed in the waveforms until the onset of fault i.e. 1s. As the fault applied is a 3-phase to ground fault which is the most severe fault in power systems, overshoots can be observed at the onset of the event. However, the system has been designed with appropriate limits according to (Padiyar K.R., 2002, Stijin et al., 2010) ensuring that it works with reasonable operating points.

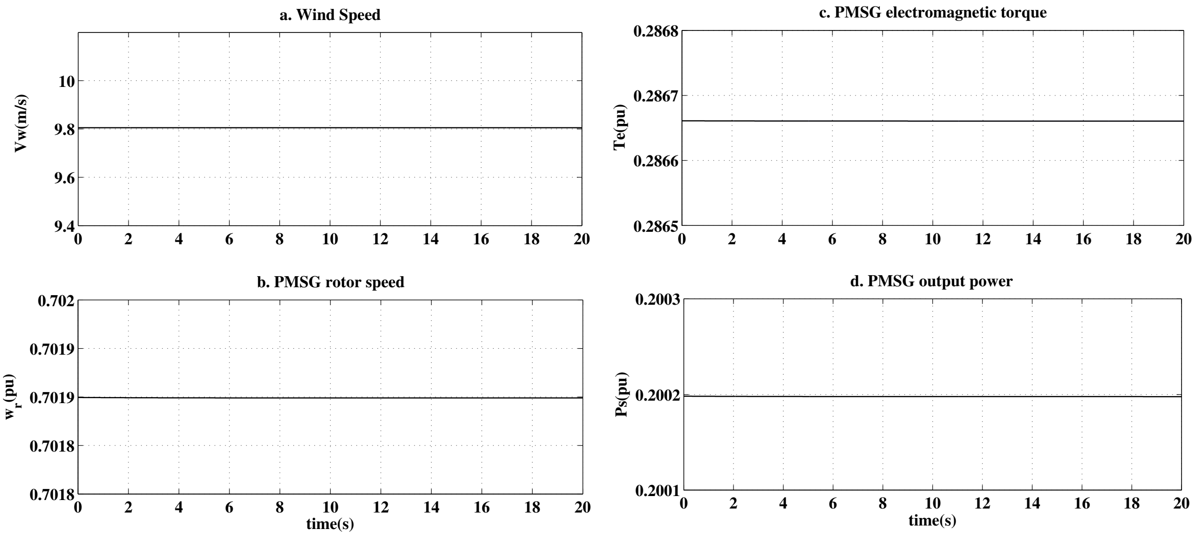

Figure 4.5: 3-phase fault on the onshore PCC : Wind farm quantities

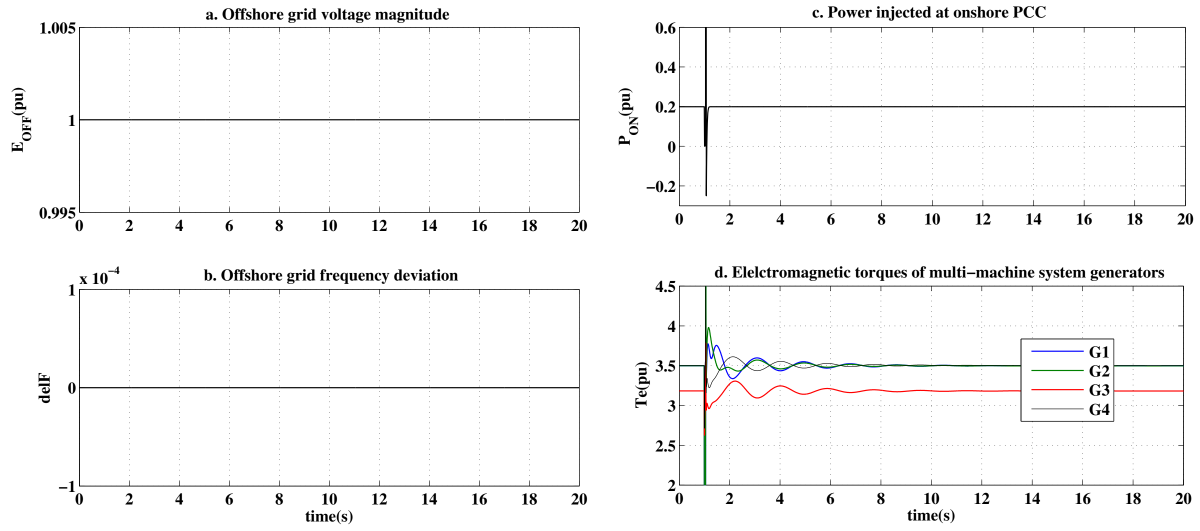

Figure 4.6: 3-phase fault on the onshore PCC : Offshore grid quantities and 4-machine system quantities

4.5.2 Case Study 2: 16-machine, 68-bus system

In this section, generator G1 of the 16-machine, 68-bus base system given in Figure 3.22 is replaced by a VSC-HVDC connected offshore wind farm (Appendix A2, A3) shown in

Figure 4.7. It is interfaced to the 16-machine system at bus-53. The offshore wind farm delivers 2.65 pu of power at the wind farm bus. The loadflow and initial condition calculations are given in Table. 4.3. The calculations pertain to case-1 of the proposed method. The VSC-HVDC, offshore network and wind turbine details are given in the appendix. The important results of offshore network calculations followed by VSC-HVDC and then multi-machine initial conditions are presented. The offshore wind farm is operating at a wind speed of 9.83 m/s.

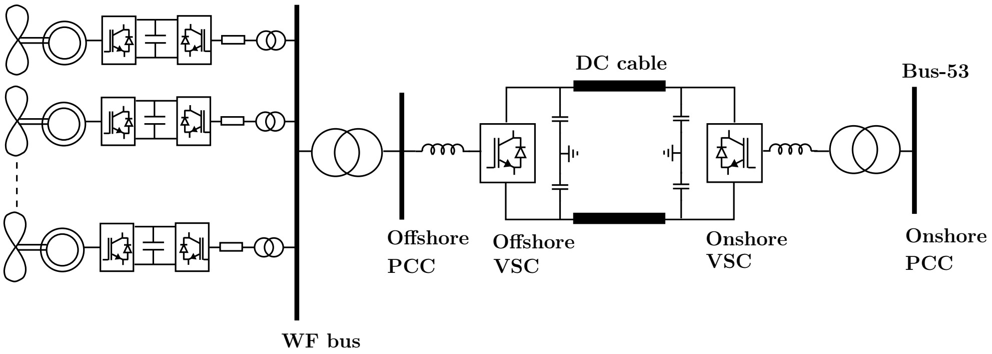

Figure 4.7: VSC-HVDC connected offshore wind farm

Further, a 3-phase to ground fault is applied on bus-2 of the system at 1s. The fault is cleared after 0.05s. The plots of the voltage magnitude at bus-2 and power in AC transmission line 2-1 are presented in Figure 4.8. In addition, the plots of voltage magnitude at bus-53 and the onshore VSC AC current magnitude plot are given in Figure 4.9. The dynamic analysis is also compared with the results obtained when the simplified model of VSC-HVDC discussed in Chapter 3 is used. The waveforms demonstrate the initial conditions from the onset of the simulation. It can be observed that the system employing simplified model of the link performs exactly similar to the system with full model. Despite the proximity of the fault from the link, the oscillations and transients are very well exhibited by the simplified model, even with a severe fault.

At 1s, wind speed is stepped up from 9.83 m/s to 12 m/s as shown in Figure 4.10(i). The power delivered at bus-53 by the wind farm through the HVDC link is given in Figure 4.10(ii). The onshore VSC AC current magnitude and power in the AC line 2-1 is given in Figure 4.11. Even in this context, the waveforms demonstrate the accurate representation of the calculated initial conditions from the onset of the simulation, thereby validating the effectiveness of the proposed methodology. It can be observed that power plot at bus-53

Table 4.3: Initial condition calculations for 16-machine system

Specified Quantities	$P_{\text{WF0}} = 2.65$ pu, $Q_{\text{WF0}} = 0$ pu, $(\overline{V}_{\text{OFF0}})_{\text{PCC}} = 1\angle 0$ $(V_{dc0})_{\text{ON}} = 1.5$ pu, $Q_{\text{PCC0}} = 0$ pu $N_{\text{WT}} = 237$, $i_{sd0} = 0$ pu		
Load flow and Initial condition calculations			
Offshore Grid		VSC-HVDC link	
$\overline{I}_{\text{OFF0}}$	$2.6443\angle 1.82$ pu	P_{OFF0}	2.5731 pu
$\overline{V}_{\text{WF}}$	$1.0021\angle 1.82$ pu	$(V_{dc0})_{\text{OFF}}$	1.5036 pu
		I_{cc0}	1.7112 pu
Multi-machine AC system			
Iteration-1, $Q_1 = 0$			
$\overline{V}_{\text{ON0}}$	$0.9813\angle 24.38$ pu	P_{ON0}	2.5669 pu
Q_{PCC0}	-0.6843 pu	$\overline{V}_{53}$	$0.9904\angle -11.28$ pu
Iteration-2, $Q_2 = -0.6843$ pu			
$\overline{V}_{\text{ON0}}$	$1.0748\angle 24.38$ pu	P_{ON0}	2.5669 pu
Q_{PCC0}	0.0726 pu	$\overline{V}_{53}$	$1.014\angle 11.11$ pu
Iteration-3, $Q_3 = -0.6117$ pu			
$\overline{V}_{\text{ON0}}$	$1.0651\angle 24.58$ pu	P_{ON0}	2.5669 pu
Q_{PCC0}	-0.0021 pu	$\overline{V}_{53}$	$1.0113\angle 11.13$ pu
Iteration-4, $Q_4 = -0.6138$ pu			
$\overline{V}_{\text{ON0}}$	$1.0653\angle 24.58$ pu	P_{ON0}	2.5669 pu
Q_{PCC0}	0 pu	$\overline{V}_{53}$	$1.0113\angle 11.13$ pu
$Q_{\text{ON0}} = -Q_4 = 0.6138$ pu			
PMSG aggregated wind farm			
Aggregated Parameters	$R_s = 0.00065$ pu, $x_{sd} = 0.0758$ pu, $x_{sq} = 0.1447$ pu $R_{\text{GSC}} = 0.00038$ pu, $X_{\text{GSC}} = 0.0038$ pu		
$I_{q0} + jI_{d0}$	$2.6443 + j0$ pu	P_{GSC0}	2.6526 pu
ω_{r0}	0.7034 pu	i_{sq0}	4.5491 pu
V_{w0}	9.83 m/s		

for system with simplified model overlaps with that of full model. Due to the change in wind speed, the power delivered increases almost by 50% of initial power. In such a case, a slight deviation in the performance between system with simplified and full model can be observed in the quantities given in Figure 4.11. However, given the magnitude of operating conditions, lower modeling complexity and higher computation speeds, these deviations are acceptable. In addition, this condition arises when the wind speed is stepped to nominal speed. As a result, any further rise in wind speed would not result in any further significant increase in the deviations in the quantities of the system.

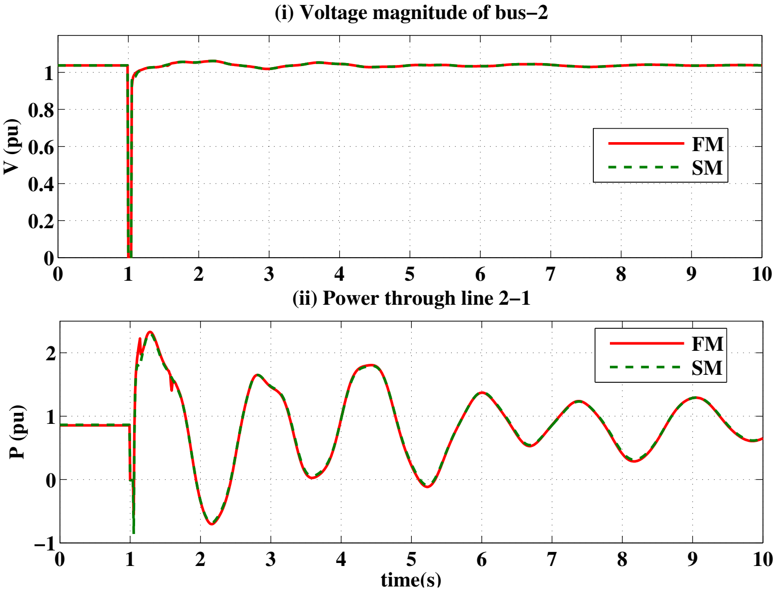

Figure 4.8: 3-phase fault at bus-2 : (i) Voltage magnitude at bus-2 (ii) Power in the line 2-1

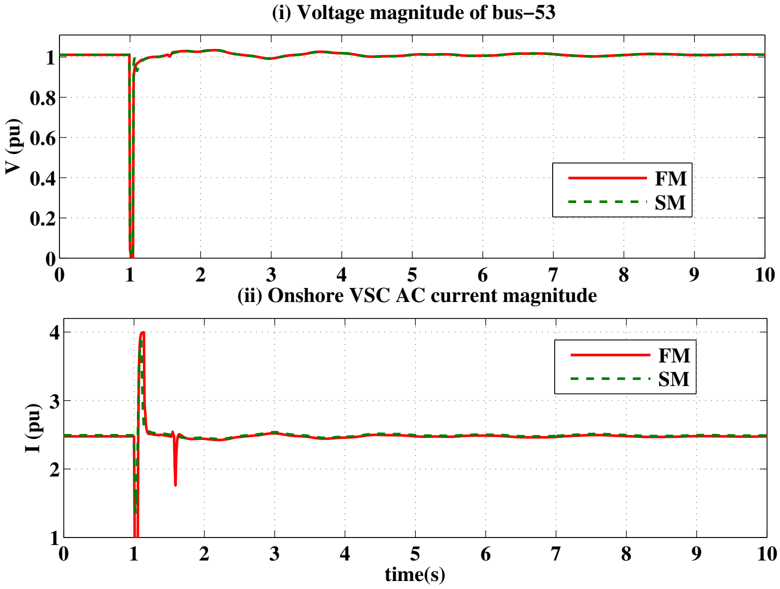

Figure 4.9: 3-phase fault at bus-2 : (i) Voltage magnitude at bus-53 (ii) Onshore VSC AC current

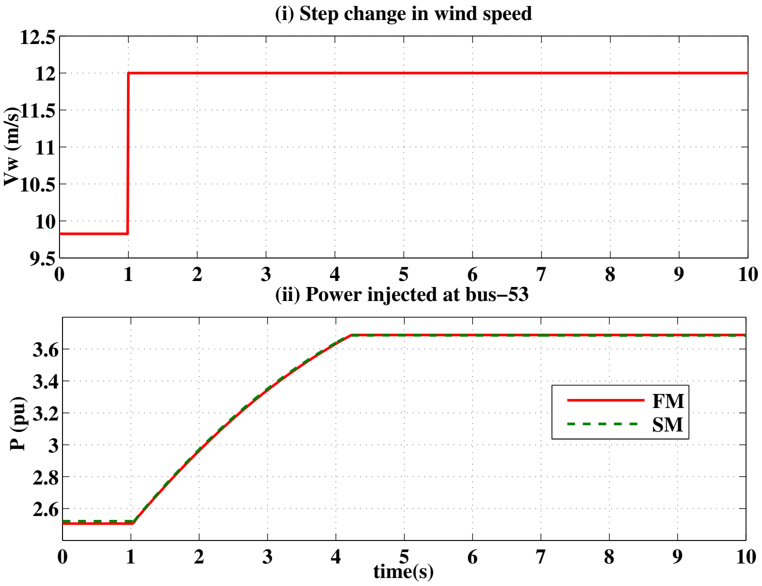

Figure 4.10: Step change in wind speed : (i) Wind speed (ii) Power delivered at bus-53

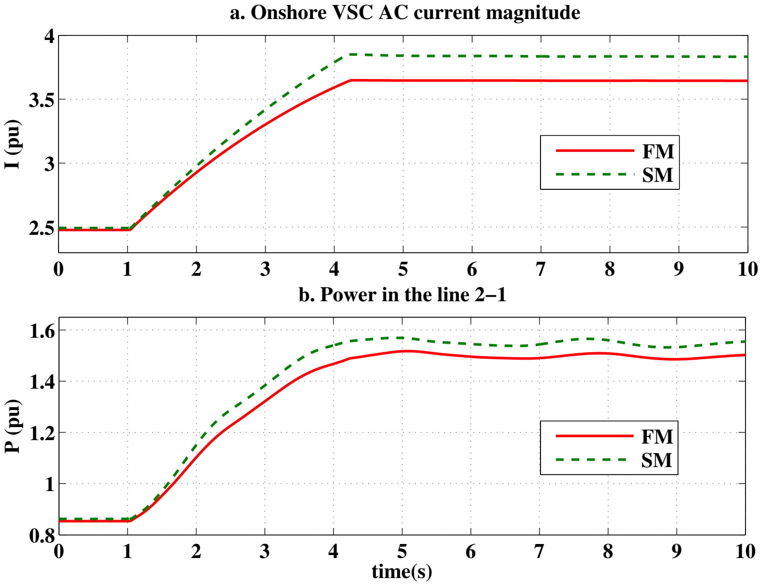

Figure 4.11: Step change in wind speed : (i) Onshore AC current magnitude (ii) Power in the AC line 2-1

4.6 Summary

This chapter presented a unique approach for power flow and initial condition computations of VSC-HVDC connected DD-PMSG wind farms integrated into multi-machine systems, which can aid the dynamic model of the system. The research conducted in this chapter can be summarised as follows. :

- The method proposed allows the complete system dynamic model to be implemented in easily available basic dynamic modeling packages without the need for power system toolboxes or electromagnetic transient packages.
- The strategy is proposed for three cases of specified quantities of the aggregated wind farm.
  - In the first case, the total real power delivered by the wind farm and the total number of wind turbines are specified. The method to derive the initial wind speed required for the dynamic analysis is described in this case. Also, to avoid complex calculations, the onshore VSC converter bus is included in the load flow of the multi-machine system. An algorithm is proposed to maintain reactive power at onshore PCC as zero.
  - The second case specifies the total real power output of the wind farm and the output from each wind turbine. The technique is identical to the first case, except that the number of wind turbines must be estimated separately.
  - In the third case, the specified quantities are the initial speed of wind and the total wind turbines in the wind farm. An algorithm is presented to calculate the real power output at the wind farm bus and to maintain reactive power at the wind farm bus to zero.
- The proposed approach is validated through case studies carried out on an offshore DD-PMSG wind farm integrated to a 4-machine and 16-machine systems via a VSC-HVDC link. MATLAB/SIMULINK environment is used.
- Significant power flow and initial conditions results that can assist the dynamic analysis are displayed. Dynamic response of the entire system is obtained by initiating dynamic events. The initial conditions displayed in the waveforms prove the effectiveness of the strategy.

- The simplified VSC-HVDC model discussed in previous chapter is validated for 16-machine system with VSC-HVDC based offshore wind farm. The dynamic analysis results affirm the model's suitability for use in large AC systems involving VSC-HVDC based offshore wind farms operating under conventional control strategies.

The VSC-HVDC link isolates the offshore wind farm from the onshore power system. As we move towards integrating more converter-based systems into the grid in the future, there will be a significant impact on the overall stability of the system. To address this challenge, it becomes imperative for both the VSC's and offshore wind farms to actively participate in ensuring synchronization and maintaining frequency stability within the system. In this context, the next chapter will explore grid synchronization and inertial techniques specific to VSC-HVDC-based offshore wind farms.

Chapter 5

GRID SYNCHRONISATION AND INERTIAL SUPPORT

5.1 Introduction

The increasing penetration of VSC-HVDC based offshore wind integration poses major threat to the frequency stability of the power system due to the decline in inertia. The traditional method of using a Phase-Locked Loop for synchronizing the grid side VSC (GSVSC) with the power grid does not work well when the grid is weak. This emphasizes the need for additional control methods that can provide grid synchronisation, inertial and frequency support from power electronic interfaces in weak power systems as already mandated in grid codes around the world.

In this chapter, a novel approach for grid synchronisation and inertial support from VSC-HVDC connected offshore wind farms in weak system is presented. The DC capacitor dynamics mimicking synchronous generator mechanics is used for grid synchronisation. As the DC dynamics are directly used, a quick grid synchronisation is achieved. The inertia from the DC capacitor as well as the inertia from the PMSG's of individual wind turbines are tapped. The controller includes inherent damping capabilities and no separate control loop is added. A time constant based approach is described which allows for usage of two distinct DC voltage tolerance band ranges for the response. A larger tolerance band whose influence on the inertial response time period depends on the time constant chosen. And a smaller tolerance band impacting the rest of time period of the response. This method has been proved to enhance the total inertial response of the system in comparison to the existing strategies. The tolerance bands are chosen based on the data available in literature. Upon choosing the time constant, the rest of parameters of the controller can be easily derived.

5.2 Methodology

In order to illustrate the control strategy, the system described in the previous chapter *i.e* an offshore wind farm integrated to onshore power system via a point to point VSC-HVDC system is used as shown in Figure 5.1. The onshore power system is represented here by a single synchronous generator connected to onshore PCC.

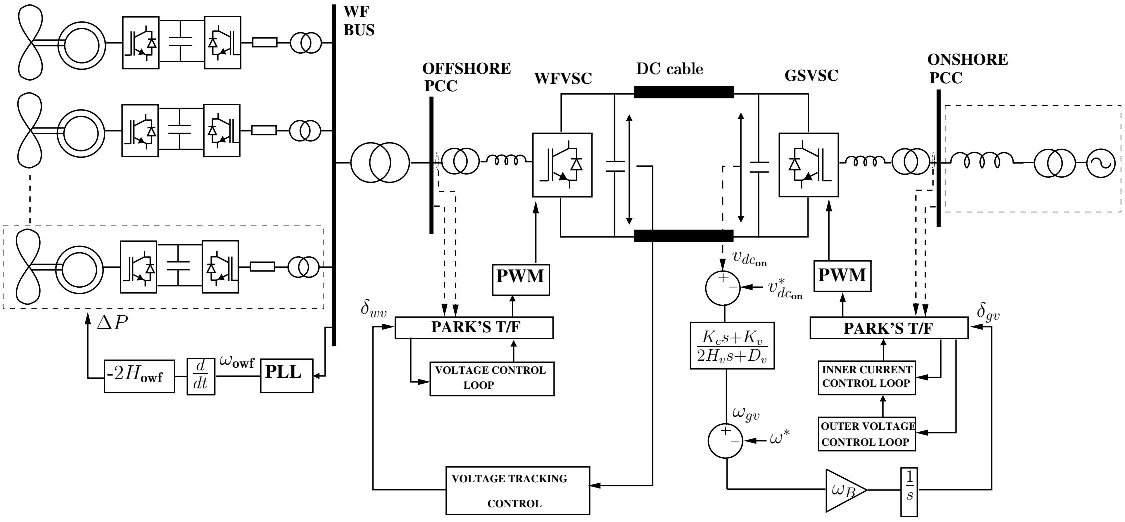

Figure 5.1: VSC-HVDC based offshore wind farm integrated to AC onshore system with proposed control strategy

From Figure 5.1, the dynamics of the HVDC link capacitor associated with GSVSC in per unit is given as,

$$K_c \frac{dv_{dc_{\text{ON}}}}{dt} = P_T - P_{\text{ON}} \tag{5.1}$$

where $K_c = \frac{v_{dc_{\text{on0}}} C_{dc}}{\omega_{gB}}$. $v_{dc_{\text{ON}}}$ is the DC voltage across the capacitor, P_T is the power transferred from the offshore wind farm, P_{ON} is the power injected to the onshore AC system, C_{dc} is the per-unit capacitance, ω_{gB} is the base angular frequency. The steady state DC voltage $v_{dc_{\text{on0}}}$ is defined in K_c as it varies in a very small range.

The general form of swing equation of the synchronous generator (in per-units) is well known as,

$$2H\frac{d\omega}{dt} = P_m - P_{eg} - D(\omega - \omega^*) \tag{5.2}$$

Considering (5.2) and (5.1), it can be seen that the DC voltage of the VSC-station plays a similar role in reflecting the power balance in the grid. Further, it can be observed that the DC voltage is analogous to the rotor speed of a synchronous generator. Using this co-relation, in order to provide independent grid synchronisation avoiding the use of PLL as well as provide inertial support, a novel control approach is proposed for GSVSC.

In case of DC link capacitors participating in grid synchronisation and inertial support process, it becomes extremely important to track the variations in the DC voltage and keep it within the allowable limit. Hence, a voltage tracking coefficient K_v is introduced and the capacitor equation is rewritten as,

$$K_c\frac{dv_{dc_{\mathrm{ON}}}}{dt} = P_T - P_{\mathrm{ON}} - K_v(v_{dc_{\mathrm{ON}}} - v^*_{dc_{\mathrm{ON}}}) \tag{5.3}$$

Considering that the GSVSC can emulate synchronous generator characteristics, the dynamics of the output frequency of GSVSC ω_{gv} can be written as,

$$2H_v\frac{d\omega_{gv}}{dt} = P_T - P_{ON} - D_v(\omega_{gv} - \omega^*) \tag{5.4}$$

where H_v is the inertia constant and D_v is the frequency damping constant of the controller. The inertial capability provided by the DC capacitor provided through H_v is discussed in detail in Section 5.2.1.

Equating the capacitor DC voltage dynamics and the GSVSC frequency dynamics,

$$2H_v\frac{d\omega_{gv}}{dt} + D_v(\omega_{gv} - \omega^*) = K_c\frac{dv_{dc_{\mathrm{ON}}}}{dt} + K_v(v_{dc_{\mathrm{ON}}} - v^*_{dc_{\mathrm{ON}}}) \tag{5.5}$$

Applying the Laplace transform it can be rewritten as,

$$\begin{aligned}(2H_vs + D_v)(\omega_{gv} - \omega^*) &= (K_cs + K_V)(v_{dc_{\mathrm{ON}}} - v^*_{dc_{\mathrm{ON}}})\\ \omega_{gv} - \omega^* &= \frac{(K_cs + K_v)}{(2H_vs + D_v)}(v_{dc_{\mathrm{ON}}} - v^*_{dc_{\mathrm{ON}}})\end{aligned} \tag{5.6}$$

Thus, the synchronising signal δ_v required for dq transformation is obtained as,

$$\frac{d\delta_{gv}}{dt} = \omega_{gB}(\omega_{gv} - \omega^*) \tag{5.7}$$

The control applied at GSVSC is given in Figure 5.1.

Due to the control applied at GSVSC, any change in the frequency of the onshore power system can also be sensed by the WFVSC by tracking its respective DC capacitor's voltage. This information has to be passed to the offshore wind farm side in order to the tap the inertia from PMSG wind turbines. In order to do this, a similar control is applied on the WFVSC, so that the offshore grid frequency can replicate the onshore frequency by tracking the changes in the offshore DC voltage. In a conventional approach, the WFVSC would be maintaining the voltage and frequency at offshore grid constant through a virtual PLL. The control is modified to obtain the output frequency ω_{wv} of WFVSC as,

$$\omega_{wv} - \omega^* = \frac{(K_c s + K_v)}{(2H_v s + D_v)}(v_{dc_{\mathrm{OFF}}} - v^*_{dc_{\mathrm{OFF}}}) \tag{5.8}$$

where $(v_{dc_{\mathrm{OFF}}} - v^*_{dc_{\mathrm{OFF}}})$ is the DC link voltage deviation at the offshore side. The synchronising signal of the virtual PLL is given as,

$$\frac{d\delta_{wv}}{dt} = \omega_{gB}(\omega_{wv} - \omega^*) \tag{5.9}$$

Thus, the frequency information of the onshore power system is delivered to the offshore grid.

In order to tap the inertial potential from the offshore wind farms, the frequency information at the offshore grid is transferred as additional power to the MPPT power. The extra power is a function of the rate of change of frequency at the offshore grid (ω_{owf}) given as,

$$\Delta P = -2H_{\mathrm{owf}}\frac{d\omega_{\mathrm{owf}}}{dt} \tag{5.10}$$

The total reference power at the wind turbine is given as,

$$P^*_{\mathrm{wf}} = P_{\mathrm{m}} + \Delta P \tag{5.11}$$

where P_{m} is the MPPT reference power.

Taking P_T = P^*_{wf} and due to the frequency replication control established, (5.4) can be re-written as,

$$(2H_v + 2H_{\mathrm{owf}})\frac{d\omega_{gv}}{dt} = P_m - P_{on} - D_v(\omega_{gv} - \omega^*) \tag{5.12}$$

It can be observed that the entire VSC-HVDC based offshore wind farm behaves similar to a synchronous generator with combined inertia of the HVDC capacitors and offshore wind farm.

5.2.1 Parameter Selection

The general form of time domain response of the controllers of (5.6) and (5.8) is given as,

$$\Delta\omega(t) = \left[\frac{K_v}{D_v} + \left(\frac{K_c}{2H_v} - \frac{K_v}{D_v}\right)e^{-(\frac{D_v}{2H_v})t}\right]\Delta v_{dc}(t) \tag{5.13}$$

The time constant can be defined as,

$$\tau = \frac{2H_v}{D_v}$$

This time constant governs the influence of the four constants of 5.8 on the system.

However, K_c is already a known constant given as,

$$K_c = \frac{v_{dc_{\mathrm{on0}}} C_{dc}}{\omega_{gB}} \tag{5.14}$$

The constant H_v is the inertial constant of the DC capacitor. It can be derived as,

$$\begin{aligned} 2H_v &= \frac{\int_{v_{dc0_{\mathrm{ON}}}}^{v_{dc1_{\mathrm{ON}}}} K_c\, dv_{dc}}{\int_{\omega_0}^{\omega_1} d\omega} \\ &= \frac{K_c \Delta v_{dch}}{\Delta\omega} \end{aligned} \tag{5.15}$$

where Δv_{dch} is the allowable DC link voltage deviation during the initial part of inertial response and $\Delta\omega$ is the allowable frequency deviation.

The parameters K_v and D_v are the damping constants which would depend on the deviation allowed for the DC link voltage and frequency. It can be given as,

$$\frac{K_v}{D_v} = \frac{\Delta\omega}{\Delta v_{dcd}} \tag{5.16}$$

where Δv_{dcd} is the DC link voltage deviation for the later part of inertial response.

Thus, it can be understood that, the frequency deviation in 5.13, would depend on $\frac{\Delta\omega}{\Delta v_{dch}}$, $\frac{\Delta\omega}{\Delta v_{dcd}}$ and τ.

By choosing $\Delta v_{dch} > \Delta v_{dcd}$ and an appropriate time constant τ, a higher capacitor energy can be obtained at the beginning of the inertial response and also allows the choice of other constants. According to literature, the allowable DC voltage tolerance band for HVDC systems ranges from ±5% - ±15% of the nominal DC voltage. However, many countries prefer a more stringent band of ±5% or less, with China having a particularly strict band of ±3%. A larger tolerance band for a long period of time would lead to adverse effects on the operation on DC system, especially when considering the impact on the DC submodules of MMC-HVDC. Considering the above facts, in order to ensure a reliable operation, the Δv_{dcd} is fixed at 5% and Δv_{dch} is fixed at 10%. The system would be influenced by Δv_{dch} based on τ. It is well known that the inertial response lasts around 6s after the onset of a frequency disturbance and the influence of Δv_{dch} based on (5.13) would last for around 4τs. Accordingly the time constant τ can be chosen as 0.4s - 0.6s allowing an approximate 25% - 50% influence over inertial response time period. $\Delta\omega$ is maintained at 1%.

5.3 Implementation and validation

The proposed control is implemented in two power systems, Test system - 1 and Test system - 2. MATLAB/SIMULINK is used for the study. The entire system has been per-unitised on a power base of 100MVA, respective voltage bases and frequency bases. In order to get a better perspective, the quantities and parameters are provided in real units during discussion.

5.3.1 Test system - 1

In Test system - 1, VSC-HVDC based PMSG offshore wind farm is connected to a grid represented by a single synchronous generator as shown in Figure 5.2. The offshore wind farm has an aggregated capacity of 420 MW with a virtual inertia constant of 4.9s. The synchronous generator has a capacity of 800 MVA and an inertia constant of 2.57s. The offshore wind farm is connected to the PCC via a VSC-HVDC rated for 450 MVA and ±320 kV. Two loads, a fixed load (L_1) of 6.4 pu (640 MW) and a switchable load (L_2) of 1.6 pu (160 MW) is connected at the PCC. Initially, only L_1 is connected to the system. The rest of the parameters of the system are given in Table 5.1. The short circuit ratio (SCR) is considered to classify the systems into strong, weak and very weak. It is changed by varying the grid reactance (X_{grid}).

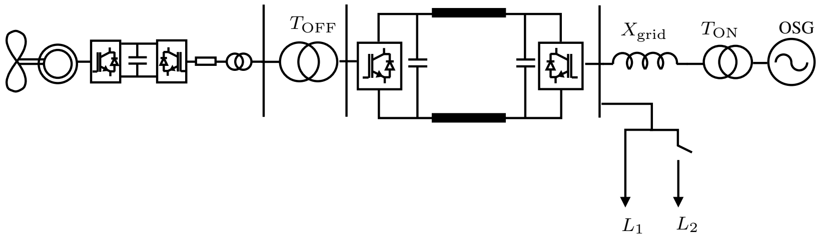

Figure 5.2: Test system - 1

The proposed control is validated by comparing it with the following existing strategies :

1. TC (Traditional control) - It is based on conventional vector control with no inertial response from wind farms or HVDC capacitor and PLL is used for grid synchronisation (refer chapter 4).

2. DCP (Traditional Droop control with PLL) -PLL-derived frequency deviation is converted to GSVSC DC voltage deviation using droop control, which is passed to the offshore grid by tracking WFVSC DC voltage dynamics and modifying virtual PLL reference using droop. This enables the wind farm to provide inertial support (Xudan et al., 2018). A minimum time delay of 5*ms* is considered for this control.

3. DCNP (Droop control without PLL) - This method uses DC capacitor inertia to synchronize with the grid. The GSVSC frequency deviation is obtained through droop control of the DC voltage deviation and is converted into a synchronizing signal. The offshore grid receives the grid frequency information by tracking the WFVSC DC voltage dynamics, similar to the DCP method (Yang et al., 2018).

Table 5.1: Parameters of test system - 1

Parameter	Value
Onshore Synchronous Generator	
Rated Power	800 MVA
Rated Voltage	20 kV
Frequency	50 Hz
x_d, x_d', x_d''	1.6 pu, 0.264 pu, 0.21 pu
x_q, x_q', x_q''	1.52 pu, 0.488 pu, 0.24 pu
T_{d0}', T_{d0}''	8 s, 0.05 s
T_{q0}', T_{q0}''	0.4 s, 0.04 s
Inertia constant	2.57 s
Rated Voltage of T_{ON}	20/230 kV
Leakage reactance of T_{ON}	0.096 pu
VSC-HVDC	
Rated DC voltage	±320 kV
Rated grid voltage	230 kV
Rated Active Power	450 MVA
Number of submodules	220
Submodule capacitance	5.5 mF
Line reactor and transformer	0.504 pu
DC Transmission line	
Resistance	0.0113 Ω/km
Inductance	0.466 mH/km
Length	200 km
Offshore Wind farm (aggregated parameters)	
Offshore grid frequency	50 Hz
Offshore grid rated voltage	230 kV
Rated power	420 MVA
Equivalent Inertia	4.9s
Nominal Wind speed	12 m/s
PMSG stator resistance	0.0034 pu
PMSG q-axis reactance	0.7685 pu
PMSG d-axis reactance	0.4026 pu
Grid side converter resistance	0.002 pu
Grid side converter reactance	0.02 pu

4. PIC (Proportional integral control without PLL) - This control is similar to DCNP control, except that the the frequency information at GSVSC and WFVSC's virtual PLL is obtained by PI control rather than droop control.

The proposed control system is represented as PC. The time constant, $\tau = 0.4\ s$.

5.3.1.1 Strong system

The SCR of system is set to 7.2, which is a strong system according to electrical standards. At 1s, L_2 is added to the system. The simulation results for the event are presented in Figures 5.3 and 5.4. Figure 5.3a shows the frequency dynamics at the onshore PCC upon the occurrence of the event, which is reflected in the DC voltage of GSVSC in Figure 5.3b. The GSVSC output frequency is obtained based on the type of control used, as illustrated in Figure 5.3c.

The initial frequency dip is lowest with the PC. The system with TC does not experience any changes in the DC voltage. In the case of system with PIC, the DC voltage returns to its initial value due to the nature of proportional-integral control. The DC voltage regulation enables the GSVSC output frequency to closely follow the PCC frequency for system with proposed control. The output frequency at GSVSC is almost similar to the PCC frequency for system with DCNP and DCP.

The frequency reflected at the offshore PCC in Figure 5.4a shows that system with DCNP and PC accurately mirror the frequency, with the PC control performing better than DCNP. The DCP control initially struggles to follow the frequency after a fault but eventually maps it correctly after 1.4 seconds. The PIC control performs poorly and is unable to replicate the frequency accurately. The wind farm provides inertial response to the grid, as shown in Figure 5.4b, and the results demonstrate that PC control results in a lower initial ROCOF and, therefore, a lower amount of power given from the wind farm. The power output at the PCC bus in Figure 5.4c consists of inertial power from the DC capacitor. Due to the incorrect frequency information with PIC control, the ROCOF of the PCC frequency is larger than other frequency control strategies. In future case studies, systems with TC and PIC will not be considered.

5.3.1.2 Weak system

The SCR of the system is set to 2.48 which represents a weak system. The simulation results for load L_2 addition at 1s is given in Figure 5.5 and Figure 5.6. In this case, the system with DCP performs poorly due to the instability of the PLL, which results in inaccurate frequency tracking at the onshore PCC (Figure 5.5a). The inaccuracies in frequency tracking get worse as the frequency is transmitted to the offshore side (Figure 5.5b - Figure 5.6c).

On the other hand, the systems utilizing PC and DCNP controls effectively regulate

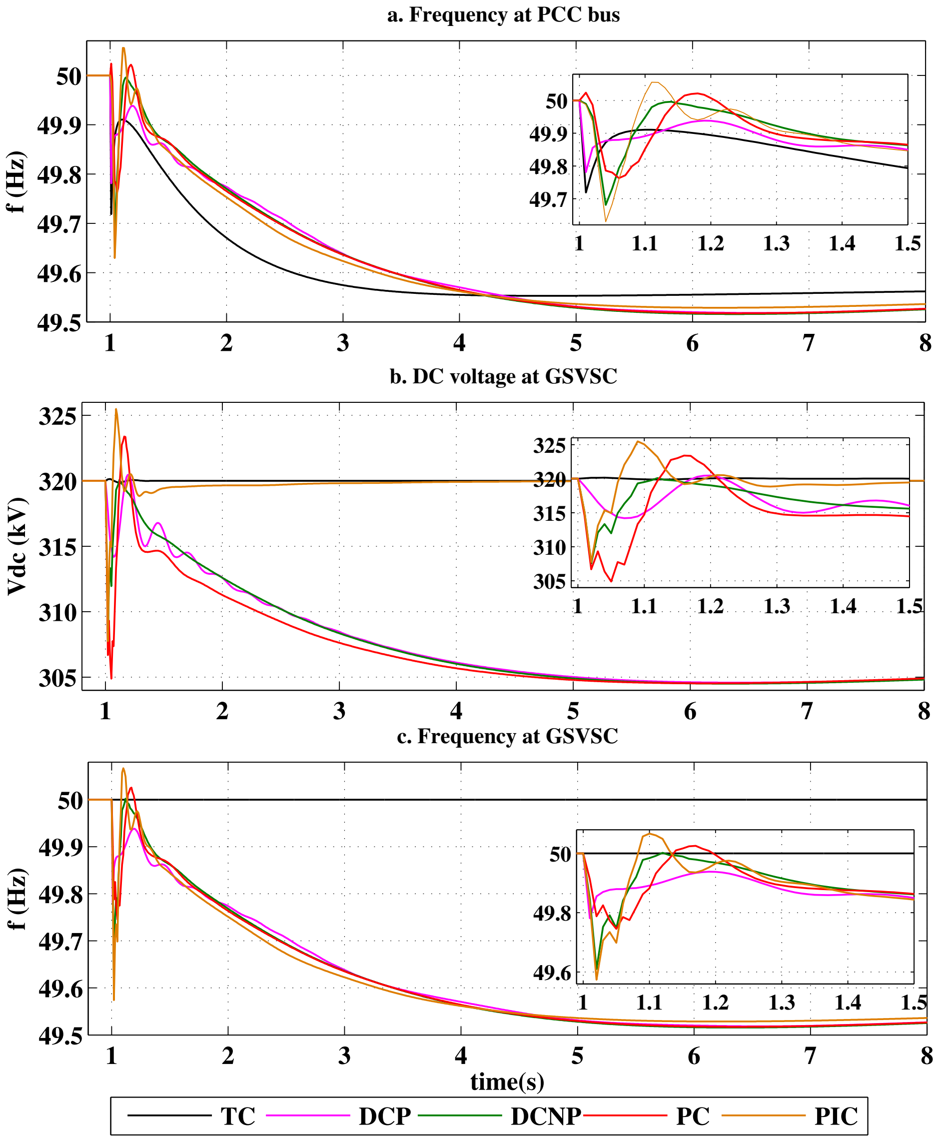

Figure 5.3: Test system - 1 with SCR = 7.2 (Strong system) a) Frequency at PCC bus b) DC voltage at GSVSC c) Frequency at GSVSC

the DC voltage, leading to an output frequency at GSVSC that closely mirrors the grid frequency as soon as the event occurs. The system with PC display fewer oscillations at the PCC bus (Figure 5.5a) than that with DCNP. Additionally, the initial frequency dip is smaller with the system that employs PC due to the larger DC voltage variation allowed for the control. Furthermore, the frequency at the offshore PCC accurately follows the grid

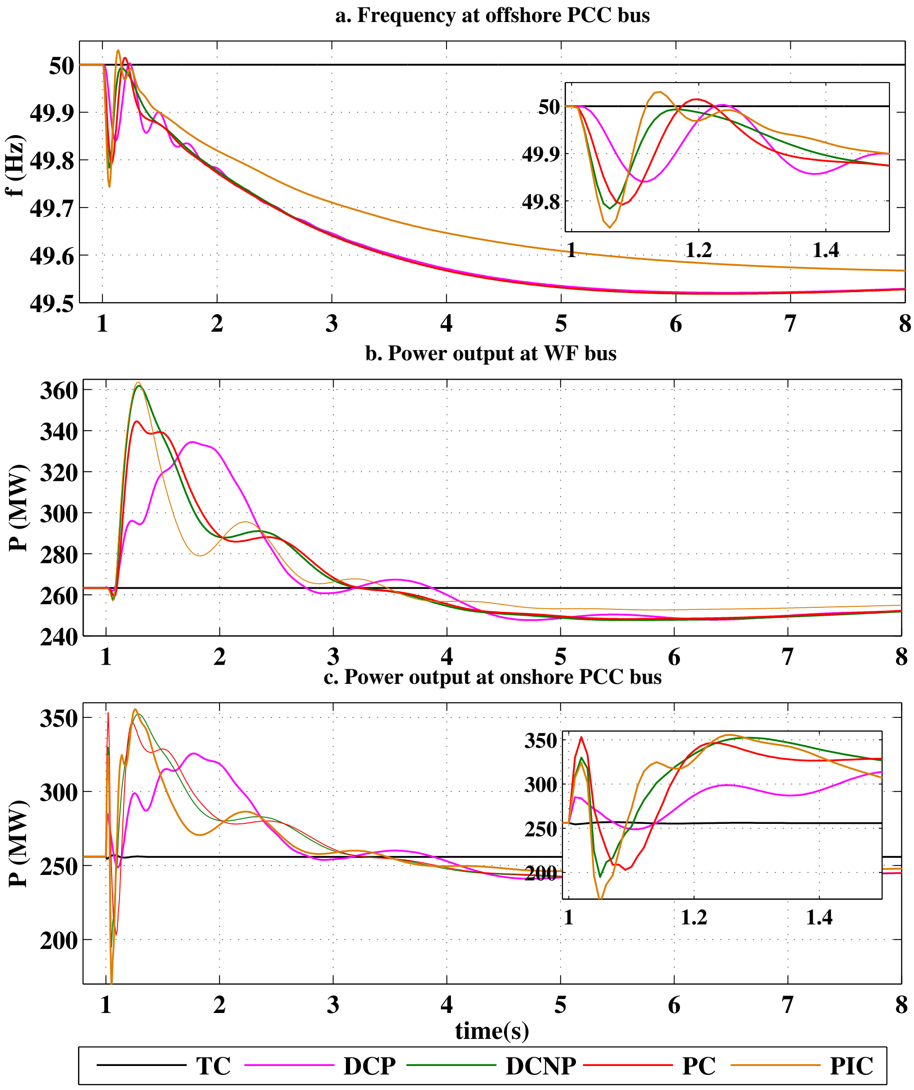

Figure 5.4: Test system - 1 with SCR = 7.2 (Strong system) a) Frequency at Offshore PCC bus b) Power output at WF bus c) Power output at onshore PCC bus

frequency variation, allowing for inertial response from the wind farm, as demonstrated in Figure 5.6a. and Figure 5.6b respectively. The power output at the PCC, which includes the DC capacitor power, shows a better power profile with the system that employs PC when compared to that with DCNP.

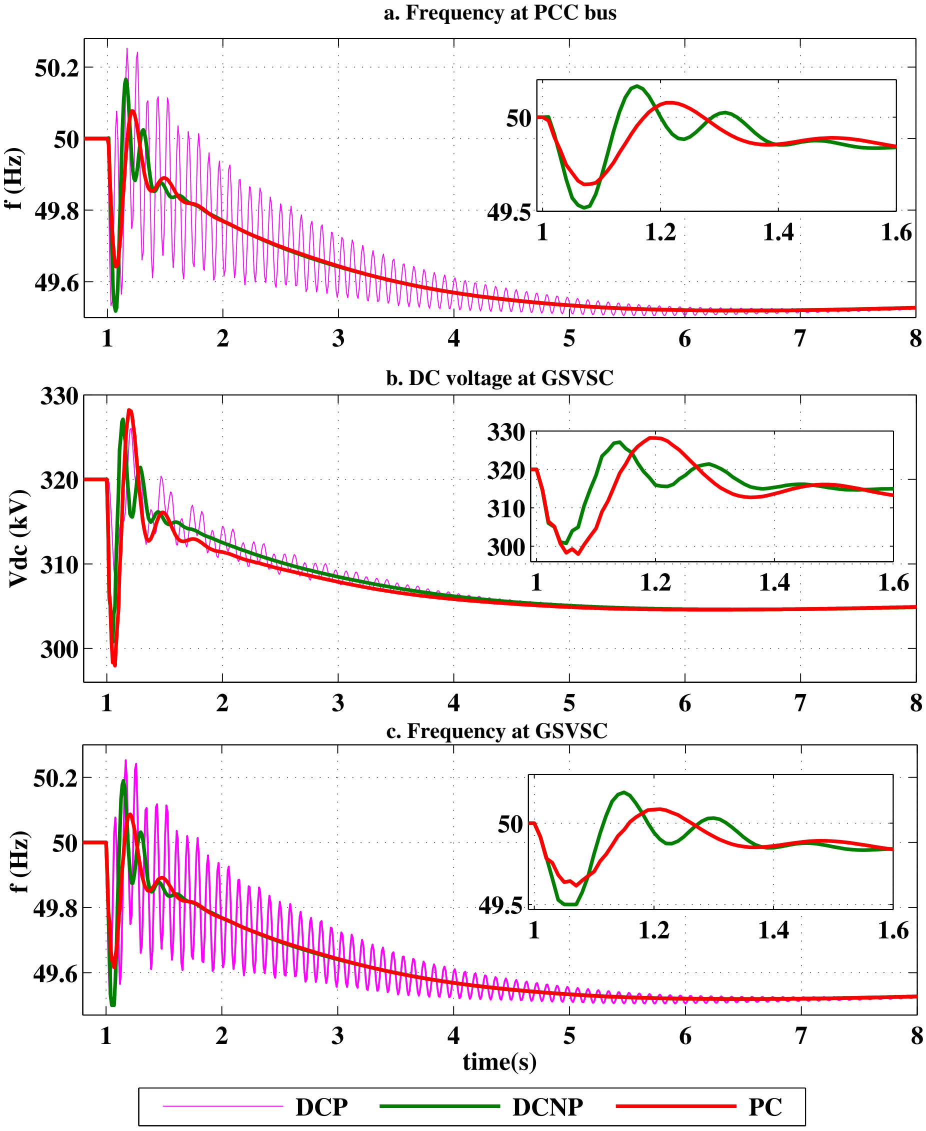

Figure 5.5: Test system -1 with SCR = 2.48 (weak system) a) Frequency at PCC bus b) DC voltage at GSVSC c) Frequency at GSVSC

5.3.1.3 Very weak system

The SCR of the system is set to 1.66 which is a very weak system. The simulation results for load addition is given in Figure 5.7 and Figure 5.8. Due to the very low grid strength, the systems with DCP and DCNP fail to support the system as observed through PCC bus frequency plots in Figure 5.7a and GSVSC DC voltage plot in Figure 5.7b. The frequency

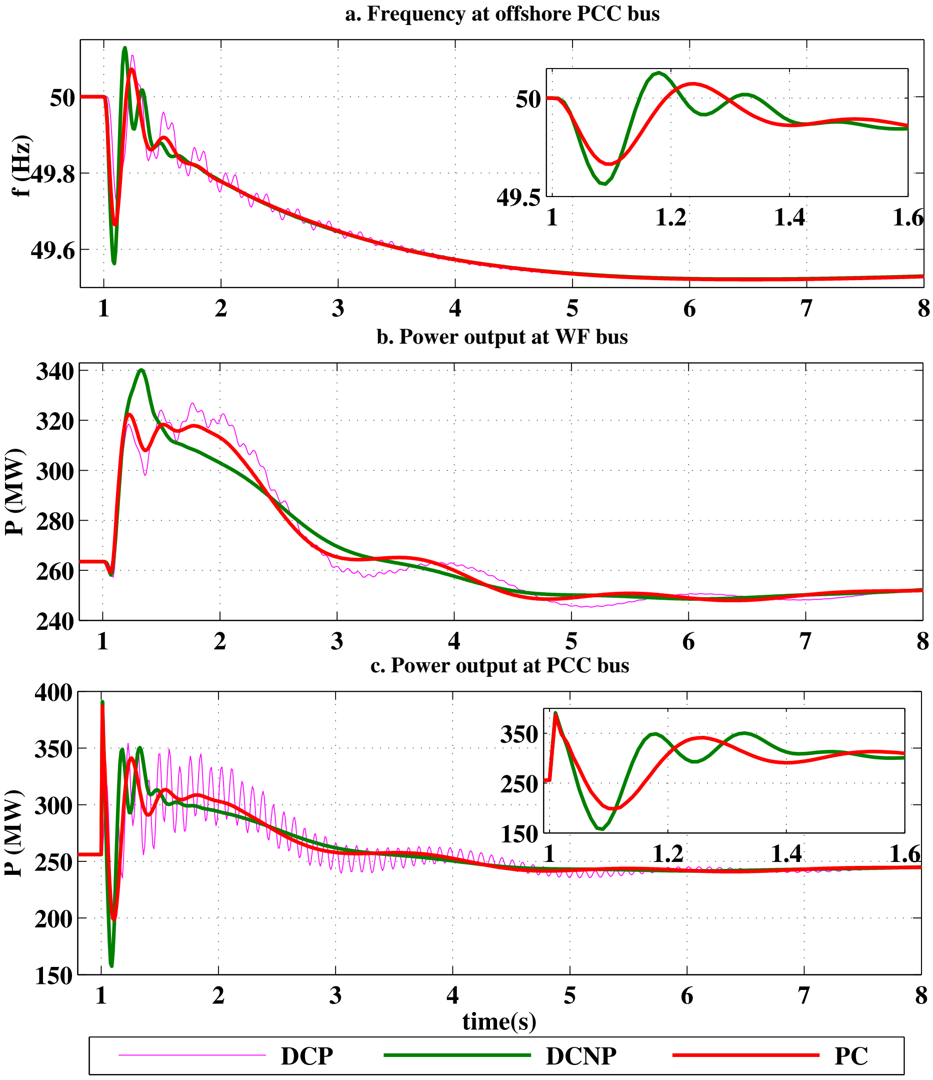

Figure 5.6: Test system - 1 with SCR = 2.48 (weak system) a) Frequency at offshore PCC bus b) Power Output at WF bus c) Power Output at PCC bus

at PCC and DC voltage at GSVSC go unstable and beyond limits. Hence, DCP and DCNP control strategies fail in case of very weak system. However, system with proposed control sustains the low grid strength as shown in Figure 5.8. The frequency at PCC bus and the accurate replication of the same at GSVSC output and offshore PCC is clearly seen in Figure 5.8a. The DC voltage at GSVSC and WFVSC which provides for accurate mirroring of frequency is given in Figure 5.8b. The power output at the wind farm bus is given in

Figure 5.8c. The extra power obtained from the capacitor can be clearly observed in the PCC power output plot. This case clearly proves the effectiveness of the proposed control.

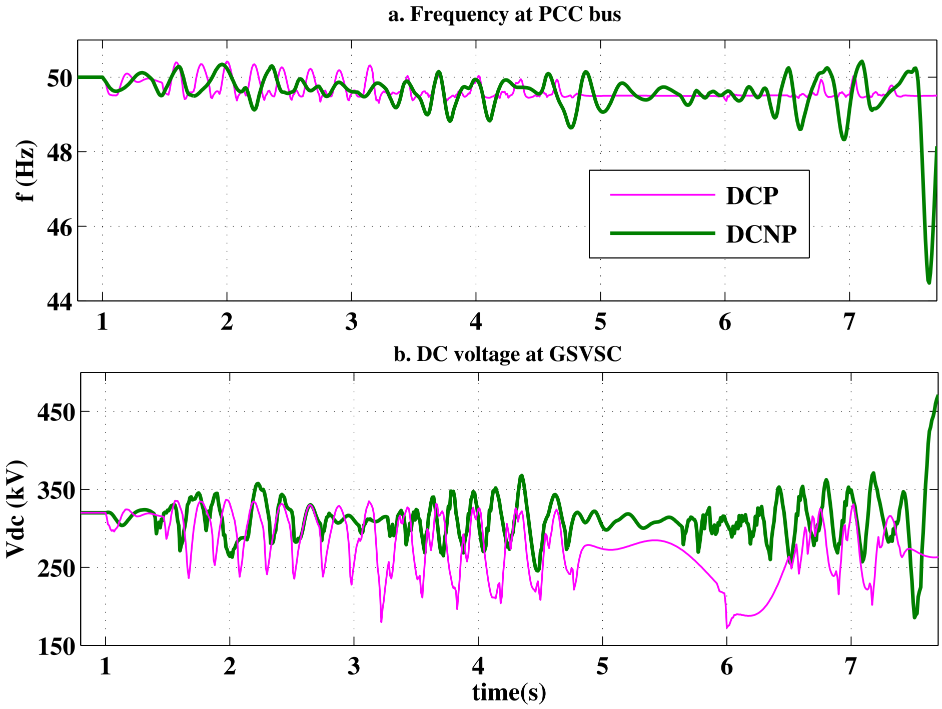

Figure 5.7: Test system-1 with SCR = 1.66 (very weak system) a) Frequency at PCC bus b) DC voltage at GSVSC

5.3.2 Test system - 2

The IEEE 4-machine system (Kundur, 1994) is modified by replacing the generators of area-1 by VSC-HVDC based offshore wind farms. Each of the OWF's are made to deliver the same amount of power as was previously delivered by the synchronous generators. The load at bus 7, L_7 is of 967 MW + j 100 MVAR and load at bus 9, L_9 is 1.967 GW + j 100 MVAR. The loads are considered to be adjustable. Simulation results for system with DCNP and PC have only been presented here. The time constant, $\tau = 0.6\ s$. The ratings of the wind farms and VSC-HVDC are given in Table. 5.2. The 4-machine ratings and parameters are adopted from (Kundur, 1994). The DC transmission line parameters are same as that of Test System - 1. The offshore wind farm parameters of Test System-1 are aggregated to the base value of the Test System -2.

a. Frequency plots

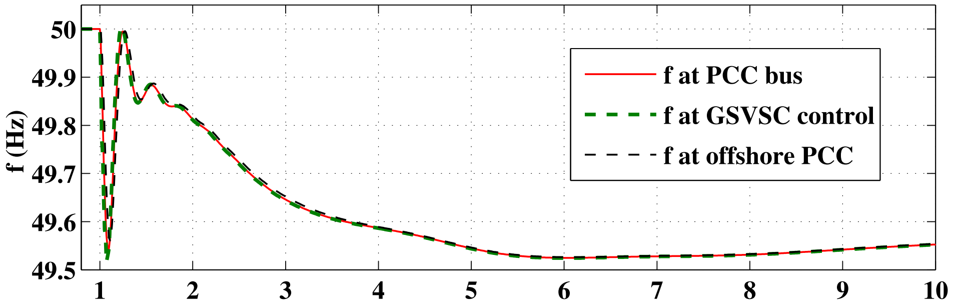

b. DC voltage plots

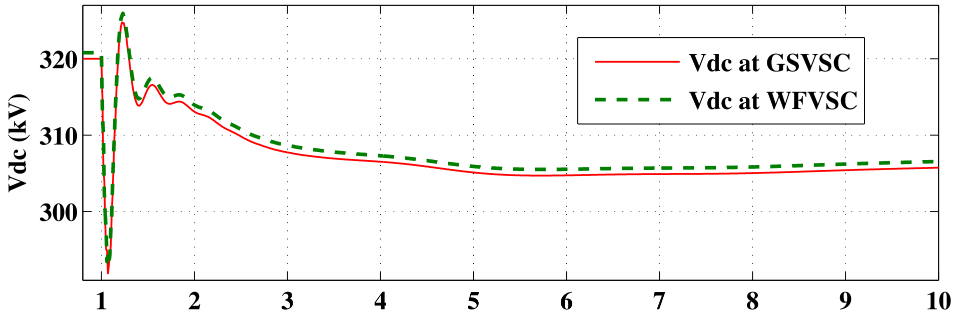

c. Power plots

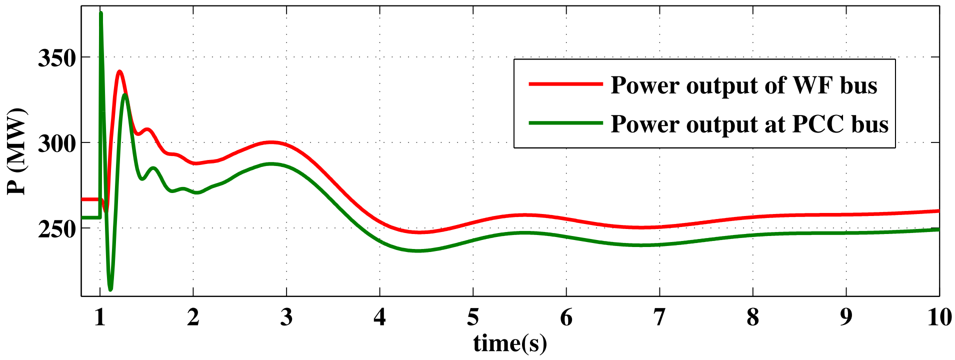

Figure 5.8: Test system-1 with SCR = 1.66 (very weak system) a) Frequency plots b) DC voltage plots c)Power Plots

5.3.2.1 Load addition at bus-7

At 1s, a load of 290 MW + j 3 MVAR is added at bus-7. The simulation results are given in Figure 5.10 and Figure 5.11. The frequency at load bus-7 is presented in Figure 5.10a. Immediately upon the onset of the event, the DC voltages at the GSVSC of both the VSC-HVDC links respond to the grid frequency change as shown in Figure 5.10b and Figure

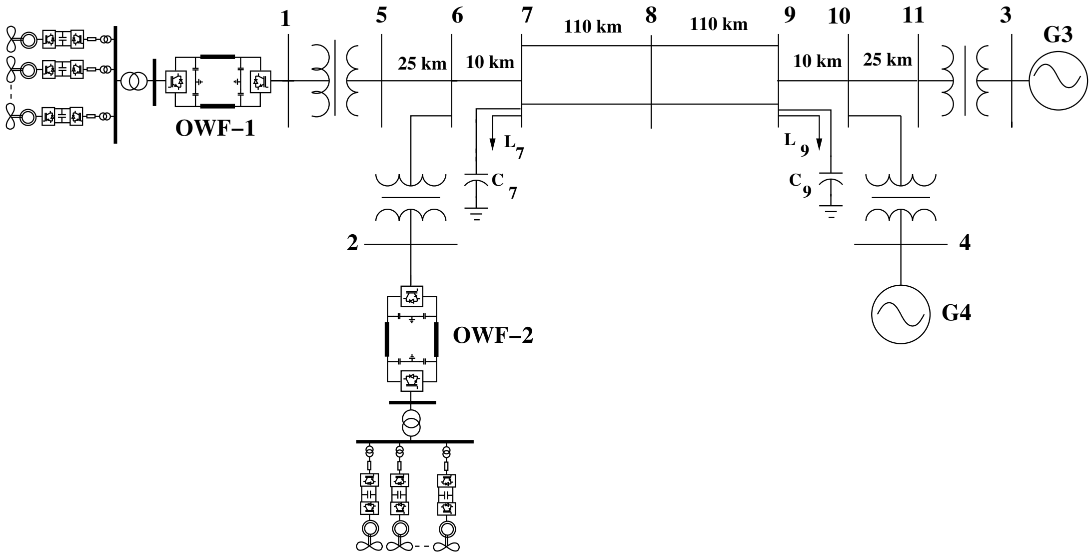

Figure 5.9: Test system - 2

Table 5.2: Parameters of test system - 2

Parameter	Value
VSC-HVDC	
Rated DC voltage	±500 kV
Rated grid voltage	230 kV
Rated Active Power	1500 MVA
Number of submodules	220
Submodule capacitance	7 mF
Line reactor and transformer	1.008 pu
Offshore Wind farm (aggregated parameters)	
Offshore grid frequency	50 Hz
Offshore grid rated voltage	230 kV
Rated power	1100 MVA

5.10c. The system with the PC exhibits a larger variation in DC voltage during the initial 2s after the event compared to the system with DCNP, allowing for the provision of additional inertial energy from the capacitors right after the event. This is evident in the total power input at bus 7 as shown in Figure 5.10d, resulting in a better frequency profile for the system with the proposed control (Figure 5.10a).

Figure 5.11a depicts the average system frequency or the center of inertia (COI) frequency calculated for the entire system by considering the VSC-HVDC-based offshore wind farms as virtual synchronous generators with appropriate virtual inertia constants.

The frequency of the wind farms and generators with respect to the COI frequency is presented in Figure 5.11b for the system with PC and Figure 5.11c for the system with DCNP. It can be observed that the virtual synchronous generators in area-1 collectively oscillate against generators G3 and G4 in area-2, representing the inter-area mode. Additionally, the individual virtual synchronous generators oscillate against each other, representing the local mode. The behaviour is similar to synchronous generators of two areas of a 4-machine system.

a. Frequency at bus – 7

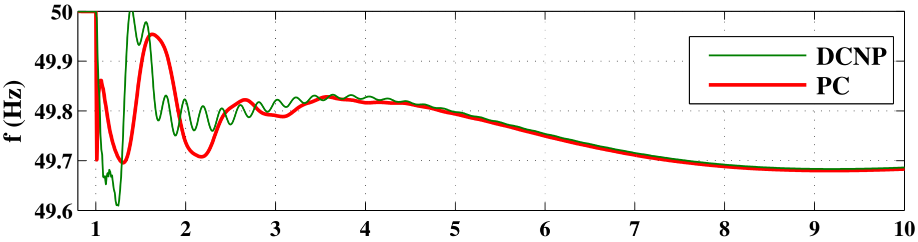

b. DC Voltage at GSVSC of OWF – 2

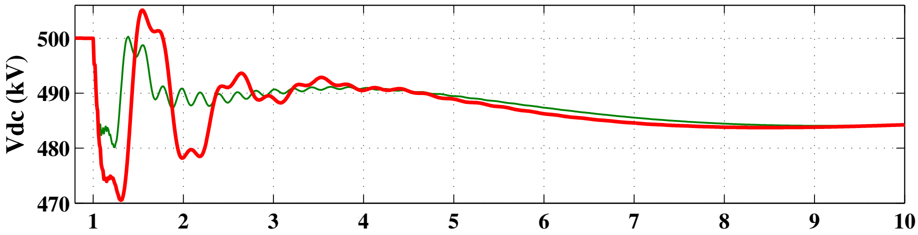

c. DC Voltage at GSVSC of OWF – 1

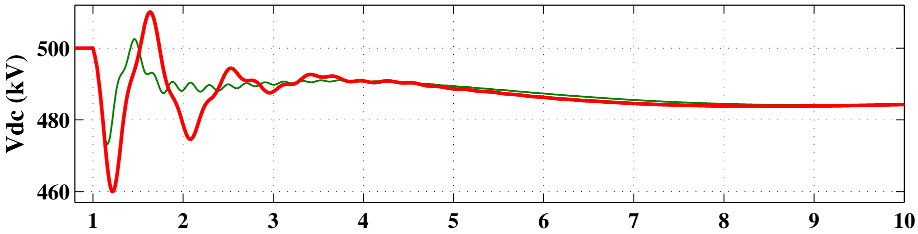

d. Total Power input at bus – 7

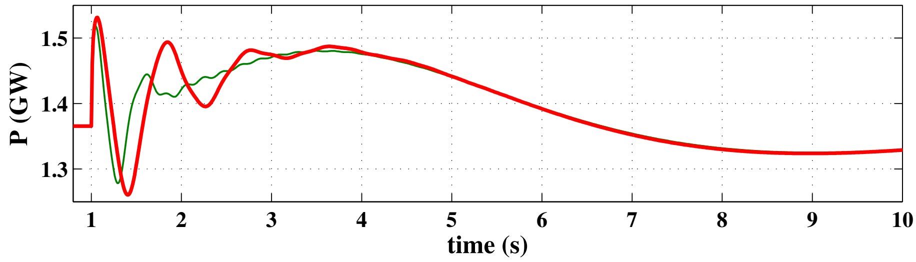

Figure 5.10: Test system - 2 with load addition plots

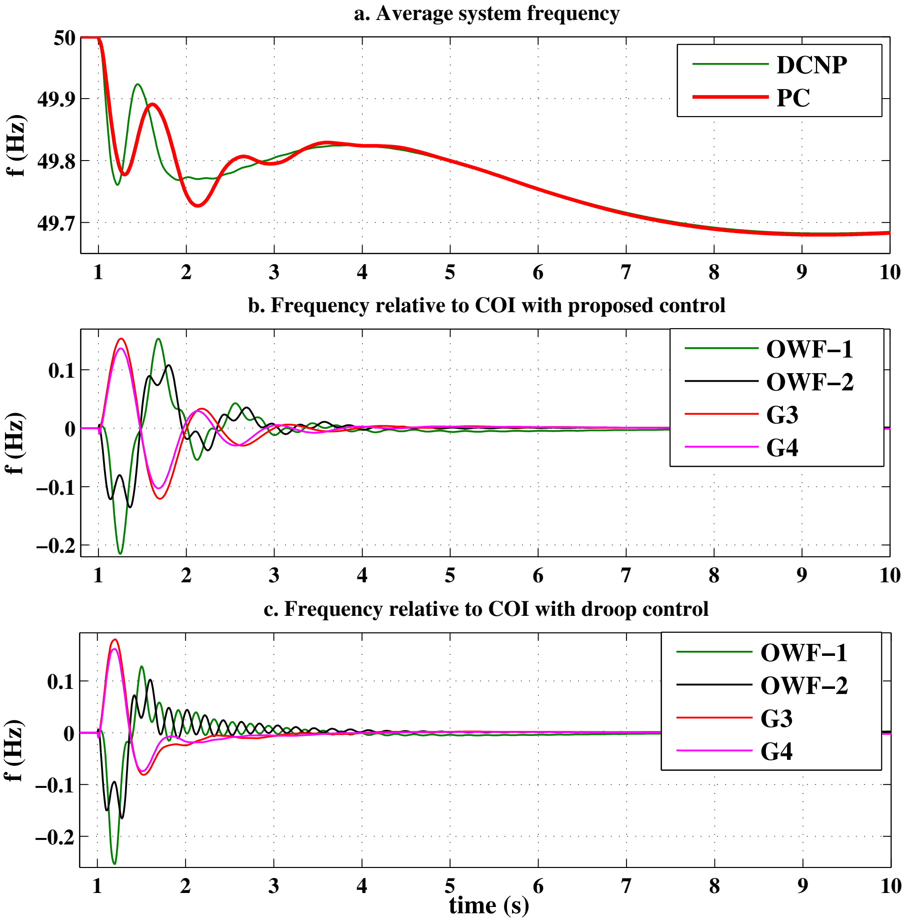

Figure 5.11: Test system - 2 with load addition plots

5.3.2.2 Load deletion at bus-9

In this scenario, a load of 295 MW + j 3 MVAR is tripped at bus-9. As a result, the frequency increases, as shown in Figure 5.12a. This frequency change is reflected in the DC voltages at both GSVSCs, illustrated in Figure 5.12b and Figure 5.12c. Analyzing the power input at bus-7 in Figure 5.12d and the total power input at bus-9 in Figure 5.13a, it can be concluded that the generators in area-2 play a more active role in providing inertial response in this case. The DC capacitors with proposed control provide only slightly larger capacitor energy as compared to system with DCNP. As a result no noticeable improvement can be seen either in ROCOF of frequency at bus-9 as shown in Figure 5.12a or in average system frequency shown in Figure 5.13b. The frequencies w.r.t COI of the virtual synchronous generators of area-1 as well as the generators in area-2 exhibit identical profiles.

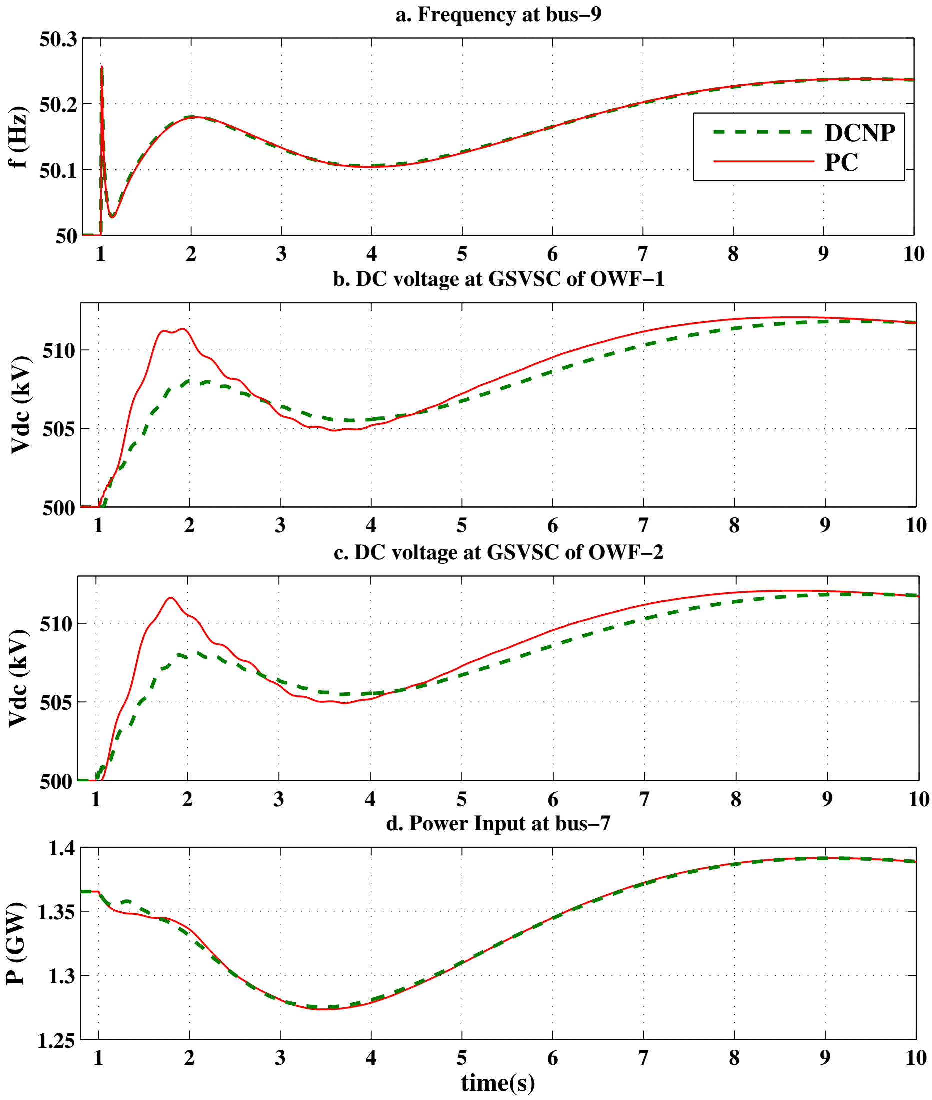

Figure 5.12: Test System - 2 load deletion plots

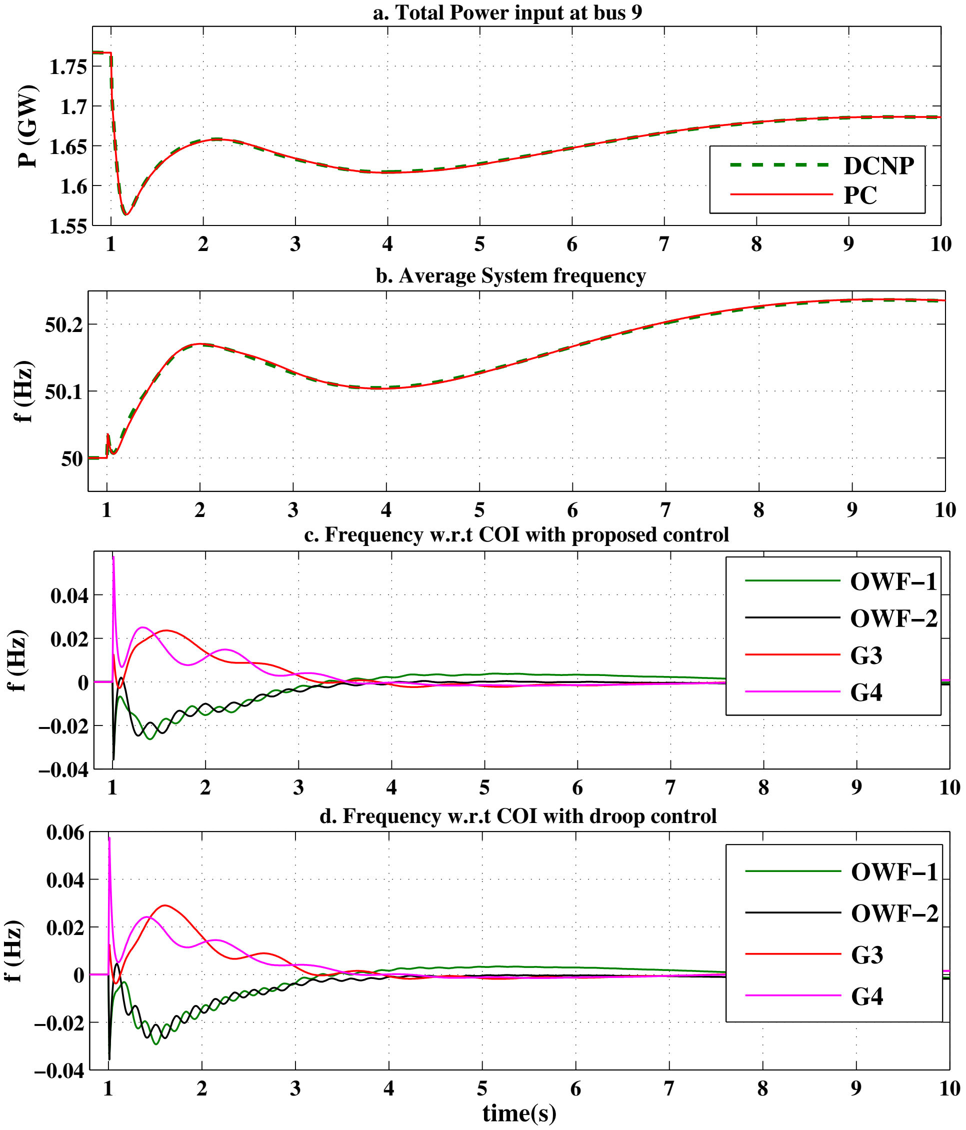

Figure 5.13: Test System - 2 load deletion plots

5.4 Summary

This chapter presents a novel approach to achieve grid synchronization, inertial and damping capabilities in VSC-HVDC connected offshore wind farms that supply power to weak power systems. The main points of this chapter are as follows :

- The proposed synchronization controller utilizes the dynamics of the DC capacitors, which are designed to mimic the behavior of synchronous generators, enabling efficient synchronization.
- The controller utilizes both the energy stored in the capacitors and the inherent inertia of PMSG wind farms to enhance the inertial response. In order to maximise the use of DC capacitor, an appropriate time constant and two distinct DC voltage tolerance bands are chosen for the controller.
- The effectiveness of the proposed control strategy is validated through MATLAB/ SIMULINK simulations using two test systems. The first system consists of offshore wind farms supplying power to a grid represented by a single generator, while the second system involves a multi-machine setup with two VSC-HVDC connected offshore wind farms.
- The proposed controller is compared with existing control topologies - traditional control, droop control with PLL, droop control without PLL and proportional integral control. The proposed controller demonstrates superior effectiveness in providing grid synchronization, inertial and damping response when compared to existing methods.

Chapter 6

CONCLUSIONS

6.1 Work Carried Out and Inferences

The topics discussed in this thesis deal with modelling, control and performance analysis of HVDC links in multi-machine systems with wind farms. The work carried out in this thesis includes :

- The analysis of behavior of synchronous and asynchronous LCC-HVDC links is presented. The systems are simulated and compared to systems with a Thyristor Controlled Series Capacitor (TCSC) line. A 4-machine, two-area system is used for the study. The study examines the dynamic differences of the systems during tie line trips and power level variations. Modal analysis shows that the system with HVDC has the lowest inter-area mode frequency and damping factor compared to systems with and without TCSC for a given power level. Power level changes have an impact on all the dominant swing modes of the system with TCSC, but the attributes of the inter-area mode in the HVDC system remain unaffected. The study introduces a multi-slack bus approach for conducting load flow analysis on asynchronous systems, wherein a slack bus is selected in each area. The study also analyzes the modes of the asynchronous system with LCC-HVDC compared to systems with only one AC tie line or only a TCSC line between the areas. The modal analysis is conducted using prony analysis, which is a signal identification based technique that does not require rigorous calculations as in conventional analytical methods.
- The work discusses the modelling, control, and integration of VSC-HVDC links into multi-machine systems. The effects of VSC-HVDC outer real and reactive con-

trols on frequency controllers are analyzed through simulations. It is found that frequency controllers with feedback real power controller of lowest bandwidth are more robust for events that only affect real power. However, frequency controllers along with feedforward active power controllers perform better during initial transients for events that affect both real and reactive power. The type of reactive power controllers also influences the behavior of frequency controllers, particularly for events affecting both real and reactive power. A simplified model of a VSC-HVDC link is presented, which eliminates DC part dynamics, includes converter associated impedances as part of AC transmission network, and modifies the control system to control converter-related AC quantities. This simplified model effectively captures the impact of VSC controllers, varying power levels, and multiple VSC links in the system. It is also validated for frequency support in asynchronous systems and in traditional control of VSC-HVDC connected offshore wind farms. The simplified model significantly reduces CPU time for simulations.

- A novel methodology for evaluating the power flow and initial condition calculations of VSC-HVDC connected DD-PMSG based wind farms integrated into multi-machine systems is presented. The proposed approach aims to aid the dynamic analysis of these systems. For three instances of most frequently provided specified quantities of the wind farm, effective solutions have been proposed. The stated quantities in the first case are the total number of wind turbines and the total real power output of the wind farm. Here, a method to determine initial wind speed is described. An approach to calculate onshore VSC converter power flow is presented. The total output of the wind farm and power output of each wind turbine is specified in the second case. The procedure to obtain the number of wind turbines in the wind farm is provided. In the third case, the initial speed of the wind and the total number of wind turbines in the wind farm are specified. An iterative algorithm for determining grid side converter power flow is presented in this case. The study presented covers all essential calculations for a VSC-HVDC connected DD-PMSG based offshore wind farm interfaced into a multi-machine system. The approach allows the user to build the dynamic model in any basic dynamic modeller without the requirement of electromagnetic transient packages.

- A methodology to provide grid synchronization and inertial capabilities from VSC-HVDC connected offshore wind farms is proposed. The proposed synchronization controller utilizes the dynamics of the DC capacitors, which are designed to mimic the behavior of synchronous generators, enabling efficient synchronization. Furthermore, the controller utilizes both the energy stored in the capacitors and the inherent inertia of PMSG wind farms to enhance the inertial response. In order to maximise the use of DC capacitor, an appropriate time constant and two distinct DC voltage tolerance bands are chosen for the controller. The controller is validated in a single machine system and a 4-machine system. The analysis is compared with existing control strategies like traditional control and droop control strategies with and without PLL. The simulations prove the efficacy of the proposed controller.

6.2 Future Scope of Work

1. *Implementation of the analysis in multi-terminal HVDC links :* The techniques and approaches presented in this thesis can be effectively applied to multi-terminal HVDC (MTDC) links. It is valuable to explore the dynamic analysis, modal analysis, and control interactions within MTDC systems. Furthermore, it is worthwhile to examine the applicability of the simplified VSC-HVDC model and the grid synchronization and inertial controllers in the context of MTDC links.

2. *Use of supercapacitors for inertial and grid synchronisation methods :* The utilization of supercapacitors in VSC-HVDC based offshore wind farms presents an innovative approach to enhance grid synchronization and inertial support. Supercapacitors, with their rapid energy discharge and recharge capabilities, can effectively mimic the inertia provided by synchronous generators, contributing to the stability of the grid during sudden disturbances.

3. *Virtual Primary and secondary frequency regulation methods from VSC-HVDC connected offshore wind farms:* The proposed grid synchronisation and inertial controller can be further extended to provide primary and secondary frequency regulation from VSC-HVDC connected offshore wind farms.

4. *Virtual voltage and PSS control methods from VSC-HVDC connected offshore wind farms :* Building upon the previous point, the controller's robustness can be further strengthened by incorporating virtual voltage and Power System Stabilizer (PSS) control methods.

5. *Fault ride through capabilities :* Exploring the fault ride-through capabilities of VSC-HVDC-based offshore wind farms, specifically focusing on aspects like zero voltage ride-through and low voltage ride-through, offers an opportunity to investigate a significant area within the literature. The existing literature highlights several research gaps in this area, making it a valuable and promising field for further investigation.

Appendix

A1. TCSC current controller parameters

- K_I = 3
- X_{max} = 0.176 pu, X_{min} = 0
- T_{TCSC} = 0.015s

A2. Parameters of VSC-HVDC link

- Ratings : 450 MVA, ± 320 kV
- Per-unit Base : 100 MVA, 50 Hz
- R_r = 0.01 pu, X_r = 0.1 pu
- R_i = 0.01 pu, X_i = 0.1 pu
- R_{dc} = 0.0021 pu, L_{dc} = 0.0276 pu
- K_{dc} = 100

A3. Parameters of offshore wind farm

Parameters of each wind turbine

- Values of C_p coefficients are : c_1 = 0.22, c_2 = 116, c_3 = 0.4, c_4=5, c_5=12.5, c_6=0
- $\beta = 0°$, $C_{p,max}$ = 0.43821, λopt = 6.325, Air density(ρ)=1.225 kg/m^3, Rotor radius = 37.5 m, H_t = 4.5
- Nominal rotor speed = 18 rpm, Nominal wind speed = 12 m/s

Parameters of each PMSG

- Rated apparent power = 2.2408 MVA, Rated Mech power = 2.0093 MW, V_{mb} = 690 V(rms)
- R_{sact} = 0.73051 mΩ, x_{sdact} = 1.21 mH, $x_{sq_{act}}$ = 2.31 mH
- Rated rotor speed = 22.5 rpm, Rated rotor flux linkage per phase = 4.696 Wb
- H_{mb} = 0.4
- $\omega_{rB} = 2*\pi*11.25$ rad/s, $\omega_{gB} = 2*\pi*50$ rad/s

Parameters of GSC, Offshore Network

- R_{GSC} = 0.002 pu, X_{GSC} = 0.02 pu (on single wind turbine base of 2.2408 MVA and 690 V)
- R_{OFF} = 0.001 pu, X_{OFF} = 0.012 pu (on a base of 100 MVA, 50 Hz)

Bibliography

Abedin, T., Lipu, M. S. H., Hannan, M. A., Ker, P. J., Rahman, S. A., Yaw, C. T., Tiong, S. K., and Muttaqi, K. M. (2021). “Dynamic Modeling of HVDC for Power System Stability Assessment: A Review, Issues, and Recommendations” *Energies 2021*, 14(6).

Abhijit, R. (2018). “Recent Technical Development in High Voltage Direct Current (HVDC) Technology, a special Emphasis to Indian projects.”, [Online] Available: https://www.linkedin.com/pulse/recent-technical-development-high-voltage-direct-current-abhijit-roy.

Ackermann, T. (2005). “Wind Power in Power Systems”, John Wiley and Sons, Ltd, Stockholm, Sweden.

Adeuyi, O. D., Cheah-Mane, M., Liang, J. and Jenkins, N. (2017). “Fast Frequency Response From Offshore Multiterminal VSC–HVDC Schemes” *IEEE Transactions on Power Delivery*, 32(6), 2442–2452.

Agnihotri, P., Kulkarni, A. M., Gole, A. M., Archer, B. A. and Weekes, T. (2017). “A Robust Wide-Area Measurement-Based Damping Controller for Networks With Embedded Multiterminal and Multiinfeed HVDC Links” *IEEE Transactions On Power Systems*, 32(5), 3884–3892.

Ali, M., Milanovic, J. V., Ilie, I. and Chicco, G. (2011). “Comparison of wind farm aggregate models for transient stability studies” *17th Power Systems Computation Conference*.

Asimenia, K., Qiuwei, W. and Haoran, Z. (2016). “Review of VSC HVDC connection for offshore wind power integration” *Renewable and Sustainable Energy Reviews*, 59, 1405–1414.

Asvapoositkul, S. and Preece, R. (2020). “Impact of HVDC dynamic modelling on power system small signal stability assessment” *International Journal of Electrical Power and Energy Systems*, 123.

Bandaru, T., Dhawa, U., Chatterjee, D. and Bhattacharya, T. (2018). “Improving the Transient Stability by Modifying the Power Exchange by the HVDC Transmission” *National Power Systems Conference*.

Bernat, J. O., and Preece, R. (2019). “Impact of VSC-HVDC Reactive Power Control Schemes on Voltage Stability” *IEEE Milan PowerTech*.

Bin, W., Yongqiang, L., Navid, Z. and Samir, K. (2011). “Power Conversion And Control Of Wind Energy Systems”, John Wiley and Sons, Ltd, New Jersey.

Chen, Y., Moreno, R., Strbac, G. and Alvarado, D. (2018). “Coordination Strategies for Securing AC/DC Flexible Transmission Networks With Renewables” *IEEE Transactions on Power Systems*, 33(6).

Chia-Nan, W., Wen-Chang, L. and Xuan-Khao, L. (2014). “Modelling of a PMSG Wind Turbine with Autonomous Control” *Mathematical Problems in Engineering Journal*, 2014.

Cole, S. and Ronnie, B. (2011). “A proposal for standard VSC HVDC dynamic models in power system stability studies” *Electric Power Systems Research*, 81, 967–973.

Divya, K.C. and Nagendra, Rao, P.S. (2006). “Models for wind turbine generating systems and their application in load flow studies” *Electric Power Systems Research*, 76, 844 –856.

Dragan, J. and Khaled, A. (2015). “High-Voltage Direct-Current Transmission Converters, Systems and DC Grids”, John Wiley and Sons, Ltd.

Ferr, J. A., Pipelzadeh, Y. and Green, T. C. (2015). “Blending HVDC-Link Energy Storage and Offshore Wind Turbine Inertia for Fast Frequency Response” *IEEE Transactions on Sustainable Energy*, 6(3), 1059 –1066.

Gasca, J.J.S. and Trudnowski, D.J. (2012). “Identification of electromechanical modes in power systems” *IEEE Taskforce Report PES*, 15.

Giddani, O.K., Grain P.A., Olimpo, A.L., Stephen, L. and Kjetil, U. (2012). "Small-Signal Stability Analysis of Multi-Terminal VSC-Based DC Transmission Systems" *IEEE Transactions on Power Systems*, 27(4), 1818 –1830.

"GWEC : Global Wind Report - 2023", [Online] Available: https://gwec.net/global-wind-report-2023/.

He, J., Wu, K., Huang, L., Xin, H., Lu, C. and Wang, H., (2018). "A coordinated control scheme to realize frequency support of PMSG-based wind turbines in weak grids" *IEEE Power and Energy Society General Meeting (PESGM)*, 1 – 5.

Hingorani, N. G., and Gyugyi, L. (2000). "Understanding FACTS: Concepts and Technology of Flexible AC Transmission Systems", Wiley-IEEE Press.

Hu, Z. and Mao, C. (2005). "Improvement of Transient Stability in AC system by HVDC light" *IEEE/PES Transmission and Distribution Conference and Exhibition : Asia and Pacific*, Dalian, 2005.

Hua, Y., Wei, P., Li, K., and Ting A. (2019). "Low-Order Response Modeling for Wind Farm-MTDC Participating in Primary Frequency Controls" *IEEE Transactions on Power Systems*, 34(2), 942–952.

Huang, L., Xin, H., Wang, Z., Wu, K., Wang, H., Hu, J. and Lu, C., (2017). "A virtual synchronous control for voltage-source converters utilizing dynamics of DC-link capacitor to realize self-synchronization" *IEEE Journal of Emerging and Selected Topics in Power Electronics*, 5(4), 1565–1577.

Huang, L., Xin, H., Yang, H., Wang, Z. and Xie, H., (2018). "Interconnecting very weak AC systems by multiterminal VSC-HVDC links with a unified virtual synchronous control" *IEEE Journal of Emerging and Selected Topics in Power Electronics*, 6(3), 1041–1053.

Hennig, T., Lower, L., Faiella, L. M., Stock, S., Jansen, M., Hofmann, L. and Rohrig, K. (2014). "Ancillary Services Analysis of an Offshore Wind Farm Cluster – Technical Integration Steps of a Simulation Tool" *Energy Procedia*, 53.

Jahan, E., Hazari, Md. R., Rosyadi, M., Umemura, A., Takahashi, R., and Tamura, J. (2017). "Simplified Model of HVDC Transmission System Connecting Offshore Wind Farm to Onshore Grid" *2017 IEEE Manchester PowerTech.*

Jef, B., Stijn, C. and Ronnie, B. (2014). "Modeling of Multi-Terminal VSC HVDC Systems With Distributed DC Voltage Control" *IEEE Transactions on Power Systems*, 29(1), 34–42.

Jiebei, Z., Campbell, D.B., Grain, P.A., Andrew, J.R,, and Chris G.B. (2013). "Inertia Emulation Control Strategy for VSC-HVDC Transmission Systems" *IEEE Transactions on Power Systems*, 28(2), 1277 –1287.

Kabsha, M. and Zakir, H. R. (2020). "A New Control Scheme for Fast Frequency Support from HVDC connected Offshore Wind Farm in Low Inertia System" *IEEE Transactions on Sustainable Energy*, 11(3), 1829–1837.

Kamel, S., AboElHassan, M. A., Ebeed, M., Yu, J., and Jurado, F. (2019). "Developed HVDC power injection model for power flow analysis with multi-control functions considering operating constraints" *Electrical Engineering*.

Khan, S. and Bhowmick, S. (2019). "A Generalized Power-Flow Model of VSC-Based Hybrid AC–DC Systems Integrated With Offshore Wind Farms" *IEEE Transactions on Sustainable Energy*, 10(4).

Kouadri, R., Slimani, L. and Bouktir, T. (2016). "Optimal Power Flow for Combined AC and VSC-MTDC system with large penetration of wind farm" *Proceedings of the International Conference on Recent Advances in Electrical Systems*.

Krishna, R. and Shubhanga, K.N. (2018). "MAPE - An Alternative Fitness Metric for Prony Analysis of Power System Signals" *International Journal of Emerging Electric Power Systems*, 19.

Kumar, V. S. S. and Thukaram, D. (2017). "Accurate modeling of doubly fed induction generator based wind farms in load flow analysis" *Electric Power Systems Research*, 155.

Kundur, P. (1994). "Power system stability and control", Mc Graw Hill publications, New York.

Latorre, H. F., Ghandhari, M. and Soder, L. (2008). "Active and reactive power control of a VSC-HVdc" *Electric Power Systems Research*, 78.

Li, S., Mike, B., Robin, P., Jovica V.M., Keith, B. and Manolis B. (2016). "The Effect of VSC-HVDC Control on AC System Electromechanical Oscillations and DC System Dynamics" *IEEE Transactions on Power Delivery*, 21(3), 1085 –1095.

Li, Y., Zhang, Z., Yang, Y., Li, Y., Chen, H. and Xu, Z. (2014). "Coordinated control of wind farm and VSC–HVDC system using capacitor energy and kinetic energy to improve inertia level of power systems" *International Journal of Electrical Power and Energy Systems*, 59, 79 –92.

Liu, H. and Chen, Z. (2015). "Contribution of VSC-HVDC to Frequency Regulation of Power Systems With Offshore Wind Generation" *IEEE Transactions on Energy Conversion*, 30(3), 918 –926.

Lu, G. -L., Lin, C. -H. and Wu, Y. -K. (2021). "Comparison of Communication-Based and Coordination-Based Frequency Control Schemes for HVdc-Connected Offshore Wind Farms" *IEEE Transactions on Industry Applications*, 57(4), 3352 – 3365.

Meer, A. A., Rueda-Torres, J., Silva, F., Gibescu, M. and Meijden, M. (2016). "Computationally Efficient Transient Stability Modeling of multi-terminal VSC-HVDC" *IEEE Power and Energy Society General Meeting (PESGM).*

Mercado V. M. J., Gomez, L. D., Rabaza, O. and Alameda-Hernandez, E. (2015). "Aggregated models of permanent magnet synchronous generators wind farms" *Renewable Energy, Elsevier*, 83, 1287–1298.

"MERCOM : Mandatory Wind Energy Purchase Fuels Installation Growth of 168% in Q1 2023", [Online] Available: https://www.mercomindia.com/mandatory-wind-growth-of-168-in-q1-2023/.

Minyuan, G., Wulue, P., Jing, Z., Quanrui, H., Jingzhou C. and Xiang Z. (2015). "Synchronous Generator Emulation Control Strategy for Voltage Source Converter (VSC) Stations" *IEEE Trans. on Power Systems*, 30(6), 3093 –3101.

Muyeen, S. M., Takahashi, R. and Tamura, J. (2010). "Operation and Control of HVDC-Connected Offshore Wind Farm" *IEEE Transactions on Sustainable energy*, 1(1), 30 –37.

Padiyar, K. R. (2002). "Power system dynamics - stability and control" BS Publications, Hyderabad, India.

Padiyar, K. R. (2009). “FACTS controllers in power transmission and distribution” New Age International (P) Ltd., Publishers, New Delhi, India.

Padiyar, K. R. and Kulkarni, A. M. (2019). *Dynamics and control of electric transmission and microgrids*, John Wiley and Sons, Inc., USA.

Pal, B. and Chaudhuri, B. (2015). “Robust Control in Power Systems”, Springer, USA.

Pizano, M. A., Fuerte, E. C. R., Ambriz, P. H. and Acha, E. (2007). “Modeling of VSC-Based HVDC Systems for a Newton-Raphson OPF Algorithm” *IEEE Transactions on Power Systems*, 22(4).

Preece, R., Milanovic, J. V., Almutairi, A. M., and Marjanovic, O. (2013). “Damping of inter-area oscillations in mixed AC/DC networks using WAMS based supplementary controller” *IEEE Transactions on Power Systems*, 28(2).

Prithwish, M., Seshadri, P., Gangrekar, C., Kumar, C., Rai, A. B., and Reddy, N. M. (2015). “WAMS and Synchrophasor Experience During Synchronization of Large Grids in India” *IEEE International Conference on Signal Processing, Informatics, Communication and Energy Systems*.

Rahim, A. H. M. A. (2011). “Integration of Fixed and Variable Speed Wind Generator Dynamics with Multimachine AC Systems” *International Journal of Electrical and Computer Engineering*, 5(5).

Ratnam, K. S., Palanisamy, K. and Yang, G., (2020). “Future low-inertia power systems: Requirements, issues, and solutions-A review.” *Renewable and Sustainable Energy Reviews*, 124.

Renxin, Y., Shi, G., Cai, X., Zhang, C., Li, G. and Liang, J., (2020). “Autonomous synchronizing and frequency response control of multi-terminal DC systems with wind farm integration” *IEEE Transactions on Sustainable Energy*, 11(4), 2504–2514.

Roland R. and Lukasz S. (2020). “Evolution of the HVDC Link Connecting Offshore Wind Farms to Onshore Power Systems” *Energies 2020*, 13(8).

Schauder, C. and Mehta, H. (1993). “Vector analysis and control of advanced static VAR compensators,” *IEE Proceedings-C*, 140(4).

Shewarega, F. and Erlich, I. (2014). “Simplified Modeling of VSC-HVDC in Power System Stability Studies” *IFAC Proceedings Volumes*, 47(3), 9099–9104.

Shubhanga, K. N. (2018). “Power System Dynamics : A Dynamic Perspective”, Pearson India Education Services, U.P., India.

Sigrist, L., Echavarren, F., Rouco, L. and Panciatici, P. (2015). “A fundamental study on the impact of HVDC lines on transient stability of power systems” *IEEE Eindhoven PowerTech.*

Silva, B., Moreira, C. L., Seca, L., Phulpin, Y. and Lopes, J. P., (2012). “Provision of inertial and primary frequency control services using offshore multiterminal HVDC networks” *IEEE Transactions on sustainable Energy*, 3(4), 800–808.

Stijn, C., Jef, B. and Ronnie B. (2010). “Generalized Dynamic VSC MTDC Model for Power System Stability Studies” *IEEE Transactions on Power Systems*, 25(3), 1655 –1662.

Teena, J. and Shubhanga, K.N. (2017). “Response-type Modelling of a Two-terminal HVDC Link for Power System Stability Analysis” *Interntional Conference on Innovations in Power and Advanced Computing Technologies*. 1 –6.

Uday, K. and Shubhanga, K.N. (2015). “Modeling of FACTS Controllers in power flow programmes to analyze prevention of loop flows” *IEEE INDICON, New Delhi, India* 1 –6.

Vennelaganti, S. G. and Chaudhuri, N. R. (2018). “New Insights Into Coupled Frequency Dynamics of AC Grids in Rectifier and Inverter Sides of LCC-HVDC Interfacing DFIG-Based Wind Farms” *IEEE Transactions on Power Delivery*, 33(4).

Wang, T., Song, G. and Yin, L. (2019). “Reduced-Order Model Of VSC-HVDC Applied to Passive Network Based On Optimal Reduction Algorithm” *Renewable Power Generation Conference (RPG).*

Wang, W., Beddard, A., Barnes, M. and Marjanovic, O. (2014) “Analysis of Active Power Control for VSC–HVDC,” *IEEE Transactions on Power Delivery*, 29(4).

Wei, Y., Li, Q., Liu, K., Wang, P., Zeng, Z. and Wang, X. (2020). “A hybrid algorithm for the load flow analysis of VSC-HVDC systems based on $1 + \sqrt{2}$ order Newton-Raphson and simplified Newton” *Electrical Power and Energy Systems*, 118.

“WECC Wind Power Plant Dynamic Modeling Guide’, WECC Renewable Energy Modeling Task Force.

Xiao, M. and Tang, X. (2015). “A Study on Damping Low Frequency Oscillation in Power System by VSC-HVDC” *International Conference on Elelctric Utility Deregulation and Restructuring and Power Technologies*.

Xudan, L. and Andreas, L. (2018). “Control of VSC-HVDC Connected Offshore Windfarms for Providing Synthetic Inertia” *IEEE Journal of Emerging and Selected Topics in Power Electronics*, 6(3), 1407–1417.

Yang, R., Zhang, C., Cai, X. and Shi, G., (2018). “Autonomous grid - syncronising control of VSC - HVDC with real - time frequency mirroring capability for wind farm integration” *IET Renewable Power Generation*, 12, 1572 –1580.

Yao, L., Wang, X., Li, Y., Duan C. and Wu, X. (2020). “Distributionally Robust Chance-Constrained AC-OPF for Integrating Wind Energy Through Multi-Terminal VSC-HVDC” *IEEE Transactions on Sustainable Energy*, 11(3).

Ye, Y., Qiao, Y., Xie, L. and Lu, Z. (2020). “A Comprehensive Power Flow Approach for Multi-terminal VSC-HVDC System Considering Cross-regional Primary Frequency Responses” *Journal of Modern Power Systems and Clean Energy*, 8(2).

Yogarathinam, A., Kaur, J. and Chaudhuri N. R. (2017). “Impact of Inertia and Effective Short Circuit Ratio on Control of Frequency in Weak Grids Interfacing LCC-HVDC and DFIG-Based Wind Farms” *IEEE Transactions on Power Delivery*, 32(4).

Yong, L., Longfu, L, Christian, R, Sven, R. and Fusheng, L. (2012). “Realization of Reactive Power Compensation Near the LCC-HVDC Converter Bridges by Means of an Inductive Filtering Method” *IEEE Transactions on Power Electronics*, 27(9), 3908 – 3923.

Yousef, P., Nilanjan, R.C., Balarko, C. and Tim, C.G. (2017). “Coordinated Control of Offshore Wind Farm and Onshore HVDC Converter for Effective Power Oscillation Damping” *IEEE Transactions on Power Systems*, 32(3), 1860 –1872.

Yuan, X., Du, Z., Li, Y., Wu, G., Li, J., Wu, X. and Li, C., (2021). “Novel cascading scheme of VSC - HVDC with DC voltage synchronisation control for system frequency support” *IET Generation, Transmission and Distribution*, 15, 3502 –3519.

Yujun, L., Zhang, Z., Yang, Y., Li, Y., Chen, H. and Xu, Z. (2014). "Coordinated Control of wind farm and VSC-HVDC system using capacitor energy and kinetic energy to improve inertia level of power systems" *International Journal of Electrical Power and Energy Systems*, 59, 79–92.

Zeni, L., Eriksson, R., Goumalatsos, S., Altin, M., Sorensen, P., Anca, D. and Kjaer, P. (2016). "Power Oscillation Damping From VSC–HVDC Connected Offshore Wind Power Plants" *IEEE Transactions on Power Delivery*, 31(2).

Zeng, X., Liu, T., Wang, S., Dong, Y., Li, B., and Chen, Z. (2020). "Coordinated control of MMC-HVDC system with offshore wind farm for providing emulated inertia support" *IET Renewable Power Generation*, 14, 673–683.

Zhang, L., Harnefors, L. and Nee, H. P. (2010). "Power-Synchronization Control of Grid-Connected Voltage-Source Converters" *IEEE Transactions on Power Systems*, 25(2), 809 –820.

Zhao, M., Chen, Z. and Blaabjerg F. (2008). "Load flow analysis for variable speed offshore wind farms" *IET Renewable Power Generation.*, 3(2), 120–132.

Zhiyong, Y., You, S., Liu, Y., Osborn, D., and Pan, J. (2017). "Frequency Control Capability of VSC-HVDC for Large Power Systems" *IEEE Power and Energy Society General Meeting*.

Zhong, Q. C. and Weiss, G. (2011). "Synchronverters : Inverters That Mimic Synchronous Generators" *IEEE Transactions on Industrial Electronics*, 58(4), 1259–1267.

Zhou, Y., Zhao, L., Lee, W., Zhang, Z. and Wang, P. (2019). "Optimal Power Flow in Hybrid AC and Multi-terminal HVDC Networks with Offshore Wind Farm Integration Based on Semidefinite Programming" *2019 IEEE Innovative Smart Grid Technologies - Asia*.

Publications based on the thesis

Journal Papers

1. Rashmi and D.N.Gaonkar, “A Novel Approach for Steady State Calculations of VSC-HVDC connected PMSG based Offshore Wind Farms integrated into Multi-Machine Systems”, *Electric Power Components and Systems*, Vol. 51, No. 10, pp. 961–971, March 2023.

2. Rashmi and D.N.Gaonkar, “A Novel Simplified Modeling Approach for VSC-HVDC Links in Performance Analysis of Multi-Machine Systems”, *Arabian Journal for Science and Engineering*, Aug. 2023.

Conference Papers

1. Rashmi and D.N.Gaonkar, “Modelling and Performance Analysis of Synchronous and Asynchronous Links Integrated into Multi-Machine Systems” *2022 IEEE 19th India Council International Conference (INDICON), Kochi, India*, pp.1–6, Nov. 2022.

2. Rashmi and D.N.Gaonkar, “Effect of Primary VSC-HVDC Controls on the Performance of Ancillary Frequency Control Strategies” *2022 IEEE 7th International Conference on Recent Advances and Innovations in Engineering (ICRAIE), MANGALORE, India*, pp.487–493, Dec. 2022.